PHYSICAL PROCESSES IN A WESTERN ANTARCTIC PENINSULA FJORD

A dissertation submitted to the graduate division of the University of Hawai'i at Mānoa, in partial fulfillment of the requirements for the degree of

DOCTOR OF PHILOSOPHY
IN
OCEANOGRAPHY

December 2018

By:
Øyvind Lundesgaard

Thesis committee:
Brian Powell, chairperson
Mark Merrifield
Craig Smith
Peter Winsor
Eric Firing
Amy Moran

Abstract

The western Antarctic Peninsula (wAP) is lined with glacio-marine fjords which connect the coastal ocean with the terrestrial ice sheet. The physical oceanography of these fjords is relatively unexplored despite their potential importance for regional glaciology, oceanography, and geochemistry, as well as for the productive marine ecosystems in the fjords. This dissertation explores the physical oceanography of a glacial wAP fjord, and identifies and examines key dynamical processes which occur in the system. The analysis is built around comprehensive oceanographic and atmospheric observations from Andvord Bay, a glacial fjord located on the northwestern wAP. Measurements were collected between December 2015 and March 2017 during three research cruises, and with moored sensors, as part of the *FjordEco* project.

In the first part of the dissertation, I describe the physical environment of Andvord Bay, including the atmospheric and glaciological forcing conditions, and the hydrography and energetics of the fjord in relation to the outside ocean. Since Andvord Bay is located just north of the present influence of relatively warm modified Upper Circumpolar Deep Water, the fjord glaciers are not currently in retreat, and glacial mass flux into the ocean occurs predominantly in the form iceberg calving. Meltwater runoff, mean winds, tidal currents and mixing are all weak inside the fjord, and as a result the fjord is dynamically quiet compared to the outside ocean. The lack of a strong mean circulation provides beneficial conditions for phytoplankton blooms, and partially isolates the fjord from temperature variations in the Gerlache Strait. Seasonal water mass exchange is likely driven by low-frequency dynamics of the Gerlache Current as well as by occasional katabatic wind events.

The second part of the dissertation examines the effects of katabatic wind events on the ocean within a wAP fjord. A strong, down-fjord katabatic wind event observed during December 2015 cruise appears to have had significant and immediate effects on the fjord waters, effectively flushing out the surface layer and altering the stratification in the upper 100 m. A series of idealized numerical experiments were conducted in order to explore the effect of such forceful down-axis winds on fjord water masses and exchange with the exterior ocean. Based on these simulations and observations, I discuss how episodic wind events may drive significant fluxes of nutrients, ice and water properties in otherwise quiescent Antarctic fjords.

The final part of the dissertation examines buoyant plumes generated by ice-ocean interactions at the glacier terminus. Mid-water intrusions of anomalously cold and turbid water were observed in ocean profiles from inner Andvord Bay during all three research cruises. I characterize the spatial distribution of the intrusions, and examine the water properties observed during near-glacier surveys using hydrographic profiles and an autonomous underwater vehicle. Using water mass analysis and a pre-existing analytical model, it is shown that the observations are consis-

tent with a deep, localized source of submarine meltwater. Glacial plumes in Andvord Bay are relatively weak compared to comparable fjord environments with subglacial discharge of highly buoyant freshwater. While the plumes are unlikely to drive significant melt or ocean circulation, they may be an important vertical pathway of sediment, trace metals and other geochemical tracers of terrestrial origin from the glacier grounding line to the upper ocean.

Acknowledgements

A large number of people have contributed to this work in various ways. I would particularly like to thank my main advisor Brian Powell for his mentorship, and for his encouragement and patience throughout the work with this dissertation. I would also like to thank my co-advisor Mark Merrifield for bringing me into the FjordEco project, and for all his help and assistance along the way. My remaining dissertation committee members, Peter Winsor, Craig Smith, Eric Firing and Amy Moran, have all contributed crucial support and guidance at various stages of the work.

Martin Truffer, David Sutherland, Hank Statscewich, Emily Eidam, Lisa Hahn-Woernle and Maria Vernet have all provided invaluable feedback on various parts of my research. Glenn Carter generously made his microstructure profiler available for the FjordEco cruises, and his help, along with that of Rockland Scientific and Polar Latitudes, made the turbulence measurements possible.

I am very grateful to Dave and the entire Sutherland lab for having me as a visiting student at the University of Oregon. I enjoyed my time in Eugene immensely and learned a lot from everyone at UO during my stay.

It has been a great privilege to be able to do research at sea in what must surely be one of the most beautiful regions of the world. This work would not have been possible without everyone who contributed during the FjordEco cruises, including captains and crews of the *Gould* and the *Palmer*, Antarctic Support Contract staff and the different science teams.

I am thankful to all the fellow students and researchers I've worked with during these three years, for their company and for many inspiring discussions on and off the topic of oceanography. Of those not already listed, I would like to mention Amanda, Alma, Seth, Saulo, Kelly, Svetlana, Andrei, Gabi, Dale, Sarah, Emma, Sarah, Sherry, Jack, Kiefer, Lauren, Lindsey, Kiya, Kristin, Ted, Maria, Alex, Katy, Daniel, Angeles, Dustin, Becca and Astrid.

Lastly, I want to thank my girlfriend Katelyn, my mother Nina and other family and friends for their support through this process. I certainly couldn't have done this without you.

This work was financed by the National Science Foundation under grant OPP 1443680.

Contents

List of Figures

List of Tables

Chapter 1

Introduction

1.1 Motivation

Glacial fjords are connected at one end to the terrestrial ice sheet and at the other to the coastal ocean. The fjords interact in various ways with the atmosphere and different forms of ice, provide pathways for freshwater, glacial ice and sediment into the ocean, and constitute important habitats for marine organisms. The study of glacial fjord systems therefore encompasses a large number of disciplines including glaciology, climate science, geology, chemistry and biology. Each is connected in various ways to the physical oceanography, which describes the composition of ocean waters, the dynamics governing flow and transport, and the response of fjord waters to external forcing at the interfaces with the atmosphere, outer ocean and the ice sheet.

The western Antarctic Peninsula (wAP) is the warmest region of continental Antarctica. Its coastal waters host highly productive marine ecosystems (Ducklow et al., 2007; Smith et al., 2013), and its complex coastline is home to several hundred marine-terminating glaciers (Cook et al., 2014). During the latter half of the 20th century, the wAP experienced rapid warming of both the atmosphere and the ocean (Vaughan et al., 2003; Meredith and King, 2005; Turner et al., 2005; Cook et al., 2016). Previous studies have linked this warming to ongoing large-scale changes in the region, including shifts in biological productivity (Clarke et al., 2007; Montes-Hugo et al., 2009; Moreau et al., 2015), reduction of sea ice cover (Zwally et al., 2002; Stammerjohn et al., 2008), and glacier thinning and retreat (Pritchard and Vaughan, 2007; Wouters et al., 2015; Cook et al., 2016).

While the recent decades has seen a rapid increase in our knowledge of ocean processes in glacial fjords, fjord systems along the wAP are relatively understudied from a physical oceanographic perspective. Due to the close connection between small-scale fjord processes and mass loss from the Greenland Ice Sheet (Vieli and Nick, 2011; Straneo and Cenedese, 2015), much of our current knowledge of glacial fjord dynamics is based on studies from Greenland. The growing body of research from fjords in Greenland and other high-latitude regions has shown that the physical oceanography of glacial fjord varies between different systems, and can involve many different processes, including freshwater discharge (Straneo et al., 2011; Carroll et al., 2015), wind forcing (Oltmanns et al., 2013; Carroll et al., 2017; Spall et al., 2017), sea ice interactions (Azetsu-Scott and Syvitski, 1999; Cottier et al., 2010), ocean-driven melt (Motyka et al., 2003; Xu et al., 2013), external ocean forcing by tides (Johnson et al., 2011; Mortensen et al., 2011) and

low-frequency density fluctuations (Jackson et al., 2014; Sutherland et al., 2014b). In comparison, the study of wAP fjords is in its infancy, but is attracting growing interest due to the documented ongoing ocean-driven mass loss from the Antarctic Peninsula Ice Sheet (Cook et al., 2016).

The goal of this dissertation is to characterize the physical oceanography of a glacial wAP fjord, Andvord Bay. The first part of the work is exploratory, aiming to describe the physical environment of the fjord based on a synthesis of a large number of observations collected between November 2015 and March 2017 during the *FjordEco* project. The second part targets two specific dynamical mechanisms of potential importance to the fjord; the effects of strong, episodic wind events and the generation of mid-water intrusions of glacially modified waters by ice-ocean interactions near the terminus of a fast-flowing glacier.

1.2 STRUCTURE OF THE DISSERTATION

In addition to this brief introduction (Chapter 1), the dissertation consists of three main chapters (Chapters 2-4) as well as a final chapter summarizing the conclusions of this work and remaining open questions (Chapter 5). The three main chapters of this dissertation (Chapters 2-4) are intended to compliment each other, but can also be read individually. Each is written as an individual study, including abstracts and introductions as well as separate appendixes containing chapter-specific supplementary information. Since much of the relevant background literature is shared between the three main chapters, a common reference list is found at the back of the dissertation.

Chapter 2 presents an overview of the physical environment of Andvord Bay based on observations collected during the *FjordEco* project. The subsequent two chapters are motivated by the findings from this observational study. The aim of Chapter 2 is to characterize the physical oceanographic setting of the fjord, addressing the following questions:

- What characterizes the *hydrographic regime* of the fjord: what water masses are present, and how do ocean properties vary over time?
- Which characterizes the *dynamical regime* of the fjord: How energetic is the fjord marine environment and what are the important forcing mechanisms?
- What drives exchange between the fjord and the external ocean?

Chapter 3 is motivated by the observation of strong, katabatic wind forcing events in Andvord Bay. In this chapter, observations from a specific wind event are studied in detail, and supplemented by a numerical modelling study used to explore the effect of such wind events on the ocean in Andvord Bay and comparable fjords. The focus is in particular directed towards the following questions:

- What is the dynamical response of a wAP fjord to strong episodic wind forcing?
- How efficient are wind events at flushing out the surface layer?
- Can wind events drive substantial import of external deep waters?

Chapter 4 focuses on interactions between the ice and ocean in Andvord Bay. It is motivated by Chapter 2, in which Andvord Bay was characterized as a cold, low-freshwater environment, but with some signature of glacier interactions in the form of mid-water intrusions of cold, turbid water masses. In Chapter 4, these plumes are studied in more detail, including their spatial distribution and water mass properties. The observations are compared with a pre-existing theoretical framework for upwelling plumes generated by the submarine release of buoyant water. The main questions addressed in this chapter can be summarized as follows:

- What is the origin of the mid-water intrusions observed in wAP fjords?
- What is the composition of glacially modified water masses observed in these plumes?
- Do buoyant plumes generate significant fluxes of water and particles, or drive glacial melt?

Chapter 2

Andvord Bay: Hydrography and energetics

Fjords along the western Antarctic Peninsula contain rich marine ecosystems and tidewater glaciers sensitive to ocean change, but the physical oceanography of these fjords has not previously been studied in detail. This paper presents a comprehensive description of the physical environment of Andvord Bay, a glacial fjord located in the Gerlache Strait on the northern end of the Peninsula. Measurements were collected as part of the *FjordEco* program between November 2015 and March 2017, including three research cruises and a number of fixed installations (sub-surface moorings, time lapse cameras, and automatic weather stations). Andvord Bay is located just north of a sill in the Gerlache Strait, which inhibits the direct influence of warm Upper Circumpolar Deep Water from the shelf. Deep waters in the fjord are therefore relatively cold, and glaciers in Andvord Bay are not subject to the ocean-driven retreat observed farther south on the Peninsula. Instead, mass flux from the glaciers occurs mainly through calving. The influence of melt is small compared to glacial fjords in the Arctic, although summer freshening is evident in the Andvord Bay near-surface layer, likely as a result of glacial inputs. The combination of surface freshening and the absence of strong mean wind forcing in the fjord results in a salinity stratification which extends well into the euphotic zone, providing advantageous conditions for phytoplankton blooms. Andvord Bay is generally dynamically quiet compared to the ambient ocean, and strong horizontal temperature gradients into the fjord suggest that exchange with the Gerlache Strait is slow. Local katabatic wind events and low-frequency oscillations of the coastal current may be the main mechanisms of water exchange, and the export of large icebergs from within the fjord provides a mechanism to export freshwater, glacially eroded sediments and micronutrients beyond the fjord.

2.1 INTRODUCTION

The western Antarctic Peninsula (wAP) is a climate-sensitive region undergoing large-scale changes in atmosphere and ocean conditions (Vaughan et al., 2003; Meredith and King, 2005; Turner et al., 2005), with consequent impacts on glaciers (Pritchard and Vaughan, 2007; Wouters et al., 2015; Cook et al., 2016) and marine ecosystems (Clarke et al., 2007; Montes-Hugo et al., 2009). Glacio-marine fjords provide a key connection between the Antarctic Peninsula Ice Sheet and the coastal ocean along the wAP, and ocean processes within these fjords may therefore have a disproportionately large influence on the greater region. Furthermore, wAP fjords appear to be hotspots of biological productivity and biodiversity (May et al., 1991; Nowacek et al., 2011; Grange and Smith, 2013), suggesting that the specific ocean conditions in these fjords help provide important habitats for vulnerable marine ecosystems.

Ocean dynamics in glacio-marine fjords can impact ice-ocean interactions and drive mass loss from terrestrial ice sheets (Mortensen et al., 2011; Joughin et al., 2012; Rignot et al., 2012). The resulting link between fjord dynamics and global sea level change has motivated substantial research in the recent years, yielding great advances in the understanding of glacio-marine fjords in Greenland in particular (Straneo and Cenedese, 2015). Comparatively little is known about fjords on the wAP, although the observed retreat of glaciers in the region appears to be driven mainly by ocean processes (Cook et al., 2016). The current paradigm of the physical oceanography of wAP fjords is largely based on geologically motivated studies (Domack and Williams, 1990; Domack and Ishman, 1993) depending on relatively few oceanographic measurements. There is a general lack of direct observations of currents, mixing and hydrographic variability in wAP fjords.

A rich suite of dynamical processes has been shown to be active in high-latitude fjords. Like mid-latitude fjords and estuaries, high-latitude fjords are subject to the influence of winds and tides, both of which can drive ocean circulation and water exchange (Cottier et al., 2010; Mortensen et al., 2011; Spall et al., 2017). Many glacio-marine fjords also encounter significant subglacial meltwater discharge, which can generate buoyancy-driven flow and entrainment of warm external water masses, acting to increase glacial melt (Straneo et al., 2011; Sciascia et al., 2013; Motyka et al., 2013). Low-frequency density fluctuations at the fjord mouth, rather than local forcing, often governs exchange between fjord and shelf waters in deep-silled fjords (Jackson et al., 2014; Sutherland et al., 2014a). Interior mixing in Arctic fjords is often driven by local winds (Skarðhamar and Svendsen, 2010), but can also occur as the result of local ice melt (Azetsu-Scott and Syvitski, 1999; Fer and Widell, 2007), or interactions between tidal or mean flow and topography (Perkin and Lewis, 1978; Mortensen et al., 2011). Rotational effects may play a role in fjord dynamics depending on the morphology and stratification of the individual fjord (Ingvaldsen et al., 2001; Cottier et al., 2010; Johnson et al., 2011).

Many of the conditions which generate the hydrography and dynamics of Arctic fjords are also present along the wAP. Both share the presence of tidewater glaciers, the strong seasonality

in solar irradiance and sea ice cover, and the occurrence of strong wind forcing events. However, there are also some key differences between the physical settings of wAP fjords and their more well-studied Arctic counterparts. For one, subsurface water masses offshore of Arctic fjords are often strongly influenced by relatively warm (+2°C to +10 °C) waters of subtropical origin (Saloranta and Svendsen, 2001; Straneo et al., 2012), while subsurface water masses are colder (-2°C to +2°C) along the wAP (Smith et al., 1999; Martinson et al., 2008; Moffat and Meredith, 2018). Additionally, runoff from wAP glaciers is currently small compared to the Arctic (Vaughan, 2006; van Wessem et al., 2016), where summer freshwater input typically is substantial (Hagen et al., 2003; van den Broeke et al., 2008). The wAP therefore offers the opportunity to extend the study of fjord systems into a less well-studied parameter range, and to a subpolar glaciers system at an earlier stage of atmospheric warming.

The goal of this study is to characterize the physical environment of a wAP fjord, including the hydrographic and glaciological characteristics as well as forcing conditions, ocean energetics and dynamical processes. We present observations from Andvord Bay, a fjord on the northern wAP, collected between November 2015 and March 2017 as part of the *FjordEco* project. The field program consisted of comprehensive shipboard measurements from three research cruises, multiple sub-surface moorings, automatic weather stations, and time-lapse cameras. We use these measurements to describe the meteorological, oceanographic and glaciological conditions in the context of the larger-scale hydrography, and then discuss mechanisms which may play a role in fjord hydrodynamics and the structure and function of the fjord.

2.2 DATA AND METHODS

2.2.1 STUDY SITE

2.2.1.1 *Andvord Bay*

Andvord Bay is a glacial fjord located on the northern wAP (Figure 2.1). The fjord opens into the Gerlache Strait, which separates the main coastline from Anvers and Brabant Islands (Figure 2.1b). Andvord Bay is composed of a main channel which branches into two deep inner coves. It is flanked by two narrow channels, Aguirre Channel and Errera Channel, with minimum depths of ∼100 m and ∼200 m, respectively. For the purpose of this study, Andvord Bay with its opening to the Gerlache Strait was divided into 6 areas with associated labels: *Inner Fjord East, Inner Fjord West, Middle Fjord, Outer Fjord, Mouth* and *Gerlache*. These areas (shown in Figure 2.1c) will be referred to throughout the paper, and unless otherwise stated, *the fjord* can be understood to refer to the area inward of and including the Outer Fjord.

Andvord Bay is surrounded by steep topography and several tidewater glaciers with a total catchment area of $\sim$ 500 km^2 (Cook et al., 2016). The largest glacier is Bagshawe Glacier in Inner Fjord West (250 km^2), followed by Moser Glacier in Inner Fjord East (86 km^2), Deville

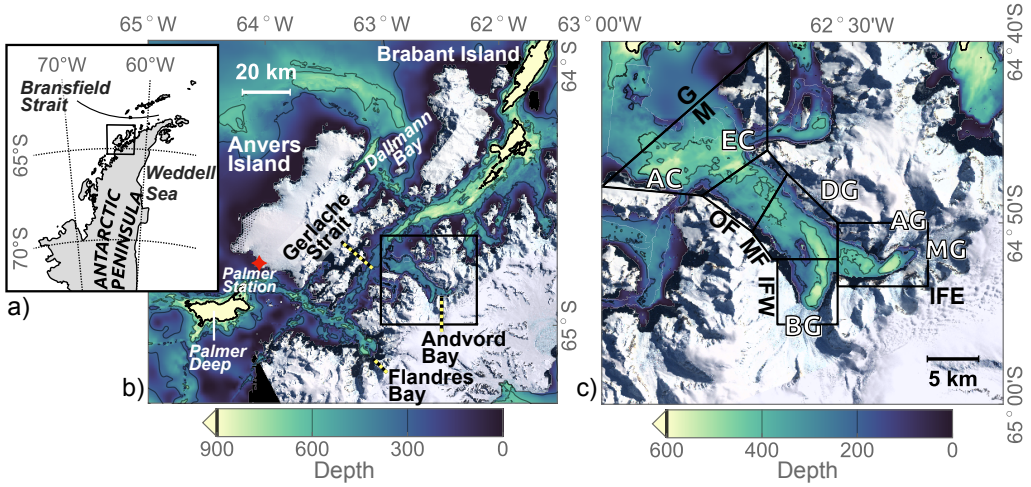

Figure 2.1: *a)* Overview map of location on the Antarctic Peninsula. *b)* Bathymetry of the greater Gerlache Strait area with key geographic labels. *c)* Bathymetry of Andvord Bay. Labelled are major glaciers *(Bagshawe, Deville, Arago and Moser Glaciers)* and side channels *(Errera and Aguirre Channels)*. Black polygons show FjordEco area labels listed in Section 2.2.1.1. Depth contours for *b* and *c* are shown in scale bars below each panel. Bathymetry from Global Multi-Resolution Topography product (Ryan et al., 2009). Land imagery from Landsat Image Mosaic of Antarctica (Bindschadler et al., 2008). Multibeam and imagery data available from the U.S. Geological Survey.

Glacier on the eastern edge of the fjord (35 km^2), and a number of smaller glaciers emptying predominantly into the inner coves. According to Cook et al. (2016), the total catchment area of glaciers terminating in Andvord Bay is changing by an average rate on the order of 100 m^2 yr^{-1}, a very small number suggesting that the glaciers are not actively retreating.

No shallow sill is present at the mouth of Andvord Bay. The bathymetry of the fjord is nevertheless complex, with bottom depths ranging from 70 m at a bathymetric high in the southern part of the fjord, to >550 m in the inner coves. An unobstructed lateral path exists at 370 m depth from these inner basins to the Mouth. Deep waters at the Mouth are further separated from the main channel of the Gerlache Strait, yielding a functional sill depth of 312 m. An elongated depression extends for 5-7 km along the north-south axis in the inner fjord, with the greatest depths found in the basin near the glacier edge in Inner Fjord West. The basin of Inner Fjord East is separated from this elongated depression by a deep (> 370 m) sill. Andvord Bay is 5-7 km wide and ~17 km long as measured from the terminus of Bagshawe Glacier to the Mouth. The total water volume of the fjord is approximately 34 km^3, 62% of which is located above 200 m depth, and 3% below 400 m.

2.2.1.2 *Regional hydrography*

The Gerlache Strait provides an oceanic connection between two distinctly different deep water regimes; the wAP shelf to the south and the Bransfield Strait Basin to the north. On the shelf, the characteristic water mass below 100 to 200 m depth is modified Upper Circumpolar Deep Water

(mUCDW). This water mass is the result of the cross-shelf transport of UCDW from the Southern Front of the Antarctic Circumpolar Current, which flows northeast along the WAP shelf break (Orsi et al., 1995). Once on the shelf, these relatively warm waters cool and mix with local water masses, but retain enough heat to cause the characteristic increase in temperature with depth typically observed from 100 to 200 m depth in profiles on the shelf (Hofmann and Klinck, 1998; Smith et al., 1999; Martinson et al., 2008; Moffat and Meredith, 2018).

In the Bransfield Strait, the subsurface waters are heavily influenced by water masses that originate in the Weddell Sea, and therefore substantially colder than the mUCDW-dominated areas further south (Whitworth et al., 1994; López et al., 1999; Hofmann et al., 1996). The dominant subsurface water mass in the southeastern part of the Bransfield Strait is typically labelled Bransfield Strait Water (BS, BSW). Other authors (e.g., Garcıá et al., 2002; Sangrà et al., 2011) use the label Transitional Weddell Water or Transitional Zonal Waters with Weddell Sea influence (TWW), which seems to overlap at least in part with BS. Previous studies have found the Gerlache Strait to be dominated by water masses from the Bransfield Strait regime, with occasional occurrences of mUCDW (Garcıá et al., 2002).

2.2.2 DATA

2.2.2.1 *CTD profiles and automated shipboard sensors*

Three research cruises were conducted as part of the FjordEco measurement program (Figure 2.2). Extensive physical, biological and geochemical measurements were conducted in the area during *Cruise 1* on the *R/V Laurence M. Gould* in November-December 2015, and during *Cruise 2* on the *R/V Nathaniel B. Palmer* in April 2016. *Cruise 3*, in February-March 2017 was also on the *Gould*. It had the primary purpose of recovering the fixed installations, but a smaller set of shipboard observations and samples was also collected.

275 profiles of Conductivity, Temperature and Pressure (CTD) were collected during the cruises, most of which were within Andvord Bay (Table 2.1a). The CTD measured oxygen in addition to salinity, pressure and temperature. An along-fjord transect of 10 stations from the inner fjord to the Gerlache Strait was repeated during all three cruises, and repeat surveys were performed across the Outer Fjord (Figure 2.2). In addition, both the *Gould* and the *Palmer* have automatic flow-through seawater systems with intakes at 5-7 m depth. An integrated themosalinograph (TSG) provided a continuous record of average near-surface temperature and salinity at 1 minute intervals. Atmospheric variables were also collected by automated ship systems. All CTD and automated shipboard data are publicly available at the Antarctic and Southern Ocean Data Portal of the Marine Geoscience Data System (`www.marine-geo.org/portals/antarctic`, Carbotte et al. (2007)).

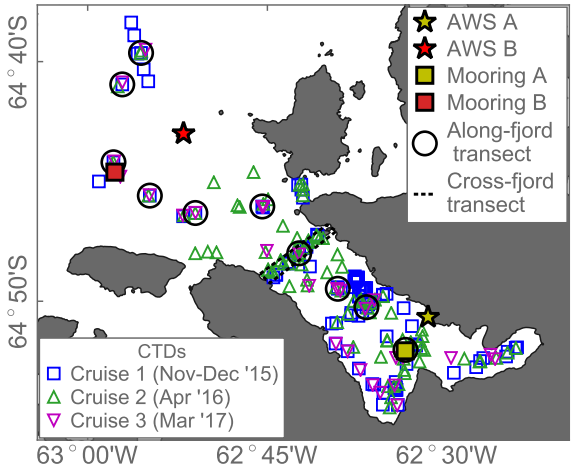

Figure 2.2: Map of key FjordEco observations. A number of additional CTD stations in the Gerlache Strait are not shown.

a) Research cruises

	Cruise ID	*Start*	*End*	*Air temperature*	*CTD (all/fjord)*	*VMP (all/fjord)*
Cruise 1	LMG15-10	23 Nov 2015	22 Dec 2015	1.40°C	125/105	12/11
Cruise 2	NBP16-03	3 Apr 2016	23 Apr 2016	-3.59°C	113/72	22/9
Cruise 3	LMG17-02	26 Feb 2017	9 Mar 2017	0.60°C	37/20	

b) Oceanic moorings

	Location	*Start/end*	*ADCP (depth)*	*Temperature sensor depths*
Mooring A (#1)	Inner Andvord Bay	29 Nov 2015 / 4 Apr 2016	75 kHz (518 m)	199 m, 298 m, 498 m
Mooring A (#2)	Inner Andvord Bay	17 Apr 2016 / 5 Mar 2017	75 kHz (501 m)	301 m, 391 m, 491 m
Mooring B	Gerlache Strait	27 Nov 2015 / 5 Apr 2016	150 kHz (up, 184 m) 300 kHz (down, 184 m)	209 m, 311 m

c) Automatic weather stations

	Location	*Elevation*	*Start*	*End*
AWS A	Inner Andvord Bay	10 m	19 Dec 2015	7 Feb 2017
AWS B	Gerlache Strait	60 m	15 Dec 2015	5 Mar 2017

Table 2.1: Overview of FjordEco data: *a)* Research cruises with mean air temperature measured by ship within the fjord and number of CTD and VMP profiles. *b)* Oceanic moorings with instruments used in this study (both deployments of Mooring A). *c)* Automatic weather stations.

2.2.2.2 *Vertical Microstructure Profiler*

A vertical microstructure profiler (VMP-500) was used to measure turbulent kinetic energy during cruises 1 and 2. The VMP measured vertical velocity shear down to centimeter scale using dual shear probes sampling at 512 Hz. The VMP was allowed to fall freely through the water column at a terminal rate of 67-68 cm s^{-1}. We discarded VMP data from above 50 m; in this range the instrument was still accelerating towards terminal velocity and therefore subjected to significant vibration. Turbulent kinetic energy dissipation ε was calculated from shear variance (Oakey, 1982) integrated within overlapping bins of 1.3 m. At each measurement station, three to four consecutive deployments were performed within a typical time span of one hour. Deployment profiles of ε were taken as the average between the two sensors, and station average profiles were obtained by averaging all deployment profiles within each station. FjordEco VMP data is publicly available from the UCSD Microstructure Database (`microstructure.ucsd.edu`).

2.2.2.3 *Oceanographic moorings*

Two oceanographic moorings equipped with Acoustic Doppler Current Profilers (ADCPs) and SeaBird temperature sensors were deployed during Cruise 1 in November 2015 (Figure 2.2, Table 2.1b). *Mooring A* was deployed in a deep basin near the head of the fjord at a water depth of >500 m. The mooring was serviced and redeployed during Cruise 2, and finally recovered during Cruise 3. The top instruments were lowered from ~200 m to ~300 m depth during the second deployment. *Mooring B* was deployed near the junction of the Mouth area and the Gerlache Strait, at a water depth of ~310 m. Dual ADCPs were mounted near 183 m depth. Mooring B was deployed during Cruise 1, and recovered and redeployed during Cruise 2. Recovery was attempted during Cruise 3, but the mooring did not surface and is presumed lost. FjordEco Mooring data are publicly available from the National Centers for Environmental Information (`http://accession.nodc.noaa.gov/0175451`).

2.2.2.4 *Automatic Weather Stations*

Atmospheric variables were measured by two Automatic Weather Stations (AWSs) which were active from December 2015 to March 2017 (Figure 2.2, Table 2.1c). The AWSs were monitored by the University of Wisconsin-Madison AWS program (Lazzara et al., 2012). *AWS A* was located inside Andvord Bay on the northeastern coast of Inner Fjord East. *AWS B* was located on top of a small island (Useful Island) outside the fjord in the Gerlache Strait. The weather stations measured air temperature, humidity, wind speed and direction and other variables, returning data with 10 minute sampling intervals. This study also used the photo records from two time lapse cameras located on *AWS A*. One camera faced towards the W/NW capturing the middle/outer portion of the fjord. The other was pointed towards Bagshawe Glacier, capturing the innermost part of Andvord Bay. Both cameras operated from December 2015 to December 2016. AWS data are publicly available through the University of Wisconsin-Madison AWS program

(amrc.ssec.wisc.edu/aws). The daily time lapse photos from *AWS A* are available at the U.S. Antarctic Program Data Center (www.usap-dc.org/view/dataset/601111).

We define the *S16* season as the period between Cruises 1 and 2 where all AWS and moorings were simultaneously operative (December 20 2015 to March 5 2016).

2.2.3 DERIVED ESTIMATES

2.2.3.1 *Sea ice cover*

The time lapse photographs from the two cameras at *AWS A* were used to obtain a first-order, semi-qualitative estimate of daily sea ice cover in the fjord, based on daily photos taken near local noon (supporting information, Text S1, Figure S1). For each photograph, the sea ice cover fraction was visually classified as either *0*, *1/3*, *2/3* or *1*. Large icebergs, bergy bits and other ice obviously of glacial origin were excluded, and the estimates were based on the amount of relatively flat ice. Photos were processed in random order in order to minimize bias, and each dataset was processed twice in order to assess the consistency of the method. For both camera records, successive classifications based on the same photo agreed in 85% of the cases, and agreed to within 1/3 in 100% of the cases.

2.2.3.2 *Surface glacier melt*

We estimated surface melt over the catchment area of all glaciers terminating in Andvord Bay based on *Positive Degree Days (PDD)*, which has been shown to be a good first order proxy on the Antarctic Peninsula (Smith et al., 1998). *PDD* was calculated for the discrete temperature step T as (e.g., Braithwaite and Olesen, 1989):

$$\mathrm{PDD} = T\ \mathcal{H}(T)\ \Delta t \tag{2.1}$$

where T is air temperature in °C averaged over a time interval $\Delta t = 3$ hours. $\mathcal{H}(T)$ is defined as 1 for $T > 0$°C and 0 for $T \leq 0$°C. To obtain T at each point, we extrapolated the temperature record from AWS A onto the catchment area assuming a fixed lapse rate of -0.0044 °C m^{-1}, following Vaughan (2006). Topography was obtained from the Global Multi-Resolution Topography Data Synthesis (Ryan et al., 2009), and catchment area outlines were taken from Cook et al. (2014) (supplementary materials, Figure S3).

Surface melt was assumed to be related to *PDD* by a constant factor c_{PDD}. We used a central value $c_{PDD} = 4.7$ kg °C^{-1} day^{-1} m^{-2}, taking typical values for snow and ice (3 and 8 kg °C^{-1} day^{-1} m^{-2}, respectively) as the bounds of the estimate range following Vaughan (2006).

The majority of surface melt is believed to refreeze locally in the firn layer, so *PDD* itself should not be interpreted as direct measure of surface melt available as freshwater input into the ocean. We did not attempt to model the refreezing process, but rather used the overall melt to

runoff ratios estimated for the wAP in the year 2000 by Vaughan (2006), 0.1 to 0.25, as a crude approximation. This parametrization does not capture the dependence of the runoff fraction on the amount of preceding surface melt (Braithwaite and Olesen, 1989).

2.2.3.3 *Heat and freshwater content*

Heat content in the water column between depths $z0$ and $z1$ were calculated as:

$$Q = \int_{z0}^{z1} \rho c_p (\theta - \theta_f)\, dz \tag{2.2}$$

where ρ is water density, θ the potential temperature, and c_p the heat capacity (3987 J kg^{-1} $^{\circ}C^{-1}$). Freezing temperature θ_f was calculated from local salinity (Fujino et al., 1974). Similarly, freshwater content was calculated as:

$$FWC = \int_{z0}^{z1} \frac{S - S_{\text{ref}}}{S_{\text{ref}}}\, dz \tag{2.3}$$

where the reference salinity S_{ref} was set to 34.5, a typical value for the deep waters of the fjord. Average quantities in the fjord were computed by multiplying averages at each depth from all CTDs within the fjord with the estimated total volume per depth estimated from multibeam bathymetry.

2.2.3.4 *Glacier flow rates*

Glacier flow velocities were obtained from an existing ice-flow mapping dataset based on cross-correlation of image pairs from Landsat-8 (Fahnestock et al., 2016), available from the National Snow and Ice Data Center. Ice fluxes from Bagshawe Glacier and the major glaciers in Inner Fjord East were estimated by multiplying flow speeds by bathymetric transects near the glacier termini.

2.3 RESULTS

2.3.1 GLACIERS AND CLIMATE

2.3.1.1 *Winds*

While the Gerlache Strait experiences relatively strong surface forcing from along-strait winds, Andvord Bay is largely sheltered by the enclosing topography (Figure 2.3cef). Average wind speed at AWS B in the Gerlache Strait (7.0 m s^{-1}) was 2.6 times greater than at AWS A (2.7 m s^{-1}) in the period where the records overlap. Corresponding surface wind stress computed from the wind records (after adjusting for sensor elevation) was 3.2 times greater at *AWS B* (0.076 Pa)

than at *AWS A* (0.023 Pa). Some of the difference between the two records may be attributed to the local topographical setting of each sensor, but the observed weak winds within Andvord Bay are consistent with the overall quiet conditions experienced within the fjord during the cruises.

A distinct wind event occurred during Cruise 1, when strong winds were observed blowing out along the axis of the fjord for several days. Shipboard sensors registered wind gusts as high as 30 m s^{-1} in the fjord during the event, and down-fjord winds persisted from December 10th to 15th. AWS A appears to be topographically sheltered from down-fjord winds, but AWS B registered aperiodic episodes of strong winds emanating from the fjord throughout the record, visible in the upper left quadrant of Figure 2.3e. Strong down-fjord winds were consistently associated with a drop in relative humidity, suggesting a terrestrial source region. The wind events are consistent with katabatic flow from the glaciated continental plateau, a known feature of the wind field of the coastal wAP (Parish, 1988). Over the course of the measurement period, AWS B registered 12 separate instances where daily average down-fjord winds were in excess of 10 m s^{-1}, all of which coincided with a drop in relative humidity (Figure 2.3c, supporting information, Figure S2). The strongest events occurred around 13 November 2016 and Jan 11 2016, respectively.

2.3.1.2 *Air temperature and melt*

Air temperatures measured by AWS A (Figure 2.3a) were consistent with previous observations of the current mild climate of the northern wAP (e.g Vaughan et al., 2003; van Wessem et al., 2015). The observed 2016 average temperature was -1.8°C, and daily average temperatures were above freezing for 149 days during the year. Winter temperatures were relatively variable, reaching a minimum daily average of -14.1°C in August 2016, while summer temperatures were comparatively steady at few degrees above zero in December-March.

The annually integrated PDD for 2016 at AWS A was 232 °C days, in the high end of the range observed at nearby Faraday/Vernadsky Station by Vaughan (2006). Total estimated surface melt over the glacier catchment area in 2016, assuming a PDD-factor 4.7 $°C^{-1}$ day^{-1} m^{-2}, was 5.3×10^7 m^3 freshwater equivalent, corresponding to 0.2% of the water volume of Andvord Bay. The bounds of the estimate are 3.4×10^7 m^3 to 9.0×10^7 m^3 using PDD-factors 3.0 and 8.0 $°C^{-1}$ day^{-1} m^{-2}, respectively. Due to the high elevation of most of the catchment area, the majority of the melt occurs near the glacier termini (supporting information, Figure S3).

Surface melt is strongly intensified in the summer season, and the 69% of the year between April 1st and December 10th only accounted for 22% of the total surface melt in 2016. Using a runoff fraction range of 0.1 to 0.25, we obtain a annual freshwater flux range of 2.0×10^3 to 1.3×10^4 m^3 day^{-1}. The corresponding range for the S16 season was an order of magnitude greater than the annual average with 1.9×10^4 to 1.2×10^5 m^3 day^{-1}.

2.3.1.3 *Sea ice cover*

Andvord Bay was largely or partially clear of sea ice during most of 2016 (Figure 2.3d). Sea ice began appearing in March, and increased through the fall, before the fjord froze over completely

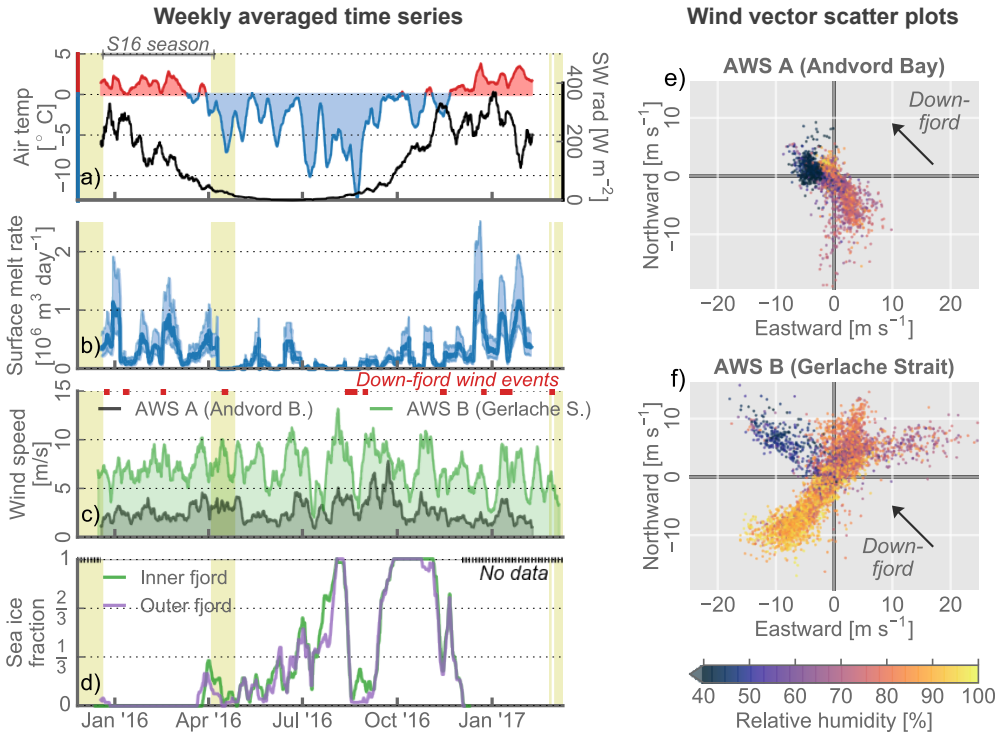

Figure 2.3: Left: Weekly averaged surface quantities in the Andvord Bay area. *a)* Air temperature (red/blue) and shortwave radiation (black) measured by AWS A. *b)* Total catchment area surface melt estimated from AWS A temperature record. Center line is using a PDD conversion factor 4.7 kg $^{\circ}C^{-1}$ day^{-1} m^{-2}, lower and upper bounds using 3.0 and 8.0 kg $^{\circ}C^{-1}$ day^{-1} m^{-2}, respectively. *c)* Wind speed measured by *AWS A* (black) and *AWS B* (green). Timing of wind events (daily averaged down-fjord wind speed >10 m s^{-1}) indicated in red. *d)* Visually estimated sea ice fraction based on time lapse photos from cameras located at AWS A looking towards the inner (green) and outer (violet) fjord. Yellow shading indicates the timing of shipboard measurements within the fjord. Right: Scatter plots of 2-hourly wind components from the records from *e)* AWS A and *f)* AWS B. Direction corresponds to the heading of the wind, e.g. upper left quadrant is to the NW. Colored by relative humidity.

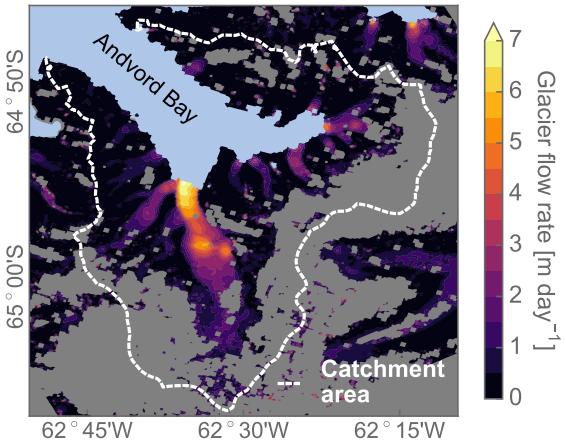

Figure 2.4: Glacier flow rates from Landsat-8 cross-correlation (Fahnestock et al., 2016). Gray zones are areas with large point-to-point error, taken as missing data. White line shows catchment area outline of glaciers terminating in Andvord Bay, from Cook et al. (2014).

in early August. However, sea ice cover then plummeted after less than two weeks, coinciding with a short period of strong, down-fjord winds. Afterwards, the fjord remained largely open until mid-September, when sea ice cover again increased quickly. The fjord was completely covered by fast ice from late September to the end of October. Around November 1st, the fjord began opening, and by the end of the record in early December, the estimated sea ice fraction was near zero.

2.3.1.4 *Solid ice flux*

Glaciers surrounding Andvord Bay are fast-moving, with near-terminus flow rates reaching 7 m day^{-1} for Bagshawe Glacier (Figure 2.4). We estimate a flux of $\sim$1.7 km^3 year^{-1} of solid ice into the fjord, corresponding to a mass flux of 1.6×10^{12} kg year^{-1} for a glacial ice density of 917 kg m^{-3}. Bagshawe Glacier accounts for the bulk of the ice flux ($\sim$1.5 km^3 year^{-1}), and the major Inner Fjord East glaciers for the remaining $\sim$0.2 km^3 year^{-1}. We expect the errors in these estimates to be relatively large due to variations in bathymetry near the terminus.

We observed glacial ice of a large size range within the fjord. Along with brash ice, bergy bits and smaller icebergs, we frequently observed large tabular bergs, often with a freeboard on the order of 30 m and lateral width exceeding 500 m. Given their shape and the surrounding glaciology, we conclude that Bagshawe Glacier is the likely source of the tabular bergs.

2.3.2 HYDROGRAPHY

2.3.2.1 *Water masses*

A CTD transect through the Gerlache Strait during Cruise 3 in March 2017 (Figure 2.5) shows the transition between the two regional water mass regimes through the Strait. Salinity below

300 m decreased by nearly 0.02 from the southwestern end of the transect to the northeastern end, but the transition is most notable in temperature, which decreased from 1.0°C to below -0.75°C. The gradient was strongest in the area between Andvord Bay and Flandres Bay, where the Gerlache Strait narrows and shoals to a sill with a minimum depth of approximately 320 m. Temperature decreased towards the northeast at a rate of -0.025 C km^{-1} at 250 m depth in the area of the transect between the fjord. The along-strait gradient weakened above 200 m depth, and the 1°C isotherm was located near 100 m depth throughout most of the transect. A larger degree of lateral exchange near the surface would be consistent with previous observations of an alongshore current flowing towards the northeast in the upper layers of the Gerlache Strait (Zhou et al., 2002; Beardsley et al., 2004). The upper waters were anomalously warm during the transect, with temperatures of 1.3°C to 2.5°C in the upper 50 m, increasing towards the wAP shelf.

The mouth of Andvord Bay is located at the northern edge of the Gerlache Strait sill. The deep waters outside Andvord Bay are therefore dominated by Bransfield Strait water masses, and ocean temperature tends to decrease with depth. θ-S diagrams from the three FjordEco cruises (Figure 2.6) show that deep waters in Andvord Bay always lie within the literature range of BSW. The same is usually true for the deepest waters in the Gerlache Strait in the region outside the fjord, but we did observe θ-S properties tending towards mUCDW in this area during the first cruise in spring 2015. Temperature was elevated in a broad subsurface maximum centered near 150 m, reaching a maximum of 0.68°C (Figure 2.7a, d). The warm anomaly was correlated with a clear oxygen minimum (<210 μmol kg $^{-1}$, compared to >250 μmol kg $^{-1}$ at similar depths in Andvord), a well-known characteristic of mUCDW (Garcıá et al., 2002; Carter et al., 2008). We found no obvious mUCDW signature in θ-S and oxygen inside Andvord Bay at any time, or in the Gerlache area during the two later cruises.

Repeat CTD transects from the three cruises (Figure 2.7) illustrate longitudinal gradients in temperature and salinity from the Gerlache Strait into Andvord Bay. We observed no clear overall depression of isohalines into the fjord indicating strong estuarine circulation. As illustrated in Figure 2.7, strong instantaneous salinity gradients existed in the upper waters, but no significant along-fjord salinity trend emerges from the cruise average CTD and TSG measurements (Figure 2.9). Clear temperature gradients between Andvord Bay and the Gerlache Strait were found during all cruises, typically associated with cooling into the fjord. Due to the low temperatures in the area, density of the ocean waters is primarily a function of salinity, so relatively large lateral temperature differences do not necessarily generate strong pressure gradients.

Many temperature profiles from the inner fjord exhibited vertically localized cold anomalies, typically 0.1°C to 0.2°C colder than the surrounding waters. These cold anomalies were mainly found in the upper 50 to 200 m range, and are visible as near-vertical θ-S intrusions between the 27.4 kg m^{-3} and 27.6 kg m^{-3} isopycnals (Figure 2.6). This study does not deal with this signal in detail, but we note that our observations are consistent with the "cold plumes" described by Domack and Williams (1990).

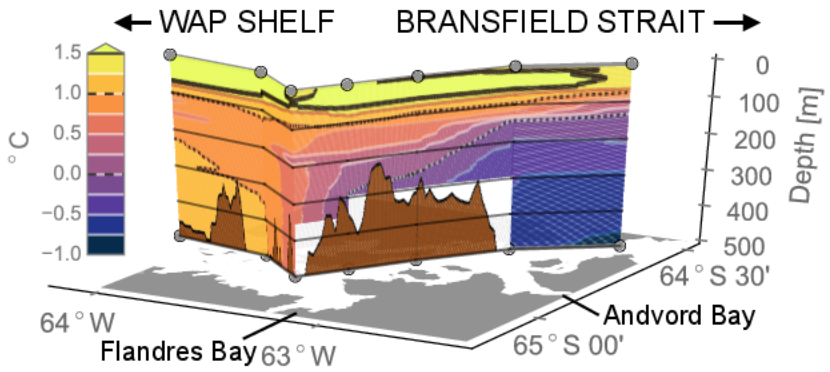

Figure 2.5: Ocean temperature between 0 and 500 m through the Gerlache Strait on March 3, 2017. Grey dots show station locations on the underlying map. Underlying bathymetry (not maximum strait depth) shown in brown. Temperature scale capped at 1.5°C for emphasis of the deep gradient.

Deep basin waters in Inner Fjord East were slightly colder and fresher than in Inner Fjord West, but the differences were small compared to changes between cruises. Oxygen concentrations in the deep basins ranged from 236 to 267 μmol l^{-1} during all cruises, well above typical sublethal thresholds for benthic organisms (e.g. Vaquer-Sunyer and Duarte, 2008).

We interpret the overall vertical structure of the fjord as a three-layer one, shown in average profiles from within the fjord in Figure 2.8. In the upper 80 m, temperature and salinity were highly variable, below 300 m they are relatively stable and vertically uniform. Between these two layers, we generally observed a gradual transition with depth, although temperature in this range was frequently affected by cold intrusions in the inner parts of the fjord. The properties of the bottom layer generally extended down into the deep fjord basins, where temperatures ranged from -1.0°C to -0.6°C and salinities from 34.49 to 34.54.

The first internal radius of deformation, calculated from cruise average profiles of the density above 400 m depth, range from 2.7 km during Cruise 1 to 3.7 km during Cruise 3. As the deformation radius is smaller than the fjord width, rotational effects can be expected to be of importance to the fjord dynamics (e.g. Cushman-Roisin et al., 1994).

2.3.2.2 *Seasonal variability*

Water properties in Andvord Bay differed significantly between the cruises. The interior waters of the fjord were cold and saline during Cruise 1 (early spring) compared to Cruise 2 and Cruise 3 (late summer/fall, Figure 2.8a). The surface layer of the fjord, on the other hand, was warmest during *Cruise 3* in March 2017, after an extended period of surface temperatures above zero, and coldest in April 2016, during which the weekly average air temperature reached a minimum of -6°C.

These seasonal changes are reflected in the heat content Q in the fjord (Figure 2.9cd). The heat content in the upper 80 m was significantly greater during Cruise 3 than during the two previous

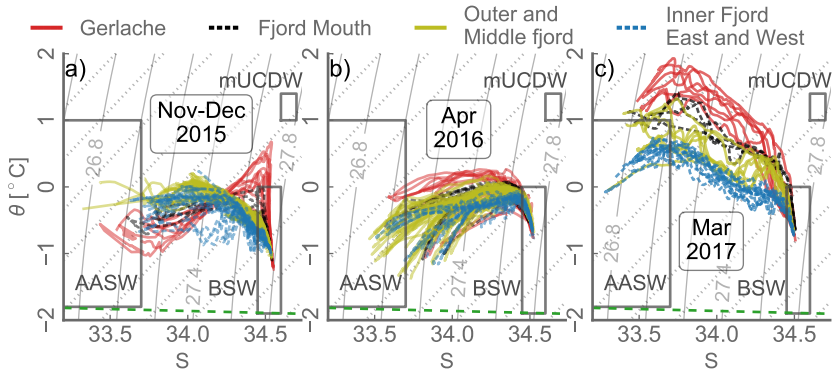

Figure 2.6: Scatter plots of potential temperature θ and salinity S from CTD profiles during FjordEco CTD profiles. Colors indicate the fjord areas where the profile was taken (Figure 2.2). Solid lines show isopycnals, dotted lines show "melt lines" (Gade, 1979). Green dashed line shows freezing point. Reference water masses based on Smith et al. (1999) in black squares.

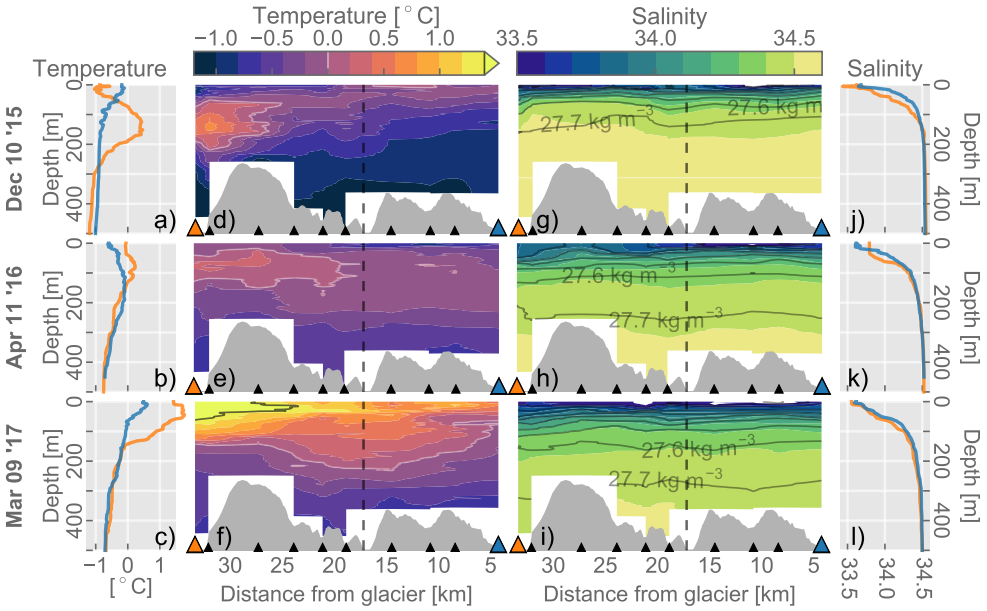

Figure 2.7: Along-fjord CTD transects from the Gerlache Strait into Andvord Bay during Cruise 1 (top), Cruise 2 (middle), and Cruise 3 (bottom). *a-c)* Potential temperature profiles at the Gerlache Strait *(orange)* and Andvord Bay *(blue)* ends of the transects. *d-f)* Contours of potential temperature. *g-i)* Contours of salinity. Overlaid are isopycnals spaced by 0.1 kg m^{-3}. *j-l)* Salinity profiles at the Gerlache Strait *(orange)* and Andvord Bay *(blue)* ends of the transects. Dashed line shows location of fjord entrance. Station locations shown in Figure 2.2.

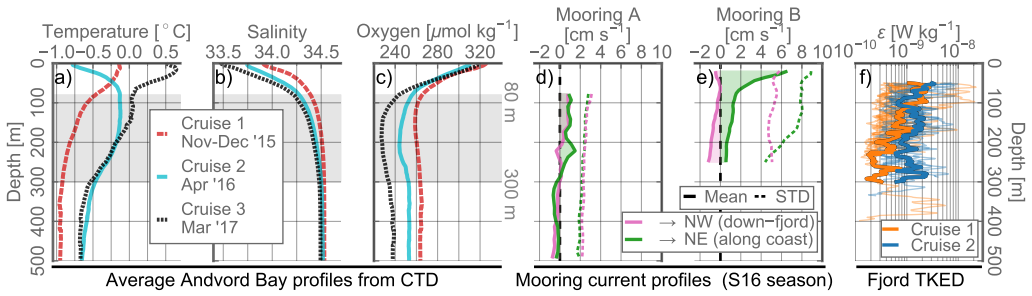

Figure 2.8: *Left:* Cruise average profiles of in-situ temperature *(a)*, salinity *(b)* and oxygen *(c)*. Computed from means of all profiles within Andvord Bay (excluding Mouth area) after smoothing with a 5-m binomial filter in the vertical. *Middle:* time mean and standard deviation of current components during the S16 season from *(d)* Mooring A in inner Andvord Bay, and *(e)* Mooring B in the Gerlache Strait. *Right (f):* Profiles of turbulent kinetic energy dissipation (TKED), ε, within the fjord. Cruise average profiles between 50 and 300 m shown in thick lines.

cruises. Heat content below 80 m stands out as anomalously low during Cruise 1. The total, volume-integrated heat associated with above-freezing ocean temperatures in the fjord increased from 1.67×10^{14} J during Cruise 1 to 2.12×10^{14} J during Cruise 2, and further to 2.43×10^{14} J during Cruise 3. Total freshwater content in the fjord (relative to a reference salinity of 34.5) doubled from Cruise 1 (8.1×10^7 m^{-3}) to Cruise 2 (1.72×10^8 m^{-3}), and further increased to Cruise 3 (2.30×10^8 m^{-3}). This freshening was surface-intensified, but extended throughout the water column (Figure 2.9efg).

The down-fjord wind event in mid December 2015 coincided with a significant increase in salinity in the upper layer of the fjord, and a corresponding reduction in freshwater content (Figure 2.9a, e-g). In addition, near-surface temperatures increased in the Inner Fjord after the event (Figure 2.9b). Upper ocean salinity remained elevated at least one week after the cessation of the wind forcing.

2.3.2.3 *Upper ocean*

Salinity stratification was concentrated in the upper layer, and a well-defined mixed layer was often absent. Average mixed layer depth (MLD) calculated from all fjord CTD profiles (using a threshold of $\Delta\sigma_\theta$ >0.02 kg m^{-3} relative to the minimum potential density σ_θ) was 12.7 m (supporting information, Figure S4). MLD was less than 10 m in 47% of the cases, and less than 20 m in 80%. A significant exception to this was found during the December 2015 wind event, during which a well-defined mixed layer extended down to nearly 60 m. The upper ocean restratified within hours to days after the forcing subsided.

Anomalously cold and fresh water was found along the southwestern coast of the Outer Fjord during Cruise 2 (Figure 2.10). The cross-fjord gradients were largely restricted to the upper 40 m, and no similar signal was observed in cross-fjord transects from the same area during Cruise 1. Upper ocean water mass characteristics were also unique during Cruise 2 in that a large fraction of $\theta - S$ curves showed a clear tendency of aligning with "melt lines" (Gade, 1979) above the 34.0

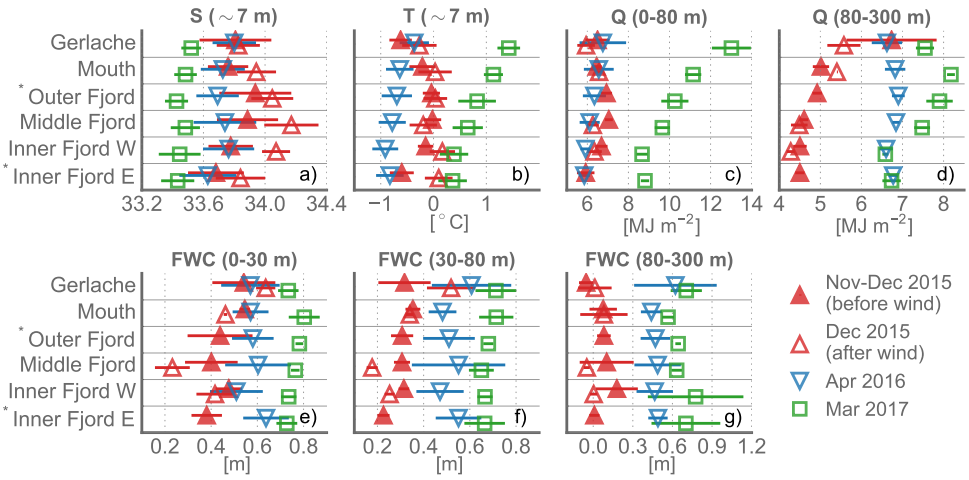

Figure 2.9: Average quantities within defined areas in and outside Andvord Bay (Fig 2.1c) during the three FjordEco cruises: Salinity *(a)* and temperature *(b)* from ship TSG; heat *(c, d)* and freshwater content *(e, f, g)* integrated over the labelled depth ranges, calculated from CTD profiles within each area. Symbols show cruise averages, error bars extend one standard deviation from the mean. Cruise 1 in 2015 has been subdivided into measurements before and after a large wind event starting December 11th. *No available CTD data after the wind event.

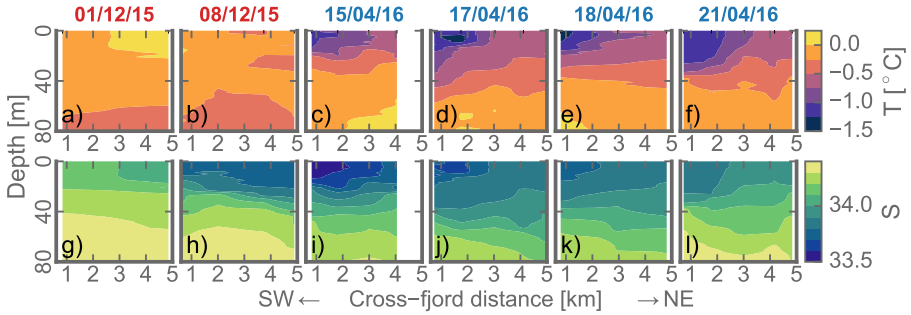

Figure 2.10: Upper ocean temperature (top) and salinity (bottom) from cross-fjord transects in outer Andvord Bay. *a-b, g-h* from Cruise 1, *c-f, i-l* from Cruise 2.

isohaline (Figure 2.6b). This tendency appears to have evolved during the latter half of the cruise, and was also observed in the upper ocean outside the fjord. The alignment of the upper ocean $\theta - S$ distribution with melt lines suggests ongoing ocean-driven melt, which could occur as a a result of melting of sea ice or ice of glacial origin.

2.3.3 MOORING RECORDS

2.3.3.1 *Currents*

Mean currents at Mooring B were influenced by the Gerlache Current, expressed as a surface-intensified mean flow towards the northeast (Figures 2.8e, 2.12abc). Currents decayed with depth towards an eastward flow on the order of 1 to 2 cm s^{-1} below 100 m. Within the measurement

range at Mooring A in Andvord Bay, mean flow was dominated by a weak, two-layer pattern, with northward flow above 300 m and southward below (Figure 2.11b, 2.12bcd). The associated average current speeds were on the order of 1 cm s^{-1}. The two-layer structure corresponds approximately to the hydrographic shift between a relatively uniform lower layer to a transitional middle layer near 300 m.

Currents at both mooring locations underwent low-frequency fluctuations including reversals of the flow direction (Figure 2.11ab, supporting information, Figure S5). At Mooring B, this slow modulation of the currents occurred at all depths, but the near-surface currents appeared largely decoupled from the currents below 65 m (Figure 2.11a). At Mooring A, the low-frequency variability was largely constrained to the upper 300 m. The time series from both moorings exhibit oscillatory behavior with a sub-monthly scale. Velocity spectra from both moorings (supporting information, Figure S6) exhibit broad peaks consistent with elevated energy for oscillations with a period of ∼20 days. We find no strong statistical relationship between the mooring records during the 4 months where they overlap.

Deep water temperatures at Mooring A underwent a clear seasonal cycle, warming gradually by ∼0.5°C between December 2015 to May 2016, cooling abruptly from July to September, and warming again in the following spring (Figure 2.11d). Temperature at 298 m reached a maximum in May-July, suggesting a phase lag of approximately 5 months relative to the seasonal cycle in solar radiation. Near the bottom at 498 m, the phase lag was further extended by approximately one month. While a full annual record is not available from Mooring B, the data from December 2015 to April 2016 showed a similar warming at the two mooring locations, indicating a seasonal temperature cycle in the deep waters inside and outside the fjord. However, temperature variability at all time scales was much greater at Mooring B, as seen in the fine structure of the time series. Temperature variance at Mooring B (after applying a biweekly high-pass filter) was 8.8 times that of Mooring A near 200 m depth, and 3.8 times greater near 300 m depth.

2.3.3.2 *Tides*

The tidal component of the flow was obtained by performing a harmonic fit of the 11 primary tidal constituents to the depth-averaged time series within the S16 season. Tidal currents at Mooring B were primarily directed in the along-strait direction (Figure 2.12e), with an average tidal current amplitude of 5.0 cm s^{-1}. At Mooring A, the average tidal current amplitude was 0.4 cm s^{-1}. The semi-diurnal M_2 constituent dominated the tidal currents at Mooring B, followed in order by the S_2, K_1 and O_1 constituents. In contrast, the diurnal constituents at Mooring A were significantly greater than the semidiurnal. Diurnal amplitudes at Mooring A were greatest between 300-500 m. This vertical structure could indicate the presence of baroclinic diurnal tides, which may interfere constructively or destructively with the barotropic tide at various depths, although the amplitudes of each of the O_1 and K_1 constituents in this maximum are only ∼0.6 cm s^{-1}.

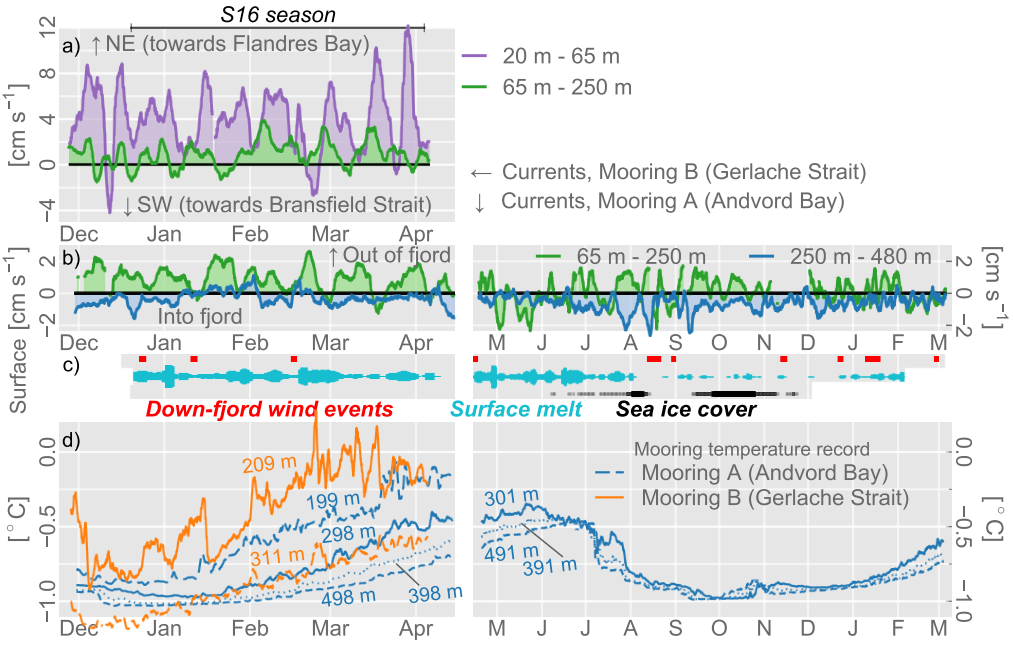

Figure 2.11: FjordEco mooring record, November 2015 to March 2017. Note the change in x-axis scale between the left and right panels. *a)* Along-shore currents from Mooring B in the Gerlache Strait. *b)* Along-fjord currents from Mooring A in Andvord Bay. *c)* Indices of surface conditions (see Figure 2.3). *d)* Deep ocean temperatures from the two moorings at different depths. Currents, runoff index and temperatures smoothed in time with a 3-day running average.

2.3.3.3 *Deep temperature record*

Records from the deep temperature sensors (Figure 2.11d) are consistent with the temperature range observed in CTD profiles during the cruises. Deep fjord temperatures increased gradually from January 2015 to July 2016, when they abruptly cool by ∼0.25°C. This rapid cooling does not correspond to a strong signal in the records of currents or surface forcing. However, the temperature drop occurs in what appears to be a time of sea ice formation, and could therefore conceivably be related to brine rejection.

2.3.4 INTERIOR DIAPYCNAL MIXING

Turbulent kinetic energy dissipation ε estimated from microstructure profiles inside the fjord was typically on the order of 10^{-9} W m^{-2} throughout the measurement depth range during both Cruise 1 and Cruise 2 (Figure 2.8f). Occasional, localized patches of elevated ε did occur, but a detailed investigation of such individual features would require a targeted sampling scheme beyond the scope of this study. Suffice it to say for our purposes that turbulent mixing was not an active or important process in the interior waters during our measurements. To obtain an order

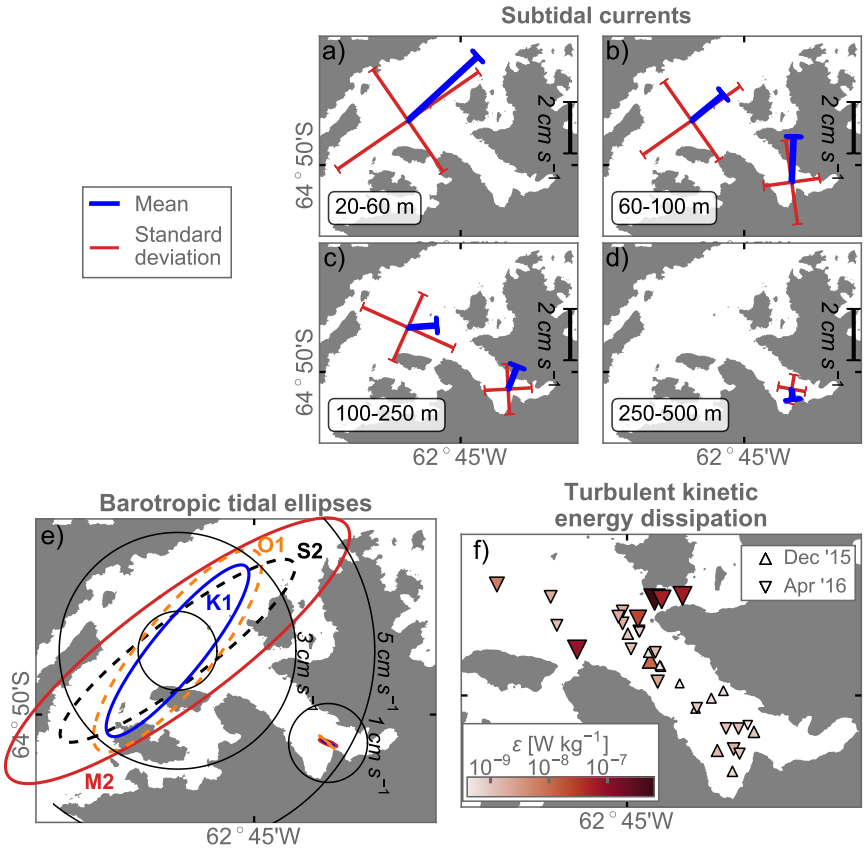

Figure 2.12: *a-d)*: Average sub-tidal currents (low-passed with a 1 day rolling average) at various depth ranges. Blue bar shows the mean vector, red bars show the principal axes, extending one standard deviation from the center. *e)* Ellipses of the four major constituents calculated from depth-average currents where the two records overlap (60-250 m). *f)*. Average turbulent kinetic energy dissipation between 50 and 100 m depth from VMP measurements.

of magnitude estimate of vertical mixing, we compute diapycnal eddy diffusivity κ_ρ, which is typically expressed as a linear function of turbulent kinetic energy dissipation ε:

$$\kappa_\rho = \frac{\Gamma \varepsilon}{N^2} \tag{2.4}$$

where the *mixing efficiency*, Γ, is typically taken as 0.2 (Peltier and Caulfield, 2003), and N is the buoyancy frequency. Using fjord average profiles of ε and N^2 between 50 and 250 m, we obtain diapycnal diffusivities ranging from 6.5×10^{-6} to 5.9×10^{-5} m^2s^{-1}, with averages 2.2×10^{-5} m^2s^{-1} and 2.7×10^{-5} m^2s^{-1} during Cruise 1 and Cruise 2, respectively. This order of magnitude is typical of the relatively quiet interior global ocean (e.g., Waterhouse et al., 2014), and not indicative of energetic mixing which is often observed in coastal environments (e.g., Gregg et al., 1999; Lien and Gregg, 2001).

While microstructure sampling during Cruise 1 was focused inside Andvord Bay, a number of profiles were also collected in the Mouth area during Cruise 2 (Figure 2.12f). Among these was a measurement station in the narrow Errera Channel, which revealed ε levels between 10^{-7} and 10^{-6} m^2s^{-1}, more than two orders of magnitude higher than typical profiles from the fjord. Further measurements in Errera Channel as well as Aguirre Channel across the fjord mouth were performed later during the same cruise, yielding ε values in the 10^{-8} to 10^{-7} m^2s^{-1} range above 100 m, lower than the initial profile but still high compared to other profiles from the cruise. Strong tidal flows were frequently observed transporting large icebergs in and out of these side channels, suggesting that the channels may be sites of tidal energy conversion.

2.3.5 DYNAMICAL SCALING

The dynamics governing fjords and estuaries vary between different systems based on forcing, stratification and geometry. In order to place Andvord Bay within this framework, we evaluated some common parameters used to scale various dynamical processes in fjords, following (Sutherland et al., 2014b). The various parameters were developed empirically from observations of specific systems, or simple physical models which may or may not be representative of fjords like Andvord Bay, and the low amplitudes we observe greatly increase the relative errors in the parameters. We based our estimates on measurements from the two first FjordEco cruises, as well as from the moored records during the S16 season, with the goal of obtaining a scaling of the circulation in Andvord Bay during the summer season.

The importance of freshwater forcing is typically quantified using the *freshwater Froude number*, F_f (Geyer and Ralston, 2011). In systems with large values of F_f, freshwater inputs can be expected to contribute strongly to the dynamics. F_f can be expressed as:

$$F_f = \frac{U_f}{2c} \tag{2.5}$$

where U_f is the barotropic current due to freshwater runoff and c the fastest internal wave speed. We estimated the former as $U_f = Q_r / A_C$, where A_C is the cross-sectional fjord area and Q_r the freshwater flux into the fjord. Q_r was approximated from the average runoff estimated from PDD using an average PDD-factor of 4.7 kg $^{\circ}C^{-1}$ day^{-1} m^{-2} and a runoff fraction of 0.25. c was calculated as the first baroclinic wave speed based on the fjord average stratification. We obtained freshwater Froude numbers on the order of 10^{-6}, suggesting that the overall effect of freshwater forcing on the fjord dynamics is very small in Andvord Bay.

The relative importance of wind forcing relative to buoyancy forcing is often estimated using the the *Wedderburn number* W (Geyer, 1997):

$$W = \frac{\tau_x L}{\beta_s \Delta_x S g H_u} \tag{2.6}$$

where τ_x is the wind stress in the along-fjord direction, L the fjord length, g the gravitational acceleration, β_S the haline contraction coefficient, and $\Delta_x S$ the average along-fjord salinity difference averaged over an upper layer of height H_u. We take H_u as the depth of the previously defined upper layer, 80 m, and $\Delta_x S$ the average salinity increase from the Inner Fjord to the Mouth. During Cruise 1, $\Delta_x S$ was in fact negative, probably due to the effects of the December 2015 wind event as well as the weak meltwater influence. Using instead the difference from Cruise 2, we get a very small value of $\Delta_x S$ (0.005). Taking τ_x as the average fjord wind stress based on AWS A wind record (0.02 N m^{-1}), we obtain W of 1.5. We could therefore expect buoyancy-driven and wind-driven circulation to be of similar importance, although both are much smaller than what is commonly found in comparable fjord systems in the Arctic (e.g. Sutherland et al., 2014b). If we instead use the maximum wind stress based on shipboard winds during the December 2015 wind event (0.65 N m^{-1}), we obtain $W = 40$. As such, wind-driven flow is likely to dominate during strong events, although the dynamics of such short-period events likely differ from those during steady forcing, and the Wedderburn number may therefore not be an appropriate measure of the dynamics during such events (Spall et al., 2017).

In many fjords, particularly those with no shallow sill, volume exchange is largely driven by low-frequency density fluctuations at the fjord mouth, driving a volume flux Q_i in the fjord. A

conventional method for estimating Q_i is an evaluation of the following expression (Stigebrandt and Aure, 1990):

$$Q_i = \beta\sqrt{B_m H_t A_f g \rho^{-1} \Delta M} \tag{2.7}$$

where β is an empirical constant (1.7×10^{-3}), B_m the minimum of the fjord width or the first internal radius of deformation, H_t is the sill depth, A_f the surface area of the fjord, ρ a mean density, and ΔM the depth-integrated standard deviation of the water column density outside the fjord:

$$\Delta M = \int_{-H}^{\eta} STD\big(\rho(z)\big)dz \tag{2.8}$$

This expression was empirically derived in Stigebrandt and Aure (1990) based on studies from Norwegian fjords, but was found in Sutherland et al. (2014b) to agree reasonably well with other methods in Greenland fjords. Evaluating (2.7) and (2.8) based on 24 CTD profiles taken in the Gerlache Strait outside Andvord Bay during Cruises 1 and 2 (excluding the change in mean profiles between cruises), and integrating from $H = 317$ m to the surface, gives an estimated volume flux $Q_i = 7.3\times10^3$ m^3 s^{-1}. This value is one order of magnitude lower than the value of Q_i reported for two Greenland fjords by Sutherland et al. (2014b) (where ΔM and A_f were both significantly larger than in Andvord Bay), but 4 orders of magnitude greater that the estimated summer freshwater runoff into Andvord Bay. The estimated velocity $U_i = Q_i / A_C$ associated with externally forced circulation in Andvord Bay (0.5 cm s^{-1}) is less than half of the observed mean amplitude of the detided along-fjord currents between 65 and 250 m measured by Mooring A (1.2 cm s^{-1}).

2.4 DISCUSSION

In this section, we summarize our current knowledge of the physical environment of Andvord Bay based on the results outlined above. In the concluding section, we summarize the main findings of the study, and outline research which we believe can further expand our knowledge of wAP fjords.

2.4.1 WATER MASSES AND RELATIONSHIP TO GLACIERS

A sill in the southern part of the Gerlache Strait appears to inhibit exchange between the colder BSW water mass regime to the north and the warmer, mUCDW-influenced regime to the south. As a result, deep waters in Andvord Bay are dominated by BSW, and temperature in the interior

waters of the fjord decreases with depth to a cold layer of -1°C to -0.5°C below 300 m. Deep water temperatures in the fjord do undergo significant changes between cruises, with a near doubling of the heat content relative to freezing below 80-300 m from spring to late summer. This does not appear to be related to the inflow of a distinct external water mass, although the rapid temperature fall in the deep waters of the inner fjord in fall/early winter could be an indication of overflow of colder waters from the outside, or local overturning due to local sea ice formation. At no point do we observe the increase in temperature with depth below the pycnocline typical of coastal waters further south along the wAP (Clarke et al., 2008; Santini et al., 2018) and of most Greenland fjords (Mortensen et al., 2011; Sutherland et al., 2014b).

Terminus retreat rates of wAP glaciers are strongly correlated with ocean temperature below 150 m, and the cold northern regime, including Andvord Bay, stands out as an area on the wAP where glaciers are *not* currently in rapid retreat (Rau et al., 2004; Cook et al., 2016). In contrast, neighbouring Flandres Bay, located only a few tens of kilometers to the south, is situated in the warmer southern regime and is experiencing rapid glacial retreat (Cook et al., 2016). It is possible that the Gerlache Strait sill isolates the deep waters of Andvord Bay and other bays and fjords in the northern water mass regime from the influence of mUCDW, making glaciers in the area resistant to ocean-driven retreat. However, mUCDW has been observed in the Gerlache Strait in earlier studies (Garcıá et al., 2002), and a warm mid-water intrusion with water mass characteristics tending clearly towards mUCDW was observed outside Andvord Bay in spring 2015. The intrusion depth of 100 to 200 m is consistent with a "warm tongue" resulting from an overflow across the Gerlache Strait sill, although mUCDW could also originate from Dallmann Bay or the western Bransfield Strait. Further research into the ocean dynamics of the Gerlache Strait area would be required to assess water mass pathways in the region, and to determine whether deep water temperatures near the glaciers in Andvord Bay and elsewhere on the northern wAP may be sensitive to changes in the large-scale regional circulation.

During our measurements, Andvord Bay was only completely covered by fast ice for 1 to 2 months during winter. Surface waters were therefore open to the influence of the atmosphere throughout most of the year. Temperature variability in the upper water column was large, with near-surface temperatures in the fjord ranging from -1.4°C to +1.2°C. Near-surface ocean temperatures appear to be set mainly by air-sea heat transfer, as evidenced by the near-surface temperatures of -0.8°C in April 2016 and +0.5°C in March 2017 following extended periods of low and high air temperature, respectively. High temperature variability is a typical feature of AASW, the broadly defined water mass near the surface along the wAP (Smith et al., 1999; Barnes et al., 2006). The highest observed ocean temperatures during the FjordEco program (measured near the surface in the Gerlache Strait in March 2017) exceeded +2.0°C, well beyond the upper bound of +1.0°C which typically defines AASW (Smith et al., 1999; Klinck et al., 2004). However, similarly high summer temperatures have previously been observed in near-shore waters along the wAP (Barnes et al., 2006; Venables and Meredith, 2014). Surface waters enclosed by complex

coastal topography along the wAP coast may warm more efficiently due to the long residence times and weak wind-driven vertical mixing compared to waters further out on the shelf.

Mass flux into Andvord Bay from the surrounding glaciers occurs almost entirely through calving of icebergs. We estimate a rate of solid ice input from the main glaciers into Andvord Bay of 2×10^{12} kg yr^{-1}, while our estimates of freshwater runoff during 2016 based on extrapolation of the temperature record over the glacier catchment area range from 4×10^{9} to 2×10^{10} kg yr^{-1}. Although the errors associated with these estimates are large, it seems clear that mass flux into the fjord in the form of solid ice greatly exceeds the liquid freshwater contributions. Given the cold ambient waters, icebergs can survive over years to decades (Neshyba and Josberger, 1980), and most larger bergs are likely exported from the fjord before melting. The coastal circulation outside Andvord Bay is predominantly northward, and connects downstream to the Bransfield Current (Huntley and Niiler, 1995; Zhou et al., 2002; Sangrà et al., 2011), providing a path for exported icebergs all the way to the southern reaches of Drake Passage. As such, iceberg export may be the main transport mechanism for terrigenous material like sediment (Gilbert, 1990) and trace metals (Raiswell et al., 2008; Duprat et al., 2016) out of the fjord.

We have found no evidence for a turbid surface meltwater plume during the process cruises or in time lapse photo records, and near-surface salinity rarely dipped below 33.5 even in the summer season. The lateral salinity gradient between Andvord Bay and the Gerlache Strait is small, and overshadowed by the freshening that occurs in the broader region during the summer season. From this, we conclude that the fjord was not subject to strong freshwater forcing during the periods of measurement, and that Andvord Bay does not stand out as a significant freshwater source for the surrounding region despite the relatively large catchment areas of its surrounding glaciers. However, we do observe the signature of meltwater mixing with ambient water in upper-ocean θ-S diagrams from April 2016, and we find clear cross-fjord salinity and temperature gradients in transects near the outer fjord during the same cruise. The latter is qualitatively consistent with rotationally deflected export of meltwater along the southern edge of the fjord, although it could conceivably be associated with tidal flows due to the proximity to the Errera and Aguirre Channels.

Profiles from the inner parts of Andvord Bay show mid-water low temperature anomalies, visible as downward anomalies in θ-S diagrams and similar to the "cold plumes" previously reported in the fjord (Domack and Williams, 1990). Presumably of glacial origin, such plumes could conceivably generate a flux of deep waters and glacially eroded sediment upwards in the water column from the base of the glacier. It is unclear whether the mechanism of tidal heaving of the glacier terminus hypothesised by Domack and Williams (1990) is consistent with the generally weak tidal amplitudes observed in the fjord. This study does not deal with ice-ocean interactions in detail, but provides oceanographic and glaciological context for future studies which will further examine the characteristics of these plumes.

2.4.2 ENERGETICS

The primary observation from our measurements of currents and turbulence is that Andvord Bay is a low-energy environment. Mean and tidal circulation in the fjord mooring are both on the order of a few cm s^{-1}, and mid-water sub-monthly temperature variance in the fjord is only 11% of that outside. Although subsurface mean currents in the overlapping depth range are of similar amplitude in the two moorings, tidal currents in the mooring outside the fjord are an order of magnitude higher than inside the fjord, and as a result, the average kinetic energy increases by nearly an order of magnitude from inside the fjord to outside. Our mooring records do not capture the surface circulation in the fjord, but a previous drifter study of the Gerlache area (Zhou et al., 2002) has shown that surface layer residence times in bays and enclosed areas can be much greater than in the main channel of the Gerlache Strait. In combination with the observed weakening of winds into the fjord, we conclude that Andvord Bay is largely shielded from the energetic conditions outside the fjord.

The idea of Andvord Bay as dynamically quiet is further supported by the low turbulent kinetic energy dissipation ($\varepsilon \sim 10^{-9}$ W kg^{-1}) measured in the interior waters. Although the observations are scattered in space and time, we conclude that strong background mixing from, e.g., internal tide breaking likely does not take place in Andvord Bay, consistent with the absence of a prominent shallow sill. In contrast, we observe strongly elevated turbulent kinetic energy dissipation (up to 10^{-6} W kg^{-1}) in the area directly outside the fjord, in particular near Errera and Aguirre Channels. We hypothesize that the funneling of tidal flows through these narrow constrictions drive tidal energy conversion and vigorous local diapycnal mixing in the vicinity of the channels. Although the details of such a process are beyond the scope of this study, this raises the possibility that "mixing hotspots" outside the fjord provide a pathway for nutrients and higher salinity upward in the water column, from which they can be distributed laterally into the fjord.

Subtidal currents in the Gerlache Strait mooring have a dominant characteristic time scale of 20 to 30 days. The same is true for the mooring in Andvord Bay, although the overall correlation between the records is weak. We find no clear relationship between the currents and the local wind field at this time scale, so the origin of this characteristic time scale is unclear. One plausible source of the observed oscillations is eddying of the Antarctic Peninsula Coastal Current (APCC) of which the Gerlache current is likely a retroflected branch (Moffat et al., 2008). Another is the passage of coastal waves generated by remote forcing (e.g. Wang and Mooers, 1976), which have been shown to drive exchange in Arctic fjords (Inall et al., 2015). Coastal waves have been shown to propagate over long distances along the Antarctic margin, although typically with periods on the order of days rather than weeks (Jensen et al., 2013; Spence et al., 2017). Overall, our observations show that an improved knowledge of the larger scale circulation and low-frequency wave field is necessary to understand the external drivers of exchange between Antarctic fjords and the exterior ocean.

2.4.3 EXCHANGE WITH THE OUTSIDE OCEAN

In contrast to many other fjords, Andvord Bay does not have a shallow sill separating the fjord waters from the outside ocean. However, it is clear from the hydrographic gradients between Andvord Bay and the Gerlache Strait that the waters inside the fjord are relatively isolated from those outside. On the other hand, the seasonal evolution of the fjord water masses mirror those of the region in general, and deep water oxygen levels never reach the low levels typical of silled fjords where the basin waters are entirely isolated (e.g. Anderson and Devol, 1987). We conclude that residence times in the fjord are long compared to the Gerlache Strait, but that the fjord waters, including those in the deep inner basins, are renewed on a seasonal time scale.

Our measurements do not allow us to directly determine the exchange flow. However, we can make some broad statements about which exchange mechanisms are likely to be dominant based on the fjord geometry and the typical magnitude of freshwater and wind forcing and of density fluctuations outside the fjord.

We find that mean wind and buoyancy forcing are both weak and unlikely to drive efficient exchange. Due to the relatively deep fjord sill, some exchange may be driven by sub-tidal fluctuations in the density field at the fjord mouth. This mechanism, which is alternately referred to as *baroclinic pumping*, *intermediary circulation*, or *geostrophic control*, has been shown to be a main driver of fjord-shelf exchange in many Arctic fjords (e.g. Cottier et al., 2005; Nilsen et al., 2008; Jackson et al., 2014; Sutherland et al., 2014b), where it is typically associated with changes in along-shelf wind forcing. In the case of Andvord Bay, we expect that the main source of density fluctuations is associated with the aforementioned subtidal variations in the geostrophically adjusted Gerlache Current. The magnitude of the exchange flow can be expected to be proportional to the *rate of change* of fluctuations in pycnocline depth (Arneborg et al., 2004). As such, the relatively long time scale (>20 days) of changes in the Gerlache Current would therefore seem to be a detriment to efficient exchange, but may still be a significant mechanism given the weakness of other processes.

While the steep topography isolates Andvord Bay from the mean along-shore winds, the fjord is occasionally exposed to strong, down-fjord wind events, likely associated with katabatic air flows from the glaciated plateau of the Antarctic Peninsula. The overall salinity increase in the fjord water during the December 2015 wind event is consistent with an export of the surface layer of the fjord. Katabatic wind events have been shown to have a great effect on the ocean in Arctic fjords (Spall et al., 2017). Several studies (Nilsen et al., 2008; Moffat, 2014; Spall et al., 2017) have also suggested that down-fjord winds can drive an import of external water masses in the deep fjord. As such, episodic local wind forcing events are also a possible renewal mechanism for the deep waters of Andvord Bay.

2.4.4 PHYSICAL CONTEXT FOR BIOLOGICAL PRODUCTIVITY

It has been hypothesized that Andvord Bay and other wAP fjords may be regional hotspots of biological productivity and biodiversity. Our results provide some insight in how the physical setting may set the stage for productive phytoplankton blooms in the fjord. First, low background wind stress in combination with the regional upper ocean freshening provides upper ocean conditions where phytoplankton are not mixed below the euphotic zone. Second, the weak current regime may allow blooms to develop fully within the fjord without being advected out. Whereas productivity in some glacial fjords is limited by turbid surface plumes as a result of subglacial discharge, the weak meltwater input in Andvord Bay results in good optical conditions for primary producers in the fjord. In sum, the quiet conditions and lack of wind-driven mixing likely allow fjords like Andvord Bay to be favourable environments for biological productivity compared to the shelf ocean. A clear exception to this occurs during katabatic wind events, which occur several times during the season. Future studies will focus on the effects of such events on the upper ocean and, by extension, marine organisms within it.

Strong episodic wind forcing events likely have a negative short-term effect on pelagic productivity as they act to flush out existing biomass, but may also drive a replenishment of nutrients in the euphotic zone, offering the system an opportunity to "reset" so that several blooms can occur within each growth season. Future atmospheric warming on the wAP is projected to increase surface runoff (Vaughan, 2006), which will likely increase the positive effects of upper stratification on phytoplankton productivity in Andvord Bay an the wAP coastal waters as a whole. However, increased glacial melt could also be disadvantageous to fjord ecosystems as it may increase upper ocean turbidity and benthic sedimentation rates, inhibit upward mixing of nutrients, and reduce the residence time of the upper fjord waters due to increased buoyancy-driven estuarine circulation.

2.5 CONCLUSIONS

We have presented a comprehensive observational study of the physical oceanography of a West Antarctic Peninsula fjord. Our findings evoke a picture of Andvord Bay as a dynamically quiet oceanographic environment, largely shielded from the strong along-shore currents and winds outside the fjord. The cold interior waters suggest that the majority of the fjord waters originate in the Bransfield Strait region, and we find little evidence of the presence of warmer uCDW water masses which are believed to drive glacial retreat further south along the Peninsula. Exchange between the fjord and the outside ocean is slow, but the fjord waters are ventilated on a seasonal time scale. We hypothesize that the main agents of this exchange are low-frequency fluctuations in the Gerlache Current and episodic down-fjord wind events, which occur several times each season.

Glaciers in Andvord Bay, like elsewhere on the wAP, are dynamic and fast-moving due to the high precipitation and steep topography. We find that the vast majority of the mass flux from the glaciers into the fjord occurs through the calving of icebergs, while runoff is small and turbid meltwater signature limited to weak mid-water plumes in the inner fjord. Future atmospheric warming on the wAP may change this, as a sustained milder climate may cause the glaciology of the wAP to become more similar to that of Greenland or the sub-Antarctic, where runoff and melt can be substantial. An increase in meltwater input could increase the estuarine circulation in the fjord, reducing the residence time of the fjord waters and increasing upper layer turbidity, both of which may have a negative impact on marine ecosystems within the fjord by reducing primary production and enhancing sedimentation disturbance. A more systematic comparison of Andvord Bay with sub-Antarctic fjords (where runoff can be much greater) and fjords further south on the wAP (where ocean-driven melt is believed to be important) might provide important insights into the impact of melt processes on fjord oceanography and ecosystems.

The West Antarctic Peninsula is a system in transition, and therefore an area of active oceanographic research. The present study provides a baseline for future research in Andvord Bay in particular, and fjord systems along the wAP more generally. Future publications from the FjordEco project will address the biology and geochemistry of the fjord, and study wind events, glacier-ocean interactions and biophysical interactions in Andvord Bay in more detail. Finally, we have shown that variations in currents and water masses flowing through the Gerlache Strait may be the main control on the oceanography of Andvord Bay. Future studies focusing on the regional circulation in the area are therefore necessary to understand the drivers of exchange and hydrography of wAP fjord systems, and their sensitivity to future atmospheric changes.

Chapter 3

Response of a fjord to down-axis wind events

Fjords along the western Antarctic Peninsula are episodically exposed to strong winds flowing down marine-terminating glaciers and out over the ocean. Given the weak background forcing and ocean circulation in these fjords, such winds could be an important mechanism for the ventilation of fjord waters. The effect of strong down-fjord wind forcing is examined through a series of numerical experiments based on a wind event observed in Andvord Bay in December, 2015. Passive tracers are used to identify water mass pathways and quantify exchange with the outer ocean. Upwelling and outflow in the model fjord generate an average salinity increase of ∼0.3 in the upper ocean during the event, similar to observations from Andvord Bay. The complex dynamical response of the fjord is strongly modified by rotation and includes the generation of near-inertial internal gravity waves. Down-fjord wind events are a highly efficient mechanism for flushing out the upper fjord waters, but have little impact on deep waters in the inner fjord. As such, episodic wind events likely have a large effect on fjord phytoplankton dynamics and export of glacially modified upper waters, but are an unlikely mechanism for the replenishment of deep basin waters and oceanic heat transport towards inner fjord glaciers.

3.1 INTRODUCTION

Due to their origin as submerged glacial valleys, most fjords are enclosed by steep topography which acts as a barrier for cross-fjord winds. As a result, local surface momentum transfer occurs predominantly in the along-fjord direction. High-latitude fjords often experience particularly strong down-fjord wind forcing during buoyancy-driven air flows known as *katabatic winds* (Argentini et al., 2003; Nielsen et al., 2014). The energetic surface forcing during katabatic events can elicit a strong response in fjord waters, including the export of sea ice (Johnson et al., 2011; Oltmanns et al., 2013) and upper ocean water masses (Svendsen et al., 2002), and upwelling and inflow of deep waters (Cottier et al., 2010; Spall et al., 2017).

Katabatic winds at high latitudes typically occur when cool and dense air masses from continental ice sheets descend along the topographic gradient and flow out over the ocean (Manins and Sawford, 1979; Renfrew, 2004). Katabatic winds have long been recognized as a characteristic feature of the surface wind field near Antarctica (Ball, 1957; Parish, 1988), and they play a particularly important role in the near-surface climate of the Antarctic Peninsula, where the complicated topography strongly influences the wind field (van Wessem et al., 2015, 2016). Nowacek et al. (2011) attributed the dominant, rotationally modified surface circulation observed in a large bay on the western Antarctic Peninsula (wAP) to a katabatic forcing episode, but otherwise little is known about how extreme down-fjord forcing events affect wAP fjords.

The ocean response to along-axis wind forcing in estuaries has been studied extensively (e.g. Hansen and Rattray, 1966; Svendsen and Thompson, 1978; Klinck et al., 1981). In narrow geometries, surface stress creates an along-wind transport in the top ocean layer, which is balanced by a deep inflow. Down-fjord winds can act to enhance the mean buoyancy-driven circulation and modify the stratification in shallow estuaries (Geyer, 1997; Chen and Sanford, 2009).

The dynamic response of a high-latitude, two-layer fjord to down-fjord katabatic wind events was explored by Spall et al. (2017). For broader fjords, the authors found that the main dynamical response is a balance between surface forcing and the horizontal pressure gradient. In such cases, the overall fjord response was found to be well represented by a non-linear, inviscid two-layer model (Farmer, 1976).

Rotational effects may be expected to play a role in the baroclinic dynamics of "dynamically broad" fjords where the first internal deformation radius L_1 is equal to or smaller than the fjord width. Arctic fjords typically fall within this category (Cottier et al., 2010), and it is likely also the case for many wAP fjords. Rotational deflection tends to concentrate surface outflow near the coast on one side of broad fjords (Svendsen, 1995; Ingvaldsen et al., 2001; Svendsen et al., 2002), and baroclinic instability of the resulting lateral shear can act to complicate the structure of the outflow (Carroll et al., 2017). In addition, diverging Ekman transport near the coast can generate a cross-fjord pattern of up- and downwelling which may result in an estuarine-like residual geostrophic circulation in the along-fjord direction (Cushman-Roisin et al., 1994).

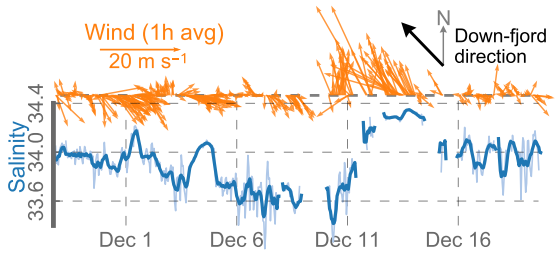

Figure 3.1: Wind and near-surface salinity measured by the R/V *L. M. Gould* within Andvord Bay in 2015. *Orange arrows*: Hourly averaged wind vectors (down-fjord direction is approximately towards the NW). *Blue lines*: Salinity measured by the underway flow-through system. Thick and thin lines show 6-hourly and hourly running averages, respectively.

It is usually assumed that down-axis wind pulses enhance the water exchange with the exterior ocean, reducing the upper layer residence time (Geyer, 1997) and increasing the inflow of oceanic deep waters (Moffat, 2014). Spall et al. (2017) estimated that katabatic wind events in Sermilik Fjord, Greenland could flush out 17-35% of the upper and 7-15% of the lower layer, respectively. Since relatively warm deep waters are often present outside glacio-marine fjords (Cottier et al., 2010; Straneo et al., 2012), deep inflow can drive heat transport towards temperature-sensitive tidewater glaciers (Rignot et al., 2010; Jenkins, 2011; Straneo et al., 2011; Cook et al., 2016). This can in turn generate glacier melt and retreat (e.g. Sutherland and Straneo, 2012; Inall et al., 2014). Several studies have suggested that local, along-fjord winds may drive import of warm deep waters in glacio-marine fjords (Nilsen et al., 2008; Moffat, 2014; Spall et al., 2017; Sundfjord et al., 2017), but the efficiency of this process is not well constrained and has not been documented in wAP fjords.

Fjords and bays along the wAP host productive marine pelagic ecosystems (Garibotti et al., 2003; Ducklow et al., 2007). Phytoplankton are concentrated in the euphotic zone, which is most directly impacted by surface forcing. A strong upper ocean response to wind forcing could conceivably impact the ecosystem both by advecting phytoplankton out of the fjord and by replenishing euphotic zone water masses with more nutrient-rich water through local upwelling or lateral exchange with the outer ocean.

As part of the NSF-funded *FjordEco* project, oceanographic observations were conducted in Andvord Bay, a glacial fjord on the northern wAP. In December 2015, sustained strong winds were observed blowing out the fjord over at least 3 consecutive days, reaching hourly averaged wind speeds of up to 25 m s^{-1} (Figure 3.1). The wind event coincided with a significant increase in the surface salinity of the near-surface fjord waters. Given the quiescent background conditions in the fjord (Domack and Williams, 1990), episodic wind forcing events could conceivably play a major role in the net fluxes between Andvord Bay and the exterior ocean.

This study explores the response of a high-latitude fjord to strong, episodic down-fjord wind stress forcing through a series of idealized numerical model experiments based on the wind event observed in Andvord Bay. Particular attention is given to changes in fjord water masses

and exchange with the exterior ocean, and how these processes depend on wind strength and duration, stratification and fjord geometry. We discuss the role of such wind events in ventilation of fjord waters, and in the oceanography of wAP fjords in general.

3.2 DATA AND NUMERICAL EXPERIMENTS

3.2.1 OBSERVATIONS

Measurements were collected in Andvord Bay between November 23 and December 22, 2015, during the *LMG15-10* cruise on the R/V *L. M. Gould*. Near-surface salinity was measured by a flow-through thermosalinograph with intake at 5-7 m depth, and winds were measured by an onboard meteorological sensor (Smith, 2017a). A total of 105 CTD profiles were collected within Andvord Bay proper during the cruise (Smith, 2017b). Ocean currents were measured by a 150 kHz Shipboard Acoustic Doppler Current Profiler (SADCP, available from the Joint Archive for SADCP website http://ilikai.soest.hawaii.edu/sadcp/).

3.2.2 NUMERICAL MODEL

We performed a series of idealized numerical experiments using the Regional Ocean Model System (ROMS), a free-surface, terrain following model commonly used in coastal studies (Shchepetkin and McWilliams, 2005). The experiments did not include ocean-ice interaction, thermal surface fluxes, freshwater or tidal forcing, all of which are processes likely to play a role in wAP fjords. The experiments are not intended as a full dynamical representation of a fjord like Andvord Bay, but rather represent a simplified system useful in understanding the response of fjords to strong wind events.

Idealized model experiments were conducted on a 40 km x 30 km f-plane model grid with 100 m uniform horizontal resolution and 30 s-levels in the vertical. Layer thickness varied from <1.5 m near the surface and 11 m at the bottom to a mid-depth maximum of 29 m.

The model was initialized with horizontally homogeneous vertical temperature and salinity profiles. The same profiles were applied as boundary conditions at the open model boundaries. All experiments were initialized at rest, with no flow prescribed at the boundaries. A sponge layer increased horizontal diffusivity and viscosity linearly by a factor of 10 over the outer 5 km towards the open boundaries.

Vertical mixing was parametrized using the conventional $k-\epsilon$ turbulence model (Launder and Spalding, 1983). Background vertical momentum viscosity and diffusivity were set to 10^{-6} m^2s^{-1}. We used the ROMS fourth-order scheme for tracer advection, and ROMSs third-order upstream advection scheme for momentum. Viscosity was parametrized using a small Laplacian coefficient scaled by the local deformation rate (Smagorinsky, 1963), using the conventional choice of 2.2

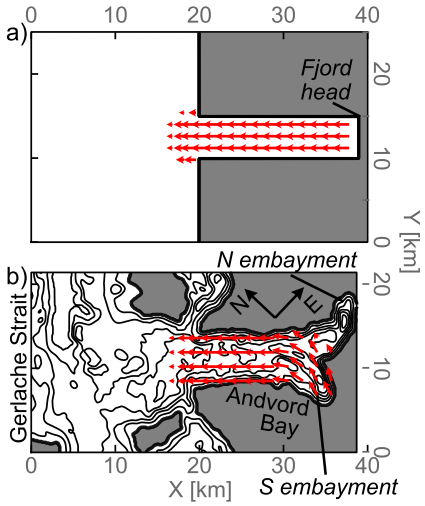

Figure 3.2: Schematics of model grid used in Main Scenario (*a*) and Andvord Bay runs (*b*). *a* has uniform depth 400 m, *b* shows 100 m depth contours. Red arrows show the spatial envelope used for the wind stress forcing. Black compass arrows in *b* show the true geographical coordinates in Andvord Bay. Also shown are various labels referenced in the text. Edges with no coastline are open model boundaries.

for Smagorinsky coefficient c_s (e.g. Griffies and Hallberg, 2000). Explicit background horizontal diffusivity was set to 2 $m^2\ s^{-2}$ for all tracers.

3.2.3 EXPERIMENTS

3.2.3.1 *Main scenario*

The main experiment discussed in this study (hf. *Main Scenario* experiment) was designed to simulate the wind event observed in Andvord Bay in December 2015. The bathymetry in this experiment was that of a highly idealized fjord inset in a coastline running along the north-south direction (Figure 3.2a). The width and length of the fjord were 5 km and 19 km respectively, and ocean depth was set to 400 m throughout the entire domain including the ocean outside the fjord. The Coriolis parameter f was set to -1.81 cpd, corresponding to 64.75°S latitude.

Initial and boundary temperature and salinity conditions were prescribed based on smoothed average profiles from 17 CTD casts taken in Andvord Bay between November 5th and Dec 9th 2015, as part of the *FjordEco* program. To avoid spurious values in the deep ocean due to varying CTD depth ranges, temperature was set to a fixed value (-0.915 °C) everywhere below 300 m. Salinity was set to increase at a fixed rate of 2.5×10^{-5} m^{-1} below 300 m, giving a weak but stable stratification consistent with the observations from Andvord Bay. With this setup, the first baroclinic deformation radius was calculated to be 2.9 km.

Water masses in the model were tagged using passive numerical dyes in order to trace the pathways of water masses during the model run. All water outside the fjord ($x < 20$ km) was

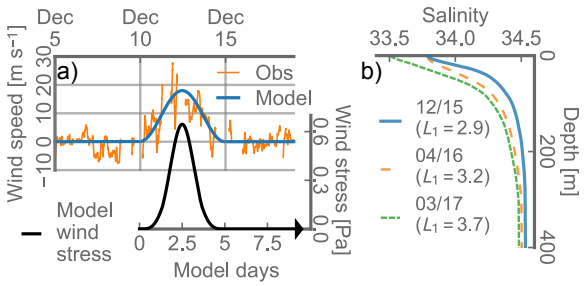

Figure 3.3: *a: Orange line:* Hourly averaged wind (positive down-fjord) from shipboard measurements within Andvord Bay in 2015. *Blue line:* Model down-fjord wind speed. *Black line:* Model down-fjord wind stress. *b:* Salinity profiles prescribed as model initial and boundary conditions. The blue line shows the average profile from Andvord Bay before the wind event in December 2015, used in the Main Scenario and most variational runs. Dashed orange and green lines show average profiles from subsequent cruises in fall and late summer, respectively. The first baroclinic deformation radius L_1 associated with each profile (in km) is shown in the legend.

initialized with an *Ocean Water (OW)* tracer used to study the evolving distribution of ocean water in the fjord. In order to examine the exchange of the near-surface water masses where phytoplankton are concentrated, we introduced a second *Upper Fjord Water (UFW)* tracer within the fjord ($x > 20$ km). The UFW was initialized in the upper 35 m, a typical extent of the euphotic zone on the coastal wAP during moderate bloom conditions (Vernet et al., 2008).

The idealized model wind time series was prescribed a sinusoidal bell function between the model start time t_0 and a later time t_1, and set to zero beyond. Surface wind stress $\vec{\tau}_{wind}$ was computed from the model wind time series $\vec{U}$ using the conventional bulk formula (e.g. Gill, 1982), where $\vec{\tau}_{wind}$ is proportional to $|\vec{U}|^2$ below 10 m s^{-1} and to $|\vec{U}|^3$ above (Large and Pond, 1981).

Model winds were scaled to approximately match the observed event, with maximum wind speed 18 m s^{-1} and corresponding maximum wind stress amplitude 0.645 Pa (shown in Figure 3.3a). While the entire wind event was approximated with a 5-day sinusoidal envelope ($t_1 = 5$ days), 98% of the integrated wind stress was applied within a 3-day window, 56% within a single day.

The wind stress forcing was applied uniformly over the surface area of the fjord (Figure 3.2a). Outside of the fjord, the forcing amplitude was set to decay linearly over 5 km westward, with a 1 km decay in the y-direction on each side in order to avoid extreme surface stress gradients.

3.2.3.2 *Other experiments*

While the Main Scenario experiment was designed to resemble the wind event observed in Andvord Bay in December, 2015, the ocean response during wind events more generally may be expected to vary as a function of forcing, stratification and fjord geometry. To more fully understand the effects the winds, we explored the changes in ocean response and water mass exchange under variations of key parameters of the idealized model (summarized in Table 3.1). Unless ex-

plicitly stated, the configuration of these additional experiments was otherwise identical to that of the Main Scenario.

The strength and duration of the surface forcing were varied by scaling and stretching the bell-shaped wind function (*Forcing Amplitude* and *Forcing Duration* experiments). Changes in wind speed are further exaggerated in wind stress due to the non-linearity of the bulk formula; the time period containing 95% of the integrated wind stress is listed alongside the forcing duration ($t_1 - t_0$) in Table 3.1. Sensitivity to the choice of horizontal viscosity and vertical mixing parameters was tested (*Mixing and viscosity* experiments), and we conducted experiments without forcing, with f set to zero, and with wind stress applied across the entire spatial domain (*Limit Case* experiments).

Sensitivity to stratification was explored by varying the prescribed vertical profiles (*Stratification* experiments). We used average profiles from subsequent *FjordEco* cruises to Andvord Bay in April, 2016 and March, 2017 (Figure 3.3b) in order to represent the annual range of stratification in the fjord. An experiment was also performed using the idealized two-layer profile from Spall et al. (2017), with an upper layer of salinity 31 transitioning to a lower layer with salinity 32.5 around 150 m depth.

The fjord width was varied between 1 and 9 km, thus spanning the range from "dynamically narrow" to "dynamically broad" fjords (*Width* experiments). Finally, we performed a simulation with a model of the Andvord Bay bathymetry and coastline as a comparison to the idealized cases (*Andvord Bay* experiment). The model grid was rotated to align the main axis of the fjord with the x-direction (Figure 3.2b), and the geographic labels used here (e.g. "northern coast") correspond to the rotated grid. Horizontal resolution, number of vertical layers, wind forcing function and initial and boundary conditions were identical to in the Main Scenario. The spatial envelope of the wind forcing was modified to resemble the wind pattern typically observed in Andvord Bay, with winds emanating from the southern embayment. We also performed an experiment on the Andvord Bay grid where the bell-shaped forcing function was replaced with a 1 Pa impulse function applied over 2 hours (*Transient* experiment).

3.3 RESULTS

3.3.1 DYNAMICAL RESPONSE TO DOWN-FJORD WIND EVENTS

3.3.1.1 *Near-surface currents*

We first consider the response of the near-surface layer, taken as the upper 35 m of the water column. The surface forcing rapidly spins up an energetic response in this layer, shown in Figure 3.4. During peak forcing, strong Ekman deflection of the wind-driven currents concentrates the outflow in a band along the southern edge of the fjord. At its strongest, westward surface velocity

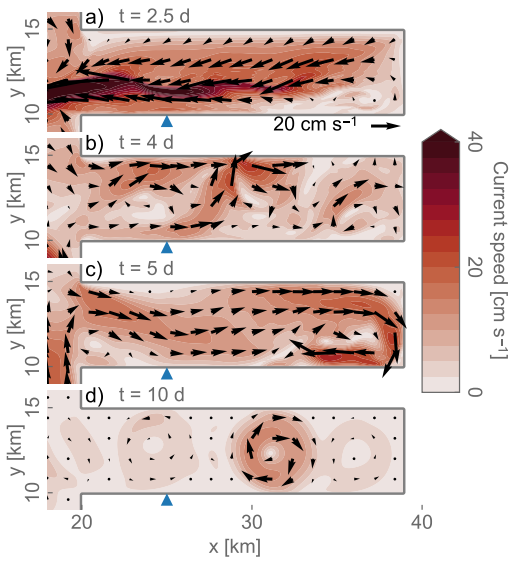

Figure 3.4: Snapshots of currents averaged over the upper 35 m at successive times of the Main Scenario experiment. Blue markers show $x = 25$ km.

within this band at the fjord mouth exceeds 80 cm s^{-1}. Outside the fjord, the flow continues to be deflected towards the southern boundary of the model domain.

The increasing winds set up and maintain strong pressure gradients, with sea surface depressions to the east and north. These gradients persist as the wind forcing subsides, and drive a surface return flow into the fjord which appears around $t = 4$ days, concentrated along the northern coast (Figure 3.4b). The spatial structure of the currents also becomes increasingly complex in this phase. In particular, three bands of flow towards the northeast appear in the middle of the fjord, separated by a zonal distance of 5-8 km. The pattern resembles that of three cyclonic vortices, each with a radius similar to the width of the fjord.

This complex flow pattern largely eliminates the cross-fjord pressure gradient. However, a sea surface depression of $\sim$1.9 cm still exists in the inner fjord at $t = 4$ days. The along-fjord pressure gradient is equalized as the near-surface inflow propagates into and clockwise around the fjord, consistent with the behaviour of a baroclinic Kelvin wave (Figure 3.4c). The propagation speed of the signal along the fjord walls is approximately 22 cm s^{-1}, similar to the gravity wave speed of the second baroclinic mode (19 cm s^{-1}). After the passage of the wave, the near-surface horizontal pressure gradient is greatly diminished, and the surface flow in the fjord subsides, with the notable exception of a geostrophically balanced cyclonic eddy present in the middle of the fjord (Figure 3.4d).

To explore the dynamics in greater detail, we examine the time-varying terms of the zonal momentum equation, equivalent to:

$$\underbrace{\frac{\partial u}{\partial t}}_{\text{acceleration}} = \underbrace{-u\frac{\partial u}{\partial x} - v\frac{\partial u}{\partial y}}_{\text{hor. advection}} \underbrace{-w\frac{\partial u}{\partial z}}_{\text{vert. advection}} \\ \underbrace{+fv}_{\text{Coriolis}} \underbrace{-\rho^{-1}\frac{\partial p}{\partial x}}_{\text{pressure gradient}} \underbrace{+F_D}_{\text{vert. visc.}} \underbrace{+F_H}_{\text{hor. visc.}} \tag{3.1}$$

where u, v, w are the Cartesian velocity components, ρ density and p pressure. The two rightmost terms represent vertical and horizontal eddy viscosity.

The first-order dynamic balance in the near-surface fjord is between surface forcing (transferred down into the water column through vertical eddy viscosity) and the zonal pressure gradient resulting from the sea surface depression inside the fjord (Figure 3.5a). The sum of these two terms is directed out of the fjord during peak forcing, but changes sign around day 3, as the forcing subsides while the pressure gradient remains. However, the dynamics are more complex than this simple balance, and both Coriolis and advective terms are of significant magnitude (Figure 3.5d, g). These secondary terms counteract the dominant balance, thus acting to limit the acceleration of the water. Horizontal friction plays a negligible role in the laterally integrated response of the fjord.

The cross-fjord momentum balance is entirely dominated by the geostrophic terms, which track closely at all depths throughout the event (Figure S1, supplemental material). The evolution of the cross-fjord pressure gradient mirrors that of the along-fjord currents with an initial two-layer vertical structure transitioning into a three-layer one.

3.3.1.2 *Vertical structure*

The flow has a two-layer structure during the active forcing phase (Figure 3.6a). An outflow concentrated above 70 m depth (3.7×10^4 m^3 s^{-1} at $x = 25$ km, $t = 2.5$ days) is nearly balanced by a deep inflow below, with a small (8.0 m^3 s^{-1}) net volume flux out of the fjord. The upper layer outflow is strongly surface-intensified, while the deep inflow is distributed throughout the deep waters, with a cross-fjord average maximum at ~95 m depth. As the wind forcing weakens, a distinctly different vertical pattern emerges. One day after peak forcing, flow below 200 m has reversed and is directed outward. In addition, a mean inflow of up to 7 cm s^{-1} develops between 50 and 100 m at this time.

As the forcing subsides entirely, the vertical structure changes once again. By $t = 5$ days, the along-fjord currents are stacked in three layers, with outflow between 50-200 m and inflow above and below. After $t = 9$ days, the layered structure has largely dissipated, and the currents are instead dominated by a weak ringing at a frequency of approximately 2 cpd.

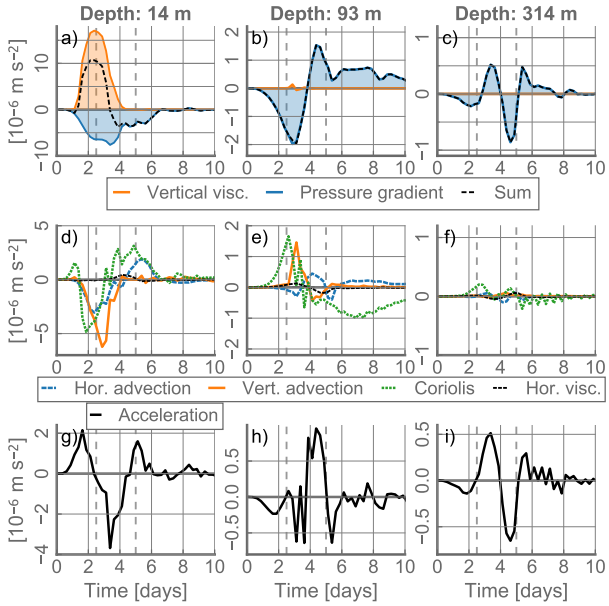

Figure 3.5: Terms of the along-fjord momentum equation (3.1) in the Main Scenario experiment as a function of time at select depths. All terms are defined as positive out of the fjord. Each term has been integrated horizontally across the fjord and between $x = 25$ km and $x = 35$ km. Upper panels (*a-c*) show vertical friction (orange), pressure gradient (blue) and the sum of the two (black). Middle panels (*d-f*) show the remaining terms. Lower panels (*g-i*) show acceleration. The peak and the end of the surface forcing (t = 2.5 and 5 days respectively) are indicated in dashed vertical lines.

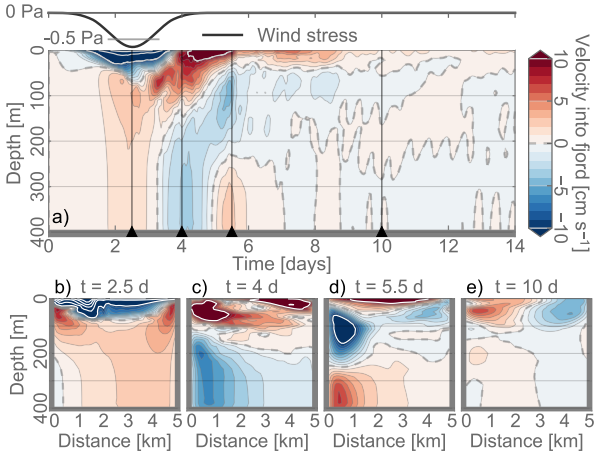

Figure 3.6: Along-fjord velocity in the Main Scenario experiment (negative/blue out of the fjord). *a)* Along-fjord currents averaged across the fjord at $x = 25$ km as a function of depth and time. Wind stress shown on top. *b)* Cross-sections at $x = 25$ km at successive times of the model run. The view is out of the fjord, with x-axis distance increasing towards the north. The color scale is saturated at ± 10 cm s^{-1}; velocities beyond this range are indicated by white contour lines spaced by 10 cm s^{-1}.

Near 100 m depth, direct stress forcing has little impact (Figure 3.5b). Instead, the pressure gradient resulting from the sea surface displacement is the dominant forcing term. Counteracted by a combination of the Coriolis and vertical advection terms, the pressure gradient drives the weak inflow during the active forcing (3.5e, h). Near $t = 4$ days the pressure gradient changes sign, and a strong outward acceleration occurs before the terms settle into geostrophic balance approximately one day later.

Below 300 m, the dominant momentum balance is between the pressure gradient and the zonal acceleration, with the Coriolis term playing a secondary role (3.5c, f, i). As the overlying gradients in density and sea surface evolve, the pressure gradient changes sign several times, accounting for the flow reversal in the bottom layer and resulting three-layer structure.

3.3.1.3 *Cross-fjord structure and upwelling*

The velocity structure is not uniform across the fjord, as shown in cross-fjord transects of along-fjord velocity during various phases of the response (Figure 3.6b-e). During peak forcing, the surface outflow is intensified in the southern half of the fjord, while the deep inflow is stronger towards the north, consistent with rotational deflection to the left of the flow direction. In addition, an inflowing subsurface jet (up to 10 cm s^{-1}) is present near the southern coast near 50 m depth.

As the forcing relaxes, the evolving deep outflow is concentrated along the southern edge, where it extends from 100 m depth to the bottom (Figure 3.6c). By $t = 5$ days, the surface inflow has become restricted to the upper 50 m, and the mid-water outflow and bottom inflow are both strongly intensified towards the southern coast. By $t = 10$ days, the response has died down with the exception of the residual geostrophic eddy, which extends down to $\sim$100 m.

In the active forcing phase, the fjord displays a distinct pattern of downwelling along the southern coast, and upwelling to the north and in the inner fjord. Surface salinity increases by as much as 0.6 near the northern coast and the head of the fjord during peak forcing as isohalines originally located at 60-80 m depth outcrop at the surface (Figure 3.7a). In the relaxation phase, the cross-fjord surface density gradients are quickly equalized (Figure 3.7b), followed by downwelling and inflow throughout the fjord which returns the upper ocean to near its initial state.

3.3.2 IMPACT ON FJORD WATERS

The bulk of the water masses initially occupying the upper 35 m (UFW) is quickly exported out of the fjord along the southern coast and into the exterior ocean. By the time of maximum forcing ($t = 2.5$ days), 70% of the UFW has exited the fjord, and 5 days later this has further increased to 80%. Of the UFW that does remain in the fjord, only 54% is located above 35 m, suggesting that much of the near-surface water gets mixed downward in the course of the event. Most of the

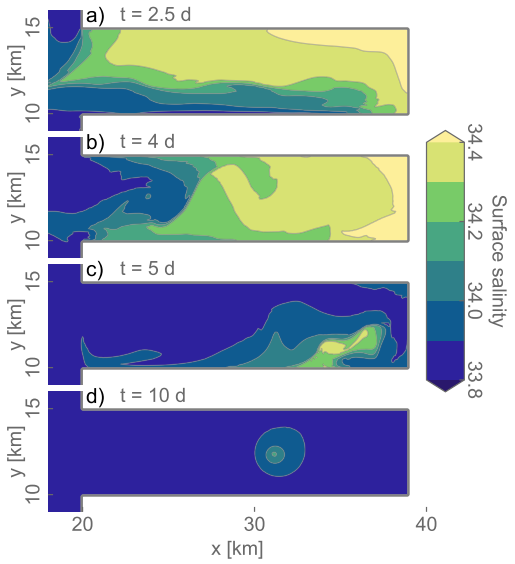

Figure 3.7: Snapshots of surface layer salinity at successive times of the Main Scenario experiment.

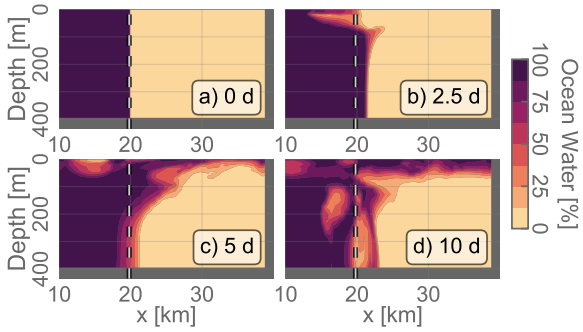

Figure 3.8: Cross-fjord averaged fraction Ocean Water (OW) at successive times of the Main Scenario experiment. Location of the fjord entrance indicated in dashed line.

exported UFW becomes entrained in circulation outside the fjord and exits through the model boundaries in the southwestern quadrant of the model domain.

The exported UFW is almost entirely replaced by water masses from the outside ocean (OW, Figure 3.8). OW begins to enter the upper waters of the fjord as the surface circulation reverses, and most of the import occurs rapidly around $t = 4$ days, when the inflow is at its strongest. By $t = 10$ days, 75% of the fjord waters above 50 m consist of OW.

Between 50 and 150 m depth, the OW fraction at $t = 10$ days is reduced to 20%. The majority of the exchange in this depth range is restricted to the area around the fjord entrance (dashed line in Figure 3.8); in the inner 14 km of the fjord ($x > 25$ km), the water between 50 and 150 m consists of only 9% OW.

Almost no exchange with the external ocean occurs in the deep waters of the inner fjord. The weak, deep inflow during the active forcing stage brings external water into the outer reaches of the fjord, shown as an eastward displacement of the OW gradient from its initial location at the

mouth (Figure 3.8b). As the deep flow subsequently reverses, the gradient moves back towards the west (Figure 3.8c). Only 7% of the fjord water below 150 m is replaced by OW by $t = 10$ days, and the import is restricted to the outer few kilometers.

In total, 7.1 km^3, or 18% of the total fjord water volume, is exchanged by $t = 10$ days (7.5 days after peak forcing). Of the imported OW, 3.2 km^3 makes it more than 5 km into the fjord, corresponding to 11% of the fjord volume in the inner 14 km. Roughly half (3.6 km^3) of the total exchange occurs in the upper 50 m, where OW is found throughout the length of the fjord by $t = 10$ days.

3.3.3 DEPENDENCE ON FORCING, GEOMETRY AND OTHER PARAMETERS

The overall characteristics of the oceanic response are conserved throughout the range of variational experiments. Changes in the ocean response and water mass exchange in the various idealized cases are summarized in Table 3.1, and briefly discussed in this section.

3.3.3.1 *Forcing duration and amplitude*

Increasing the maximum wind speed to 22 m s^{-1} increases the amount of UFW exported from the fjord at $t = 10$ days to 93% of the initial volume, compared to 81% in the Main Scenario (maximum wind speed 18 m s^{-1}). The deep waters of the inner fjord remain relatively unaffected by OW. Export and exchange are similarly reduced when the wind stress amplitude is decreased. However, even at a maximum wind speed of 10 m s^{-1} (a reduction in maximum wind stress by nearly 80% from the Main Scenario), 35% of the UFW is exported from the fjord.

Lengthening the duration of the applied wind stress forcing increases the upper layer flushing, although the efficiency saturates or even decreases slightly beyond a forcing envelope of 7 days (which corresponds to applying 95% of the wind stress within 3.6 days). A shorter forcing duration decreases the flushing efficiency, but even after a drastic reduction, the wind forcing has a significant effect on the surface layer. When the envelope window is shortened to one day (thus applying 95% of the wind stress within 12 hours), the forcing still causes more than 35% of the UFW to be flushed out of the fjord.

Net exchange below 150 m depth remains similar when the duration of the forcing is extended. However, at the longest duration (9 days envelope, 95% wind stress within 4.6 days), there is a significant increase in the OW penetrating beyond 5 km into the fjord, to 1.5% from 0.1% in the Main Scenario. However, this inflow does not extend into the innermost 10 km, where the OW fraction below 150 m is negligible.

In the case where surface forcing is applied throughout the entire ocean domain, the exported UFW fraction at $t = 10$ days increases to 89% from 81% in the Main Scenario. This is also the experiment with the greatest import of OW below 150 m (34%, versus 7% in the Main Scenario), and the only case in which OW penetrates into the deep waters near the head of the fjord. The deep inflow occurs along the northern coast and in the later stages of the experiment, after the

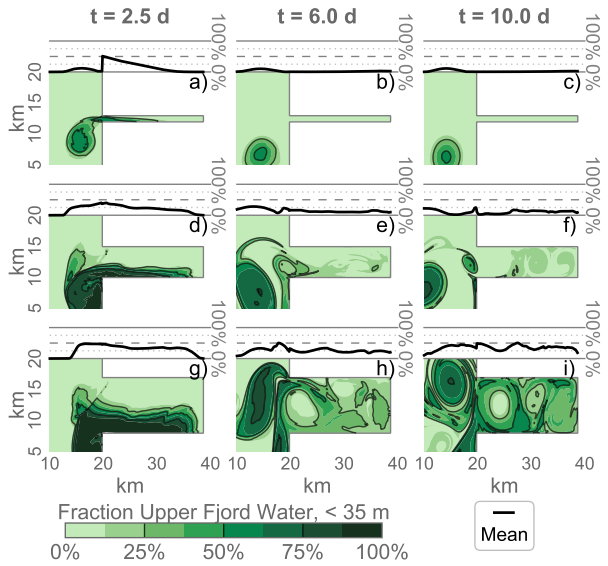

Figure 3.9: Distribution of UFW above 35 m in the Width experiments as a function of time for fjord widths 1 km (*a-d*), 5 km (*e-f*), and 9 km (*i-l*). The black line on top of each figure shows the average in the y-direction. This metric does not include UFW which has been mixed or advected below 35 m but remains within the fjord.

main fjord response has died down. The inflow is associated with a southward deep current, which develops along the outside coast and is partially deflected into the fjord. This deep coastal current is absent in the other experiments, and is likely a result of adjustment to forcing applied in the outer ocean.

3.3.3.2 *Rotation and geometry*

In the case where f is set to zero, the maximum value of the cross-fjord averaged flow speed increases significantly (47 cm s^{-1}, relative to 37 cm s^{-1} in the Main Scenario). The exported UFW fraction after the event increases to 97% (from 81%). The overall import of external water also increases without rotation, although OW does not penetrate into the deep waters of the inner fjord. The effects of rotation are also evident in experiments varying the fjord width, and thereby the ratio between horizontal scale and deformation radius (Figure 3.9). The flushing (fractionally) of UFW decreases as the fjord becomes wider, from 94% exported UFW in the 1 km width case to 52% in the 9 km case. In the wider cases, more UFW remains along the southern edge as the outflow subsides. This water is advected back into the inner fjord and/or entrained in the rotational circulation cells that develop in the upper ocean after the wind event. Conversely, in the 1 km wide fjord, the great majority of UFW is immediately exported during the active forcing phase.

Inflow of deep water extends further into the fjord when the width is increased, and 5% OW is found in the inner 14 km below 150 m depth at $t = 10$ days for the 9 km width case. However, the OW fraction is still near zero in the inner 10 km of the fjord.

Table 3.1: Overview of idealized experiments and relevant diagnostic parameters.

		$\mathbf{u_{max}}$ [A] $[cm\ s^{-1}]$		$\Delta\eta_{max}$ [B] $[cm]$		UFW [C] [%]	OW, 0-400 m [D] [%]		OW, 0-50 m [%]		OW, 50-150 m [%]		OW, 150-400 m [%]	
Experiment	**Parameters**	Out	In	Along	Cross	Fraction	> 20 km	> 25 km	> 20 km	> 25 km	> 20 km	> 25 km	> 20 km	> 25 km
Main Scenario	L_1 =2.7 km	-37.2	14.9	-2.0	-1.7	19.1	18.7	11.3	75.3	72.2	19.5	9.3	7.3	0.1
Width	1 km	-44.8	19.1	-2.0	-0.5	5.8	21.9	12.2	84.9	82.2	13.9	7.8	12.7	0.1
	3 km	-42.1	21.0	-2.0	-1.1	7.8	20.0	14.0	87.1	85.4	17.1	13.5	8.0	0.1
	7 km	-35.5	12.3	-2.0	-2.0	36.2	21.1	9.4	54.2	50.8	24.3	11.3	13.5	0.5
	9 km	-32.6	11.3	-2.1	-2.2	48.4	21.3	12.1	43.0	42.2	27.3	16.6	14.8	4.5
Stratification	Andvord Bay, 04/16 (3.2 km)	-36.5	11.6	-2.2	-1.5	24.7	19.7	11.0	72.7	68.0	23.8	9.7	7.8	0.3
(Rossby radius L_1)	Andvord Bay, 03/17 (3.7 km)	-36.9	12.7	-2.8	-1.7	22.4	19.9	12.7	74.0	70.5	26.1	15.3	6.8	0.2
	Greenland, (8.4 km)	-23.6	3.8	-1.0	-0.2	77.3	10.3	2.0	20.7	6.6	18.4	4.8	5.1	0.1
Forcing amplitude	10 m s^{-1} / 0.14 Pa	-15.8	8.3	-1.1	-0.8	63.5	6.9	2.5	30.3	19.5	9.4	0.5	1.3	0.0
(Maximum)	14 m s^{-1} / 0.33 Pa	-27.7	9.5	-1.6	-1.3	32.8	13.3	6.5	50.9	43.8	18.3	4.2	3.9	0.0
	22 m s^{-1}/ 1.12 Pa	-48.3	24.2	-2.3	-1.9	6.6	26.7	18.7	92.0	91.1	36.0	28.1	10.2	0.9
Forcing duration	1 day / 0.5 days	-41.1	9.7	-1.5	-1.8	63.5	7.4	2.4	28.4	18.1	9.3	0.6	2.5	0.0
($t_1 - t_0$ / 95% w.s.)	3 days / 1.5 days	-40.6	16.4	-1.9	-1.8	30.4	13.1	7.5	57.0	51.5	13.2	4.6	4.5	0.0
	7 days / 3.6 days	-40.1	14.7	-2.1	-1.5	10.7	22.5	14.3	83.0	79.7	24.6	15.4	9.9	1.0
	9 days / 4.6 days	-38.4	14.8	-2.0	-1.4	12.8	24.3	16.9	87.8	85.1	32.1	21.9	8.8	1.5
Mixing	ν_H = 10 m^2 s^{-1}	-38.7	14.3	-2.0	-1.7	29.5	13.0	9.8	62.0	59.4	12.0	9.5	3.7	0.1
and viscosity	$c_S = 4$	-37.5	14.3	-2.0	-1.7	20.2	18.2	11.9	76.7	72.1	19.9	12.0	6.1	0.1
	A_V =10^{-5} m^2 s^{-1}	-37.2	15.0	-2.0	-1.7	19.2	18.4	11.3	75.3	72.6	18.9	9.1	7.1	0.1
Limit Case	Zero forcing	0.0	0.0	0.0	0.0	100.0	0.0	0.0	0.0	0.0	0.0	0.0	0.0	0.0
	f = 0	-47.1	27.7	-1.9	-0.0	3.1	26.3	16.7	77.2	72.7	20.7	12.1	18.6	7.1
	Full domain wind	-40.3	26.0	-1.6	-1.8	10.8	31.1	21.0	31.8	30.3	24.4	12.4	33.9	22.6

[A] Max/min cross-fjord averaged along-fjord velocity at x = 25 km.

[B] Max difference in sea surface anomaly η. *Along*: Cross-fjord averaged $\Delta\eta$ from entrance ($x = 20$ km) to head ($x = 39$ km). *Cross*: $\Delta\eta$ from S to N coast averaged between $x = 20$ km and $x = 35$ km.

[C] Fraction *UFW* retained in the fjord 5 days after the cessation of the event ($t = 10$ days all except varying forcing duration runs).

[D] Fraction *OW* within a given depth range 5 days after the cessation of the event. Showing fraction inward ofthe fjord mouth (x > 20 km) and the inner 14 km of the fjord (x > 25 km).

3.3.3.3 *Stratification*

The model response is relatively insensitive to changes in initial stratification within the range of the *FjordEco* observations. A slight decrease in UFW flushing efficiency is observed from the Main Scenario (spring, 81% export) to the cases with higher stratification (late summer and fall, 75% and 77%, respectively).

While fjords and estuaries are often modelled as two-layer systems, the observed stratification in Andvord Bay is continuous and extends to the surface. Replacing the Andvord Bay stratification with the two-layer profile used by Spall et al. (2017) significantly changes the exchange flow in the model. The import of OW is reduced by a factor of 1.8, largely due to decreased exchange in the upper layer. The UFW flushing is also greatly diminished; the fraction exported from the fjord at $t = 10$ days decreases from 81% to 23%. While the bulk of UFW is advected out of the fjord during the active forcing in the Main Scenario, it is here rapidly mixed vertically throughout the unstratified upper layer, down to the layer interface near 150 m depth. Along-fjord flow speeds are also significantly reduced in the two-layer case.

3.3.3.4 *Viscosity and vertical mixing*

Model results are practically unchanged when the background vertical mixing coefficient A_V is increased by an order of magnitude compared to the Main Scenario. The same is true for a moderate increase in horizontal viscosity (increasing the Smagorinsky parameter c_s from 2.2 to 4). In contrast, applying a high, fixed Laplacian viscosity ($\nu_H = 10$ m^2 s^{-1}) changes the character of the dynamical response significantly. In particular, the small-scale flow features around $t = 4$ days are largely suppressed, and tracer and velocity distributions become smoother. The net result is a reduction in UFW flushing efficiency (70% UFW exported) and the overall exchange with the exterior ocean (13% OW in the fjord at $t = 10$ days versus 19% in the Main Scenario).

3.3.4 ANDVORD BAY EXPERIMENT AND COMPARISON WITH OBSERVATIONS

3.3.4.1 *Andvord Bay experiment*

The experiment using realistic bathymetry for Andvord Bay shares the main characteristics of the idealized experiments. An outflow develops during active forcing, with average currents of 30-40 cm s^{-1} in the upper 35 m in a band along the southern coast of the outer fjord (Figure 3.10). The strong outflow flushes the bulk of UFW into the outside strait as well as into the small inlet south of the fjord. The outflow is followed by a reversal of the surface flow, concentrated along the northern side and extending into the inner fjord. Although strong cross-fjord gradients are present during the active forcing phase, there is no development of evenly spaced fjord-scale vortices as in the idealized Main Scenario, likely due to the effects of variable topography and bottom-slope drag.

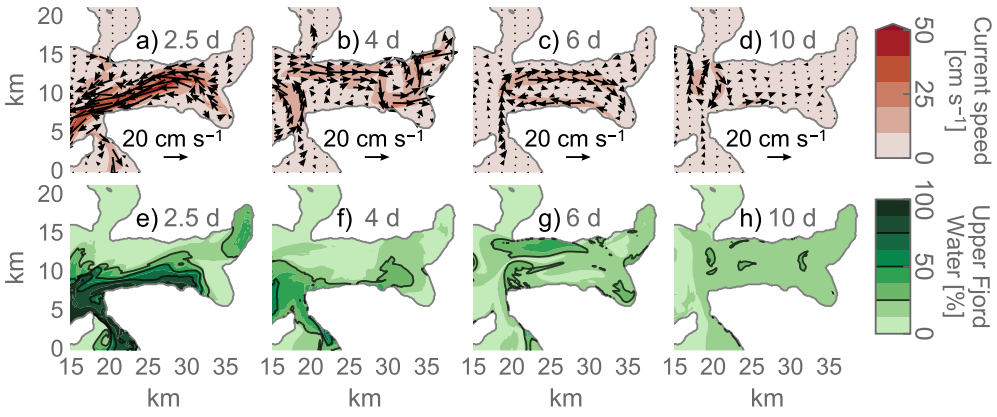

Figure 3.10: Horizontal currents (*a-d*) and percentage original upper fjord water (*e-f*) averaged over the upper 35 m at successive times of the Andvord Bay experiment.

After the main response, a coastal Kelvin wave propagates along the northern coast and into the northern embayment, where it largely dissipates. At $t = 6$ days, a clockwise circulation pattern dominates the surface currents in the main body of the fjord. Some residual flow remains during the later stages of the experiment. In particular, a cyclonic eddy is situated in the outer part of the fjord, and two smaller circulation cells are present further inside, but these largely dissipate by $t = 10$ days.

Although the majority of the upper layer is flushed out, a smaller fraction of UFW (68%) is exported from the fjord compared to the idealized Main Scenario experiment (81%). This is likely a result of the geometry of the coastline outside the fjord. Whereas there is an open path to the southwest in the idealized case, the coastline partially blocks this outflow in the Andvord Bay experiment. As a result, much of the exported water remains directly outside the fjord, and is re-imported along the northern edge as the surface flow reverses.

The overall amount of external water entering the fjord is larger than in the idealized case (32% OW at $t = 10$ days). A significantly larger amount of the water exchange occurs below 150 m (26% OW below 150 m in the Andvord case, 7% in the Main Scenario). This inflow only occurs in the outer region of the fjord, while the inner reaches including the inner basins remain largely unaffected by water from the external ocean (0.5 % OW below 150 m depth inward of $x = 30$ km).

3.3.4.2 *Observed water mass changes*

Successive CTD profiles before and after the December, 2015 event show a distinct increase in salinity above 100 m (Figure 3.11). This increase is not balanced by a decrease at depth, indicating an exchange of water masses rather than a vertical redistribution due to wind-driven mixing. The salinity increase is greatest at the surface, but it is apparent down to 80 m depth in all profiles.

Surface salinity in CTD measurements after the wind event is 34.0 or greater, an increase of 0.3-0.4 compared to before the event. During the active forcing, near-surface salinity measured

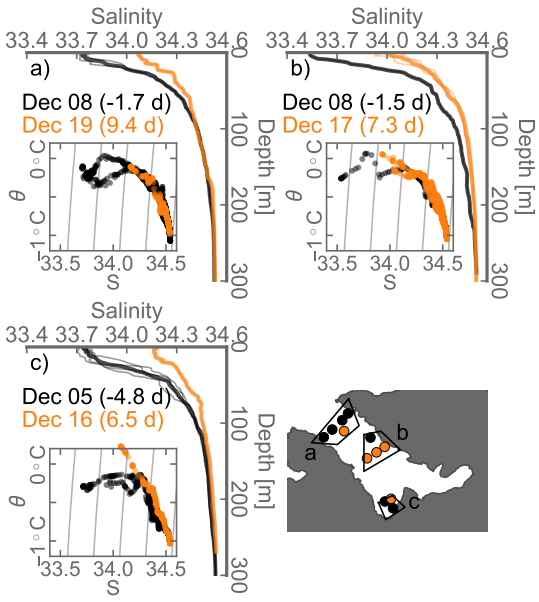

Figure 3.11: Main axes of *a*, *b* and *c*: Salinity profiles from CTD measurements before (*black*) and after (*orange*) the wind event on December 11th-14th, 2015 taken in adjacent locations within Andvord Bay (shown on bottom right). Smaller, inset figures show potential temperature θ from the same profiles as a function of salinity. Density contours are overlaid with increments of 0.2 kg m^{-3}.

by the shipboard flow-through system (Figure 3.1) reaches 34.3, before decreasing as the wind subsides. The pattern is consistent with upwelling in the fjord during the event, and subsequent downwelling as the pressure gradients cease to be balanced by surface wind stress. The process does not seem to be entirely reversible, and salinity remains elevated after the event.

An interesting feature observed in CTD profiles from the northern embayment is the increase in surface layer temperature θ after the wind event ($\theta - S$ diagram in Figure 3.11c), where near-surface waters warm up by approximately 0.5 degrees to +0.25°C. In general, there is a weak upper ocean cooling towards the head of Andvord Bay, and the warm anomaly may be an indication of net heat transport towards the inner fjord during the wind event. It could also be a reflection of general horizontal patchiness of temperature in the area.

The Andvord Bay model experiment reproduces the rapid salinity increase observed in the upper ocean during the active forcing (Figure 3.12). However, model upper layer salinity reverts back to significantly lower values after the event than in the observations. While average salinity in the upper 35 m of the model fjord is below 34.1 after the event, corresponding values calculated from individual CTD profiles are all around 34.2.

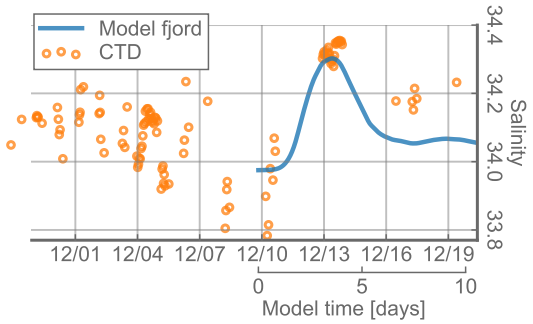

Figure 3.12: Average salinity in the upper 35 m of the water column. *Blue line*: Average salinity in the Andvord Bay model experiment. *Orange circles*: CTD casts within Andvord Bay in December, 2015.

3.4 DISCUSSION AND CONCLUSIONS

3.4.1 DYNAMICS

The model experiments show that in relatively broad fjords, strong episodic down-fjord wind forcing initially generates a two-layer exchange flow, where a vigorous surface outflow in the directly wind-forced layer overlies a weak inflow below. This initial flow structure is qualitatively consistent with classical models for surface-forced, non-rotating estuaries (Hansen and Rattray, 1966; Farmer and Osborn, 1976; Geyer, 1997), and with the two-layer dynamical structure often assumed for fjords (Svendsen and Thompson, 1978; Klinck et al., 1981; Spall et al., 2017).

In the relaxation phase, the flow reverses as a result of the strong pressure gradients present in the fjord as the forcing subsides. The flow also becomes more complex, with the overall velocity structure eventually transitioning from two to three opposing layers. A three-layer flow structure is not uncommon in fjords, in particular as a feature of the background, tidally driven flow (Valle-Levinson et al., 2014). The transition from two to three layers may be explained by a framework of vertical normal modes, as the wave speed associated with the first baroclinic mode is twice that of the second mode. A trapped, propagating two-layer signal should therefore be able to exit the fjord faster than a three-layer one.

The complex zonal momentum balance in the fjord suggests that a two-layer, linear, non-rotating model like that of Farmer (1976) cannot be expected to adequately capture the physics of the fjord response. Both the non-linear and Coriolis terms act to oppose the dominant balance between wind stress and pressure gradient, thus slowing down the overall response.

Due to the weak stratification, the first baroclinic radius of deformation (3-4 km) is smaller than the width of typical wAP fjords. As a result, rotational effects are important in all phases of the fjord response of the numerical experiment. The surface flow is strongly deflected by rotation, and the along-fjord currents are highly asymmetric at all depths. Substantial cross-fjord flow also develops, as a result of Ekman deflection of the outflow. This generates strong cross-fjord

property gradients in the surface waters during the active forcing, consistent with the response described by Cushman-Roisin et al. (1994) for wind driven upwelling in a broad, infinite channel. The cross-fjord density gradient is in phase with the along-fjord currents, and suggests a tight geostrophic balance in the cross-fjord direction.

A spatially periodic cross-fjord flow pattern develops within the upper model fjord in the relaxation phase of the wind event. A previous study of wind-forced fjord currents found a similar pattern associated with baroclinic instability of the flow (Carroll et al., 2017). The exact evolution of the instability is dependent on both viscosity and fjord geometry. A complex surface flow also evolves in the relaxation phase of the more realistic wind fjord experiment, but no spatially periodic flow structure appears in this case. Details of the flow are highly dependent on the choice of parametrization of horizontal viscosity, which has limited empirical basis in small-scale coastal environments.

3.4.2 INTERNAL WAVES

The residual "ringing" observed in the model currents (e.g., Figure 3.6a) is associated with counterclockwise rotation of the current vector at a frequency near the local inertial, $|f|$ =1.8 cpd (Figure S2, supplemental material). The semi-diurnal tidal constituents also occupy this frequency band, but since only wind forcing has been applied in the model experiments, we rule out a tidal origin of the signal. We also rule out internal seiche modes (e.g. Arneborg and Liljebladh, 2001) as a generation mechanism since the frequency is consistent throughout a range of experiments with varying geometry and stratification. Instead, we interpret this signal as wind-generated near-inertial internal gravity waves (NIIGWs).

A time series of ocean currents from a SADCP time series in December, 2015 provides observational support for the presence of NIIGWs in fjords. The observed currents, measured after a minor wind episode in Andvord Bay, exhibit upward propagating phase lines with frequency near the local $|f|$. The currents are qualitatively similar to model currents forced by a simple wind impulse (Figure 3.13). The upward propagating phase is consistent with downward propagating energy according to linear wave theory (e.g. Pedlosky, 2013), and upward propagating phase lines are typically interpreted as an indication of a surface generation mechanism rather than internal tide generation from flow over topography (Leaman, 1976; Fer, 2006).

NIIGWs are a well-known part of the open ocean response to wind forcing events, and they are believed to be a major pathway of energy from the atmosphere to the interior ocean (Wunsch and Ferrari, 2004; Alford et al., 2016). NIIGWs have been observed in shelf seas (Chant, 2001; MacKinnon and Gregg, 2003), lakes (Mortimer, 2006; Valipour et al., 2015), and broad channels and semi-enclosed seas (Leder, 2002; Fer et al., 2004; van der Lee and Umlauf, 2011), but have not previously been documented on horizontal scales as small as in this study. Internal waves of tidal origin can be an important source of energy for turbulent mixing in fjords (Stigebrandt, 1976; Stigebrandt and Aure, 1989; Allen and Simpson, 1998; Ross et al., 2014), and wind-generated

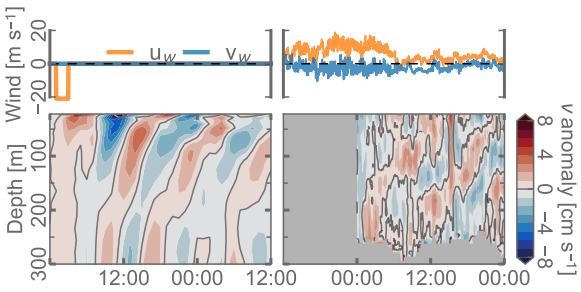

Figure 3.13: Examples of wind-generated near-inertial waves in a numerical experiment *(a)* and shipboard measurements *(b)*. *Top:* wind forcing, *bottom:* anomaly of the cross-fjord velocity component. Shipboard currents are from stationary Shipboard ADCP measurements over 24 hr near the middle of the fjord towards the northern coast on December 4th, 2015, in the aftermath of a minor up-fjord wind event. Model currents are sampled at the corresponding location in the Andvord Bay grid during the Transient experiment forced with a 2 hour, 1 Pa down-fjord wind impulse. Winds in *b* are from automated shipboard sensors.

internal waves are known to play a role in resuspension of lacustrine bottom sediment (Hawley, 2004; Austin, 2013), but it is not clear whether NIIGWs may have a significant impact on the interior waters of high-latitude fjords.

3.4.3 DEEP WATER EXCHANGE

A key hypothesis motivating this study was that down-fjord winds might drive deep heat flux into the inner fjord to impact glacier dynamics and replenish oxygen in the bottom waters. Previous studies have suggested that episodic wind events may drive significant import of external water in the deep waters of fjords (Moffat, 2014; Spall et al., 2017). Since deep water temperature typically increases offshore along the Peninsula (Costa et al., 2008; Martinson et al., 2008), wind-driven import could affect wAP glaciers, which are believed to be highly sensitive to deep water temperatures (Cook et al., 2016),

The present study offers little support for this hypothesis, as the inflow of external water masses into the inner reaches of the fjord is minimal throughout the experiments. The exchange that does occur is generally restricted to the outermost region of the fjord, and none of the experiments suggest that local wind forcing can generate import of external water towards the head of the fjord where tidewater glaciers are typically located.

We attribute the limited deep water mass exchange in this analysis compared to previous studies to a difference in methodology. This study adopts a tracer-based approach to estimate the exchange with the external ocean, as opposed to the more conventional method of integrating the volume flux across a cross-section of the fjord (e.g. Jackson et al., 2014; Spall et al., 2017). While the latter is a reasonable approach for low-frequency flows like steady wind-driven circulation or true estuarine-like circulation, it does not capture the re-export of ocean water occurring as the deep flow reverses during episodic events, and therefore overestimates the net deep ex-

change. Furthermore, the tracer approach allows the tracking of the distribution of imported water masses, in this case revealing that deep ocean water does not enter the inner fjord.

3.4.4 UPPER LAYER FLUSHING

A key result of the present study is that down-axis wind events provide an effective mechanism for flushing the upper waters of the fjord. Of the water initially located in the upper 35 m, 81% is exported from an idealized fjord when applying surface wind stress comparable to a wind event observed Andvord Bay. Even in experiments with short duration or weak amplitude, the upper layer is significantly modified.

Observations from Andvord Bay show a significant salinity increase in the top 50 m of the water column after the 2015 event. The net increase suggests that exchange, rather than vertical mixing, is the agent of the upper ocean change. A similar destratification occurs during the wind event in the model experiments; however, the observed upper ocean change persists for weeks, while the model fjord nearly reverts to its initial state within a few days of the peak forcing. There are several conceivable reasons for this discrepancy. First, the model is initialized with horizontally uniform salinity, so that lateral exchange in the model fjord only replaces the fjord waters with external waters of identical salinity. In reality, lateral exchange in the upper ocean may bring in water masses with other properties, likely denser and saltier than the native upper waters of Andvord Bay. Second, the model wind forcing is only applied in and directly outside the fjord. However, observations and simple continuity arguments suggest that wind forcing during down-fjord events in Andvord Bay also extends to the Gerlache Strait. Larger scale wind forcing could lead to coastal upwelling in the region outside the fjord, reducing the horizontal pressure gradients driving the return flow while also making the returned waters more saline.

In an experiment conducted with an unstratified top layer extending down to 150 m depth, the fraction of upper water exported from the fjord is reduced to less than 25%. In this case, surface water masses are quickly mixed down to the bottom of the unstratified layer, and at the same time the maximum outflow speeds are greatly reduced compared to the case with a slight freshening near the surface. This suggests that even a weak near-surface stratification plays a key role in concentrating the forcing into the rapid acceleration of the top layer, while in the unstratified case the energy is immediately dispersed over a much larger volume.

A wind event like the one observed in Andvord Bay in December, 2015 appears to have the potential to impact bloom dynamics in the fjord. Phytoplankton biomass inside the fjord would likely be significantly decreased by the effective export of the bulk of the euphotic zone water volume. On the other hand, exchange with the external ocean could also be a mechanism for replenishing the nutrients of depleted upper fjord waters. Future studies of phytoplankton and nutrient measurements performed from this specific event will provide insight into the details of the biogeochemical significance of such events, as well as useful validation of the results of this study.

It has previously been shown that along-fjord winds can enhance the outflow of subglacial discharge plumes in Arctic fjords (Carroll et al., 2017). Although the water exchange in the present study is surface-intensified, wind events likely act to increase the dispersal of sediment-laden, neutrally buoyant "cold plumes" which are often found around 50-150 m depth near the inner glaciers of Andvord Bay and the surrounding area (Domack and Ishman, 1993; Rodrigo et al., 2016). These plumes are a potential source of dissolved iron (Bown et al., 2017; Annett et al., 2017), and wind events may therefore drive export of trace metal export from the inner fjord to the outer ocean.

Wind events like the one explored in this study are typically associated with larger-scale atmospheric systems, and along-axis winds likely occur in many bays and fjords along the wAP simultaneously. As a result, the coastal ocean of the wAP could be exposed to episodic wind-driven pulses of glacially modified water from the coast.

Chapter 4

Buoyant meltwater plumes in a cold Antarctic Peninsula fjord

The upwelling of glacially modified water can impact fjord water masses, glacier melt rates, ocean circulation and the distribution of nutrients and geochemical tracers in high-latitude fjords. The prime driver of such buoyant upwelling in most Arctic fjord systems is the subglacial injection of freshwater, which generates buoyant turbulent plumes rising along the glacier face before spreading laterally at the surface or at a subsurface equilibrium level. Ocean observations near tidewater glaciers along the western Antarctic Peninsula have shown vertical intrusions of cold and turbid water consistent with buoyant plumes, but there is no evidence for significant subglacial discharge of freshwater in the region, and the origin of these plumes remains unclear. In this study, we examine mid-water intrusions of glacially modified waters in Andvord Bay on the northwestern Peninsula. We use observations of temperature, salinity and optical properties from hydrographic profiles during three separate research cruises as well as a near-glacier ocean glider transects to study the composition and spatial distribution of the intrusions, and use buoyant plume theory to examine the behavior of upwelling plumes in the fjord environment. Consistent with a previous hypothesis, our observations suggest that plumes originate from a deep, localized source of submarine meltwater. Glacial plumes in Andvord Bay are relatively weak compared to environments with high subglacial freshwater discharge. While glacial plumes are unlikely to drive significant melt or ocean circulation in the Andvord Bay, they may play a key role in transporting sediment and trace metals from the glacier grounding line upward in the water column and out into the fjord ocean.

4.1 INTRODUCTION

Vertical intrusions of anomalous temperature, salinity and turbidity resulting from the submarine release of buoyant water are a common feature of ocean profiles near tidewater glacier termini (Syvitski et al., 1989; Domack and Ishman, 1993; Straneo and Cenedese, 2015). When the buoyant water enters the ocean, it rises upward along the the ice-ocean interface as a turbulent upwelling plume, entraining ambient water and additional melt generated along the path of the plume (Jenkins, 2011). Ultimately, the plume reaches a level where it can rise no further, either at the surface or near the depth the where the plume waters are no longer buoyant relative to the ambient waters. From this terminal depth, the plume begins to flow horizontally into the surrounding ocean, where it can be observed as vertically localized intrusions of glacially modified water in ambient ocean profiles.

In glacial fjords, plume dynamics can impact fjord water masses (Jackson and Straneo, 2016; Carroll et al., 2017) and ocean circulation (Straneo et al., 2011; Carroll et al., 2015; Cowton et al., 2015). In many fjord systems, deep waters are relatively warm, and the entrainment and upwelling of deep water along the glacier terminus can significantly increase glacial melt (Sciascia et al., 2013; Xu et al., 2013; Kimura et al., 2014), which in turn can impact the glacier mass balance (Rignot et al., 2010; Fried et al., 2015a; Slater et al., 2015). Upwelling plumes can also provide an important mechanism for transport of suspended sediment (Ó Cofaigh and Dowdeswell, 2001; Mugford and Dowdeswell, 2011; Arendt et al., 2011) and geochemical tracers (Azetsu-Scott and Tan, 1997; Hopwood et al., 2016) from the deep waters towards the surface and down-fjord from the terminus region.

The study of glacial plumes in fjords has largely focused on tidewater glaciers in Greenland and Alaska. In these systems, buoyant plumes are typically associated with strong summer subglacial discharge of freshwater at the glacier grounding line (Cowan and Powell, 1990; McGrath et al., 2010/ed; Motyka et al., 2013; Chu, 2014). Due to the difficulty of conducting measurements in close proximity to glacier termini, very few observations have been collected within the upwelling plumes, and observational evidence is largely based on oceanographic measurements of the outflowing plume of glacially modified water some distance away from the terminus. Outflowing plumes are typically characterized by anomalous thermal, optical and geochemical (Azetsu-Scott and Tan, 1997) properties relative to the surrounding waters. Velocity measurements can also be used to detect the outflow itself (Jackson et al., 2017).

It is believed that most of the glacial surface melt from the Antarctic Peninsula Ice Sheet refreezes locally, and therefore does not enter the ocean as freshwater runoff (van Wessem et al., 2016). Additionally, there is no evidence from the wAP of channelized subglacial hydrology networks which provide efficient pathways for surface freshwater to the grounding line of glaciers elsewhere (Gray et al., 2005; Carter and Fricker, 2012/ed; Chu, 2014). Nevertheless, glacial plumes have been shown to be a feature of fjords and bays on the west Antarctic Peninsula (wAP) (Domack and Ishman, 1993; Ashley and Smith, 2000; Rodrigo et al., 2016). Domack and Williams

(1990) attributed observations of cold, turbid plumes in Andvord Bay on the northern wAP to tidal heaving of the glacier and consequent pumping of ocean water into subglacial cavities, causing resuspension of sediment and melt at the glacial base and subsequent generation of a buoyant plume. Ashley and Smith (2000) found no evidence for such subglacial cavities in a remotely operated vehicle survey of the calving face of a plume-producing glacier on nearby Anvers Island. The relative shortage of measurements of wAP glacial plumes and the uncertainty in the mechanism of their generation motivates further observational and analytical examination of plume processes at wAP glacier termini. The goal of this study is to characterize the downstream expression of wAP fjord plumes in more detail than previous studies, and to consider mechanisms of plume generations and their implications for the fjord system. We complement the observations made by Domack and Williams (1990) with our own hydrographic profiles three separate cruises at different times of the season, as well as with a single Automatic Underwater Vehicle (AUV) near-glacier survey. We study the depth, water mass properties, and optical transmission signature of the plumes and examine the spatial distribution of glacially modified waters in the fjord. We discuss mechanisms of plume generation in light of pre-existing models of ice-ocean interaction, and discuss possible implications of our findings for fjord water properties and geochemical fluxes.

4.2 DATA AND METHODS

4.2.1 STUDY SITE

This study focuses on Andvord Bay, a glacial fjord within the Gerlache Strait on the northern wAP. The general hydrography of the fjord during the *FjordEco* project was described in Chapter 2. That study characterized Andvord Bay as a dynamically quiet, cold-water fjord, with mean and tidal currents in the inner fjord on the order of $\sim$ 1 cm s^{-1}. Glacier mass flux to the ocean is dominated by calving from Bagshawe Glacier, a fast-flowing tidewater glacier located in the western cove of the inner fjord. Bagshawe Glacier flows at a rate of up to 7 m day^{-1} at its terminus (Fahnestock et al., 2016), with an estimated solid ice flux of 1.6×10^{12} kg $year^{-1}$ (Chapter 2). Deep waters in Andvord Bay are dominated by cold (-1°C to 0°C) water masses originating in the Bransfield Strait, and the fjord therefore does not exhibit the increase in temperature with depth often observed in Greenland fjords (Straneo et al., 2012) as well as in coastal areas further south along the wAP (Moffat and Meredith, 2018).

4.2.2 OBSERVATIONS

Profiles of conductivity, temperature and depth (CTD) were collected in Andvord Bay during three research cruises to Andvord Bay between November 2015 and April 2017 as part of the *FjordEco* project, (Table 4.1, Figure 4.1). A subset of the profiles were collected within the area

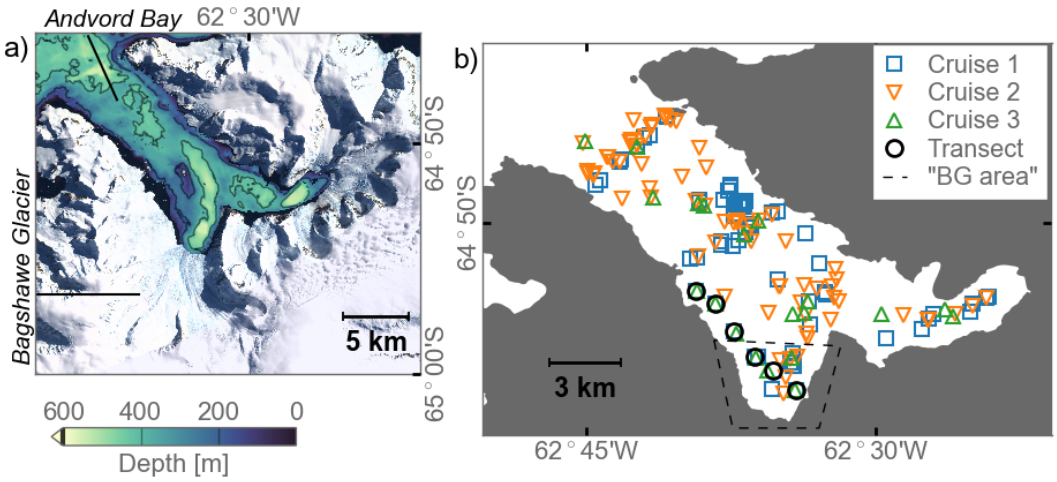

Figure 4.1: *a)* Andvord Bay Bathymetry from Global Multi-Resolution Topography product (Ryan et al., 2009). Land imagery from Landsat Image Mosaic of Antarctica. Multibeam and imagery data available from the U.S. Geological Survey. *b)* Overview of CTD measurements in Andvord Bay.

close to Bagshawe Glacier (labelled *BG* in Figure 4.1). The innermost profiles were collected within ~500 m of the terminus of Bagshawe Glacier. During Cruises 1 and 3, a repeat survey was conducted extending along the Terminus of Bagshawe Glacier.

A fluorometer (Wet Labs ECO-AFL/FL) and an optical transmissometer (Wet Labs C-Star with optical path length 25 cm) were also mounted on the CTD rosette. Percentage beam transmission, BT, was converted into optical attenuation coefficient c and path length l using the following formula:

$$c = -\frac{\ln(BT)}{l} \tag{4.1}$$

We find overall discrepancies between clear-water beam transmission values during the three cruises, suggesting a discrepancy in instrument calibration between the cruises. This study therefore uses optical attenuation coefficient only as a qualitative measure of gradients within each cruise, and we do not attempt to compare absolute values between the different cruises. A more thorough discussion of the optical properties of the plumes can be found in Pan et al. (in prep.).

In addition to the CTD measurements, we obtained near-glacier measurements from a Slocum gliding AUV ("ocean glider", Teledyne Inc.). The ocean glider included sensors measuring, pressure, salinity, temperature, and optical backscatter. The presence of sea ice and large icebergs prevented extensive use of the ocean glider, but a successful deployment was conducted over a 24-hour period on 22 April 2016 near the terminus of Bagshawe Glacier.

		CTD dates		# CTD profiles	
	Cruise ID	*Start*	*End*	*AB*[a]	*BG*[b]
Cruise 1	LMG15-10	23 Nov 2015	22 Dec 2015	105	10
Cruise 2	NBP16-03	3 Apr 2016	23 Apr 2016	72	4
Cruise 3	LMG17-02	26 Feb 2017	9 Mar 2017	20	5

[a] All profiles in Andvord Bay.

[b] Outer Fjord and Middle Fjord (excluding wind event).

Table 4.1: Overview of CTD data.

4.2.3 DETECTION AND ANALYSIS OF GLACIALLY MODIFIED WATER

A number of methods have been employed in order to detect glacially modified waters within an ambient ocean environment. In many cases, glacially modified waters can be recognized by increased turbidity or optical attenuation as a result of subglacial release of turbid meltwater. In cases where the signal is more subtle or associated with ocean-driven melt rather than freshwater discharge, a common method is to measure chemical tracers such as noble gases (Loose and Jenkins, 2014) or certain stable isotopes (notably δ^{18}O) which have a different signature in ocean water than in glacial melt. However, the methods involved in such measurements are complex and resource-demanding. Temperature and salinity are significantly easier to measure than to most geochemical tracers, and it is therefore comparatively easy to obtain a significant number of measurements. The use of temperature and salinity as tracers of meltwater is complicated by the fact that several water masses are typically present in the ambient ocean waters, and the classification of meltwater therefore rests on some assumptions about the ambient water which are typically simplifications which can generate misleading results (Beaird et al., 2015). Nevertheless, it is useful in the absence of other tracers to examine the temperature and salinity properties of seawater.

4.2.3.1 *θ-S analysis of near-glacier ocean waters*

When a mass m_i of ice melts in a mass m_a of ambient seawater in a closed thermodynamic system, the resulting average salinity S_m after melting and mixing is simply a linear combination of the contributions from the seawater with salinity S_a and the ice with salinity S_i. The same is not the case for temperature, since heat is lost from the ocean to the ice both through mixing with meltwater, warming of ice from initial temperature θ_i to freezing temperature θ_f, and through the heat required to effectuate the phase change from ice to liquid water. As a result, the final system has average temperature and salinity θ_m, S_m given by:

$$S_m = S_a - \frac{m_i}{m_i + m_a}(S_a - S_i) \tag{4.2}$$

$$\theta_m = \theta_a - \frac{m_i}{m_i + m_a}\left(\theta_a - \left[\theta_f - \frac{c_i}{c_w}(\theta_f - \theta_i) - \frac{L}{c_w}\right]\right) \tag{4.3}$$

where c_i, c_w are the specific heat capacities of ice and seawater, respectively, and L is the latent heat of fusion of ice. The resulting mixture is equivalent to a linear combination of the original sea water and a second *effective* water mass with salinity $S_{eff} = S_i$ and (potential) temperature

$$\theta_{eff} = \theta_f - c_i c_w^{-1}(\theta_f - \theta_i) - L c_w^{-1} \tag{4.4}$$

The rightmost term ($Lc_w^{-1} = 84.3°\text{C}$) dominates Equation 4.4, and θ_{eff} is typically in the range $-100°\text{C}$ to $-84°\text{C}$.

The mixture of ambient seawater and ice melt is found along straight lines in $\theta - S$ space between the original seawater values and those of the effective water mass. Such lines are often labelled *Gade lines* in acknowledgement of the development of the theory by Gade (1979). Typically, S_i is assumed to be zero, and the temperature of the ice near the ocean is assumed to be close to the freezing temperature. In such cases, the slope of a Gade line is given by

$$\frac{d\theta}{dS} = \frac{\theta_a - \theta_{eff}}{S_a - S_{eff}} = \frac{\theta_a - \theta_f + \frac{L}{c_w}}{S_a} \tag{4.5}$$

The pressure- and salinity-dependent freezing point of water imposes a limit the maximum fraction of meltwater which can be contained by the seawater without refreezing. We will refer to ambient water with this maximum amount of meltwater as *melt-saturated water*. The temperature and salinity θ_{SAT}, S_{SAT} of the melt-saturated water is defined by the intersection in θ, S space between the local Gade line and the line defining the freezing point of seawater.

Characteristic θ, S "melt lines" with a slope given by (4.5) are a common characteristic of ocean waters near areas of ocean-driven melt, such as ice shelves and icebergs. Due to the low values of θ_{eff}, the "melt line" slope is in most situations distinct from the mixing line between ambient water and freshwater ($\theta = 0$, $S = 0$) from surface or subglacial freshwater discharge, and an evaluation of θ, S properties of near-glacier waters can be a useful way of distinguishing between these processes.

In the ocean, the situation is complicated by the buoyancy change associated with the melt process. For the closed system described above, the average water density after melting, $\rho(\theta_m, S_m)$, is different from that of the initial state, $\rho(\theta_a, S_a)$. For the typical $\theta - S$ range in the high-latitude ocean, density is mainly controlled by salinity, and the result of an injection of meltwater is a decrease in water density, leading to buoyancy-driven upwelling. Since both the ocean water properties and the freezing point changes with depth, the meltwater mixes with water of different $\theta - S$ properties as it ascends upward, and meltwater from different depths have different values of θ_{eff}. For the case of ambient waters which are uniform or the result of linear mixing between two distinct water masses, the meltwater fraction associated with a single measurement of θ and

S can be obtained from linear water mass analysis (Jenkins, 1999). However, the ambient water mass θ, S distribution in the deep waters of Andvord Bay cannot be reasonably approximated as linear, and we therefore only use Gade line analysis qualitatively to identify the signature of melt processes.

4.2.3.2 *Buoyant plume theory*

Buoyant plume theory (BPT) was first developed by Morton et al. (1956) in the study of plumes generated by hydrothermal vents in the ocean. The theory was later modified by (Jenkins, 1991) for the application to ice-ocean interactions, including the entrainment of meltwater generated by a plume upwelling along an ice-ocean interface. BPT has since been applied widely to the study of glacial plumes generated at tidewater glaciers (e.g., Cowton et al., 2015; Magorrian and Wells, 2016; Jackson et al., 2017). Carroll et al. (2015) found good agreement with the outflowing plumes predicted by BPT when compared to a complex, three-dimensional numerical model. Here, we use the model formulation described in Jenkins (2011). This formulation, which we will refer to as a "line plume", assumes an outflow of finite width, creating a wedge-shape upwelling plume. Other formulations assume a point flow, generating an axi-symmetric "cone plume". We choose the former since the latter is better suitable for the case of distinct point outflow associated with well-developed channelized subglacial hydrology network. Jackson et al. (2017) found that even in such cases, a line plume geometry may be more appropriate.

The BPT model consists of simplified conservation equations for a rising plume which entrains ambient water, as well as entrainment of meltwater from the (vertical) ice face that is determined using a simplified melt model from (McPhee, 1992). The dependent variables are plume width W, plume upward velocity U, plume water temperature T, and plume water salinity S. The equations are evaluated starting from the bottom of the plume, where it is initialized with an initial volume flux Q with temperature T_d and salinity S_d.

The increase in plume volume flux with depth depends on the entrainment rate, E, and melt rate, M, both of which are always positive:

$$\frac{d(WU)}{dz} = E + M \tag{4.6}$$

where the z coordinate is oriented along the ice edge, which for the case of a vertical glacier terminus is equivalent to the vertical coordinate. The rate of change in upward momentum flux is dependent on buoyancy acceleration and drag K:

$$\frac{d(WU^2)}{dz} = Wg' - K \tag{4.7}$$

where $g' = g(\rho - \rho_a)/\rho_0$, where g is the gravitational acceleration, ρ and ρ_a the density of plume water and ambient water, respectively, and ρ_0 a reference density. The heat and salinity

conservation equations contain contributions from entrained ambient water at temperature T_a and salinity S_a, entrained meltwater at temperature T_m and salinity S_m, as well as the turbulent exchange with the near-ice water, parametrized with the turbulent exchange coefficient $G_{T,S}$.

$$\frac{d(WUT)}{dz} = ET_a + MT_m - G_T(T - T_m) \tag{4.8}$$

$$\frac{d(WUS)}{dz} = ES_a + MS_m - G_S(S - S_m) \tag{4.9}$$

The equation set (4.6) - (4.9) form the governing BPT equations. In this study, we follow the approach of Jenkins (2011), involving parametrizations of drag, entrainment, turbulent exchange and melt. Drag K and entrainment rate E are parametrized as quadratic and linear functions of velocity, respectively:

$$E = eU \tag{4.10}$$

where $e = 0.036$ is an entrainment coefficient, and:

$$K = \kappa U^2 \tag{4.11}$$

where $\kappa = 2.5 \times 10^{-3}$ is a drag parameter. The turbulent transfer coefficient is parametrized as:

$$U\kappa^{-1/2}\Gamma_{T,S} \tag{4.12}$$

where $\Gamma_{T,S}$ is the turbulent transfer coefficient for temperature and salinity, respectively.

The melt rate is calculated using a simplified parametrization following McPhee (1992):

$$ML + Mc_i(T_f - T_i) = c_w\kappa^{1/2}U\Gamma_{T,S}(T - T_f) \tag{4.13}$$

The freezing temperature T_i is calculated as a function of plume depth and salinity:

$$T_f = \lambda_1 S + \lambda_2 + \lambda_3 z \tag{4.14}$$

where $\lambda_1, \lambda_2, \lambda_3$ are known constants.

In our applications, the BPT equations were numerically integrated upwards from an injection depth z_0 to the terminal equilibrium depth z_{EQ}. We assumed that at this depth, the plume flows outward into the fjord with a volume flux (per width) $Q_{EQ} = U_{EQ}W_{EQ}$ (units m^2 s-1). z_{EQ} was

taken as the level where the the plume waters become neutrally buoyant ($\rho - \rho_a \leq 0$). In reality, the plume retains upward momentum at the equilibrium level, and will overshoot z_{EQ} along the glacier. However, z_{EQ} was shown in Carroll et al. (2015) to be a good approximation to the depth at which the outflowing plume ultimately settles downstream. We initialized the plume model with a volume flux (per width) Q_0 at an injection depth z_0. The initial diameter and velocity of the plume were calculated from Q_0 by setting the left hand side of Equation 4.7 to zero, equivalent to assuming zero initial upward momentum flux. We assumed an ice temperature $T_i = -5°C$, noting that the slope of the Gade line is relatively insensitive to modest changes in this parameter.

4.3 RESULTS

4.3.1 OBSERVATIONS OF MID-WATER PLUMES

4.3.1.1 *Example profile*

Intrusions of low temperature and elevated optical attenuation were a consistent feature of CTD profiles from inner Andvord Bay during the FjordEco measurements. An example is given in Figure 4.2, which shows a CTD profile taken close to Bagshawe Glacier on 10 December 2015. Two distinct cold anomalies are identified in the temperature profile: a narrow, strong minimum at 45 m to 70 m depth and another, broader minimum between 100 m and 155 m depth. The shallower temperature anomaly reaches a temperature of -0.8°C, a decrease of ~0.4°C compared to the surrounding waters. Associated with the minimum near 50 m is a decrease in salinity by ~0.02, such that the salinity gradient in fact becomes negative between 47 m and 52 m, directly above the temperature minimum. The density effects of salinity and temperature compensate each other in this area, such that the stratification remains weak but stable throughout the profile. No clear salinity anomaly is identified in the deeper temperature minimum.

Associated with both temperature minima were corresponding maxima in optical attenuation (Figure 4.2b). No distinct signal was found at either depth in the fluorescence profile (not shown), and we interpret such mid-water increases in optical attenuation as suspended inorganic particles. Also notable in the profile of optical attenuation was a strong increase below 250 m, towards a maximum at ~330 m. A similar broad maximum extending $>$ 100 m above the bottom was consistently found within the inner basins of Andvord Bay during all cruises (Figure 4.4).

The relationship between low temperature and high optical attenuation was evident throughout the FjordEco CTD dataset (Figure 4.3). Values of attenuation, c, above 1.0 were only observed in the profile from 10 December 2015, but the vast majority of instances of $c > 0.3$ were also associated with a distinct low temperature anomaly.

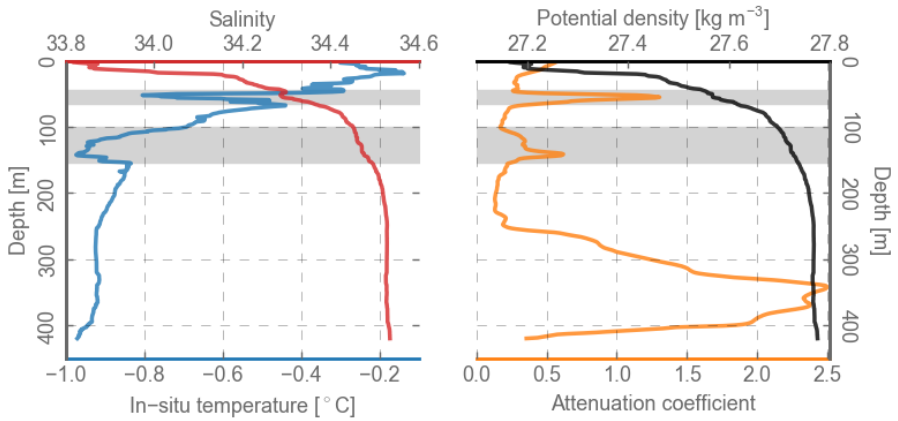

Figure 4.2: Profiles of salinity (red), in-situ temperature (blue), attenuation coefficient (orange) and potential density (black) from a CTD profile collected in Andvord Bay on 10 December 2015, approximately 1.1 km from the terminus of Bagshawe glacier. Areas of mid-water plumes highlighted in gray.

4.3.1.2 *Spatial distribution*

Figure 4.4 shows the distribution of elevated optical attenuation throughout the CTD dataset. In addition to the consistently high values in the deep basins of the inner fjord (within 6 km of Bagshawe Glacier), attenuation was also elevated in the upper 30 m of the water column throughout the fjord. We attribute the high values near the surface to optical attenuation by phytoplankton and other marine organisms, which were concentrated in the euphotic zone (Figure 4.4e). During all three cruises, we found localized maxima of elevated optical attenuation below the euphotic zone, in the upper part of the column. Such layers were typically found between 40 m and 200 m (Figure 4.4b, c, d), with the highest occurrence at ∼100 m. In the rest of this study, we concentrate on exploring the signal in the the depth range between 50 m to 200 m, where we are confident that the optical signal is associated with sediment turbidity. We will refer to depth range as the *upper mid-water* range.

Figure 4.5 shows the maximum and mean attenuation coefficient with in the upper mid-water range as a function of distance from the glacier terminus. Values are highest near the Bagshawe Glacier terminus, and decrease down-fjord. Beyond 10 km from the terminus, the mean and maximum attenuation stabilizes and we do not observe obvious intrusions.

4.3.1.3 *Near-glacier transects*

A CTD transect extending over 6.3 km across the southern cove in front of Bagshawe Glacier was repeated during Cruise 1 and Cruise 3 (Figure 4.6). The transects consisted of 6 stations starting from the southeastern end, progressing across the cove in front of the glacier terminus and ending along the western coast. In addition to the CTD surveys, the ocean glider was deployed in the area during Cruise 2. Here, we discuss a single glider transect within some hundred metres of Bagshawe Glacier. The path of the glider is shown in Figure 4.6.

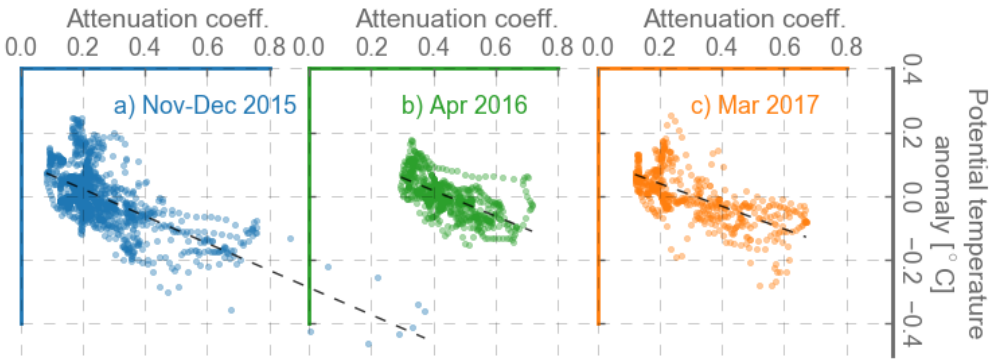

Figure 4.3: Scatter plots of attenuation coefficient, c, and potential temperature θ anomaly compared to average potential temperature at measurement depth within the "BG" area. Only included are the 50-200 m depth range and deployments from the BG area. Black dashed lines show best linear fit to observations.

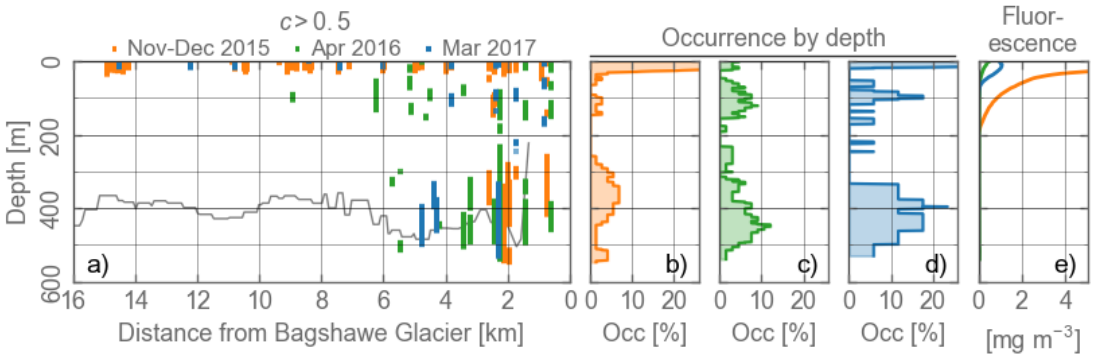

Figure 4.4: *:)* Spatial location of measurements of attenuation coefficient c >0.5 in the FjordEco CTD dataset. Gray line shows bathymetry along a line extending through the center of the fjord (see inset map, Figure 4.5 below, which also shows the location of the CTD observations). *b, c, d:* Occurrence y depth of c >0.5 in the entire fjord CTD dataset during each cruise. Note that the spatial distribution of measurements varied between the cruises. *e*: Average fluorescence during each cruise.

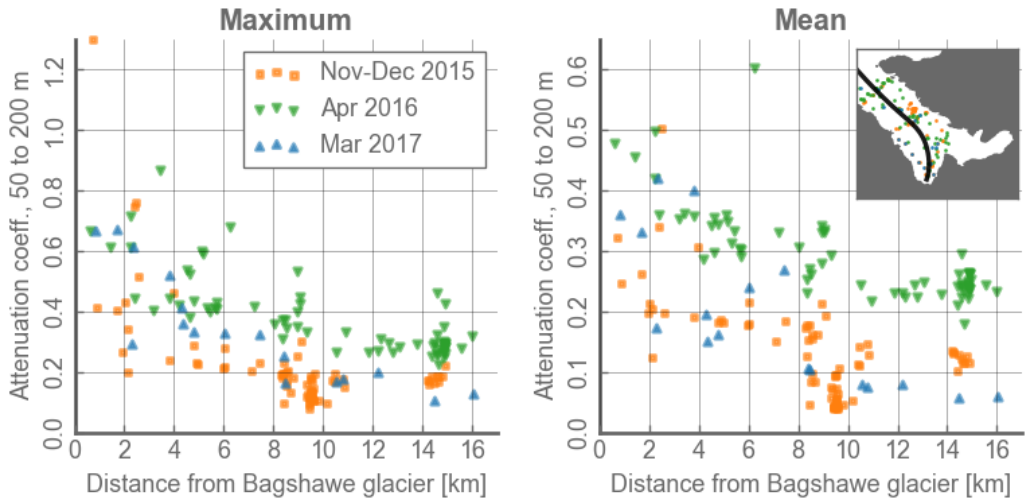

Figure 4.5: Maximum (*a*) and mean (*b*) attenuation coefficient between 50 and 200 m depth from FjordEco CTDs as a function of distance from the terminus of Bagshawe Glacier. Inset figure (*c*) shows the included casts and the reference line used to calculate "Distance from Bagshawe Glacier". The latter is calculated by mapping each point onto the closest point on the reference line.

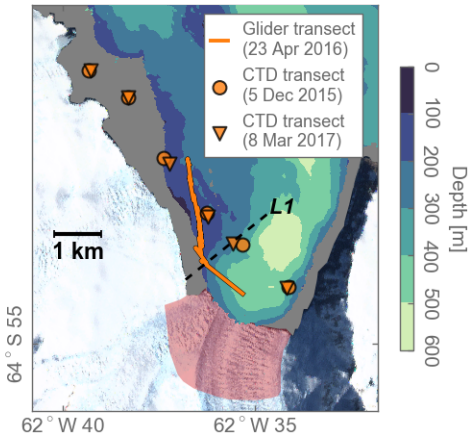

Figure 4.6: Map of measurement locations from near-glacier glider and CTD transects. The terminus is emphasized in red. The exact location of the terminus is based on the Global Self-Consistent Hierarchical High-resolution Geography shoreline product, and not necessarily representative of the terminus location during the measurements.

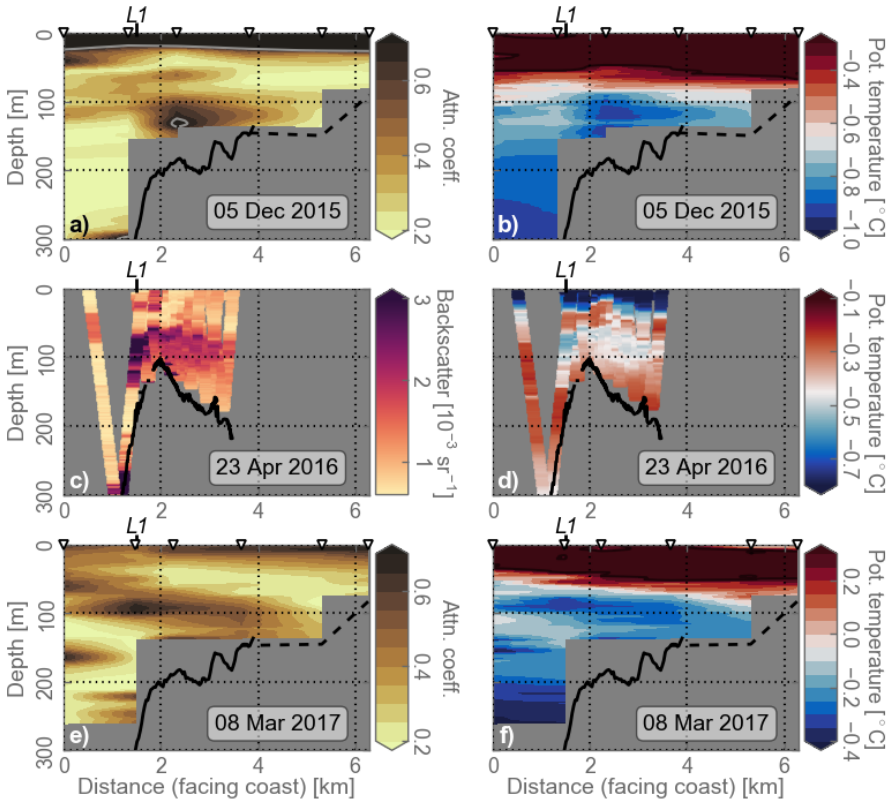

Figure 4.7: Transects near Bagshawe Glacier during the three FjordEco cruises. Note the differing color scales in the various plots, which are chosen to emphasize upper mid-water gradients. Full black lines show underlying bathymetry, where available. Dashed black lines show an estimated underlying bathymetry based on the CTD measurements.

The panels on the left of Figure 4.7 show optical properties along the transects. Although optical attenuation (measured by the CTD) and backscatter (measured by the glider) are separate quantities, both can be seen as proxies for suspended inorganic matter in the absence of other scatterers like phytoplankton, and for simplicity we will refer to both quantities as *turbidity*. During all three transects, we found a maximum in turbidity near 100 m depth off the western end of the Bagshawe Glacier terminus, near the line labelled *L1* in Figure 4.6. In the glider transect from April 2016 (Figure 4.7b), the maximum was found close to the bottom, in an area where the bathymetry rises rapidly from the deep basin in front of the glacier, to a shallow (∼100 m) maximum before deepening slightly towards the north. The backscatter signal is strongest on the basin side of this bathymetric maximum, but the signal also appears to "spill over" to the north along the transect. In the CTD measurements (which were taken ∼ 700 m further from the coast along L1), the attenuation maxima were not as closely connected to the underlying bathymetry. The pattern is consistent with flow of turbid water along the terminus, deflected by bathymetry into the fjord approximately along the L1 line.

In all three transects, turbidity maxima were co-located with negative temperature anomalies relative to the surrounding water. The relationship between temperature and turbidity was evident both in the broad maxima and in smaller-scale features elsewhere along the transect.

Figure 4.8 shows the θ, S distribution of the three along-glacier transects. Also shown are the distributions based on depth average profiles from the BG area and the fjord as a whole, respectively. During all cruises, the upper mid-water range was cool relative to the rest of the fjord.

The greatest temperature anomaly compared to the ambient waters was found in the April 2016 glider transect, where the waters at ∼ 65 m depth were 0.3°C to 0.4°C colder than the average BG area temperatures at the same depth. The slope of the θ, S distribution between 60 and 200 m in the glider transect aligns closely with the melt line defined in Equation 4.5. The greatest maxima during the CTD transects were found near the bottom, but similar slopes are found locally in parts of the two CTD transects, most notably between 90 m and 130 m in the transect from March 2017.

Negative θ, S excursions were associated with elevated turbidity, with the exception of a cluster of measurements during the March 2017 transect (near the point labelled "157 m" in Figure 4.8c). The glider transect from April 2016 was conducted closest to the glacier, and also exhibits the most striking θ, S characteristics, with observations aligning closely with local Gade lines.

4.3.2 BUOYANT PLUME MODEL

4.3.2.1 *Model plume characteristics*

The characteristic Gade line slope found in the near-glacier waters during the glider transect strongly suggest a subglacial meltwater source. The alignment of the glider observations along the same line suggests a source at a specific depth rather than multiple sources distributed across the glacier face. These observations, together with the associated turbidity signal, are consistent

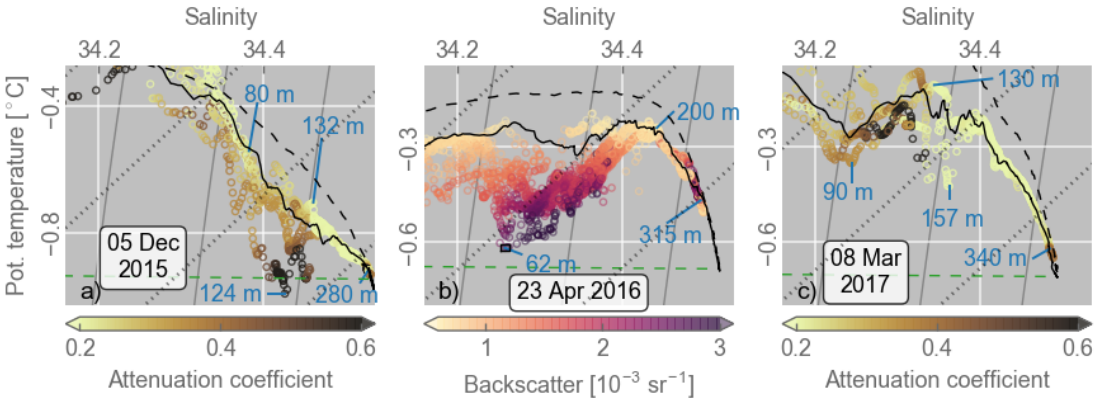

Figure 4.8: Scatter plots of potential temperature and salinity from the transects shown in Figure 4.7. Points are colored by optical attenuation coefficient (*a*, *c*) and backscatter (*b*). Black lines show cruise average temperature and salinity for the entire fjord (solid lines) and for the Bagshawe Glacier area (dashed lines). Solid gray lines show isopycnals, dotted grey lines show "melt lines" defined in Equation 4.5. Blue labels indicate the measurement depth of a few select points. Green dashed lines show example mixing lines for mixing with freshwater runoff. Note the differing temperature ranges.

with the suggestion by Domack and Williams (1990) of a source of glacier melt near the glacier grounding line. To further examine the properties of plumes generated by localized meltwater release, we conducted a series of numerical experiments using the framework of BPT.

The BPT equations for a line plume (Section 4.2.3.2) were solved numerically, using average profiles from CTD measurements in the BG area during Cruise 2 as ambient boundary conditions.

We assumed that the meltwater release at depth consisted of local ambient water saturated with meltwater with temperature and salinity θ_{SAT}, S_{SAT} calculated from the local ambient properties. Based on the observed θ, S distribution and near-glacier multibeam bathymetry, we evaluated the model using release depths z_0 between 150 m and 350 m. Lacking observational constraints for the outflow volume flux, we prescribed a range of values for Q_0 spanning three orders of magnitude from 1×10^{-3} m2 s^{-1} to 3×10^{0} m2 s^{-1}.

Figure 4.9 shows an example of the solutions to the BPT equations for z_0=250 m and different values of Q_0. The plume rises relatively steadily along the glacier face, increasing in diameter towards the terminal depth, z_{EQ}. As it travels upward, the plume encounters ambient waters of successively lower density, and the plume water density itself decreases due to entrainment. As a result, the density difference $\Delta\rho$ between the plume and ambient waters decreases continually until reaching zero at z_{EQ}. Since $S_0 = S_{SAT}$ is relatively high (> 33) the buoyancy forcing is weak and the vertical velocities small (< 50 cm s^{-1}) compared to cases with subglacial freshwater discharge. Entrainment is proportional to velocity, and the profiles of E and U therefore mirror each other. Along-plume melt rate M increases as the plume temperature T rises along the plume, but then decreases towards z_{EQ} as the velocity drops. Since both entrainment and melt are weak

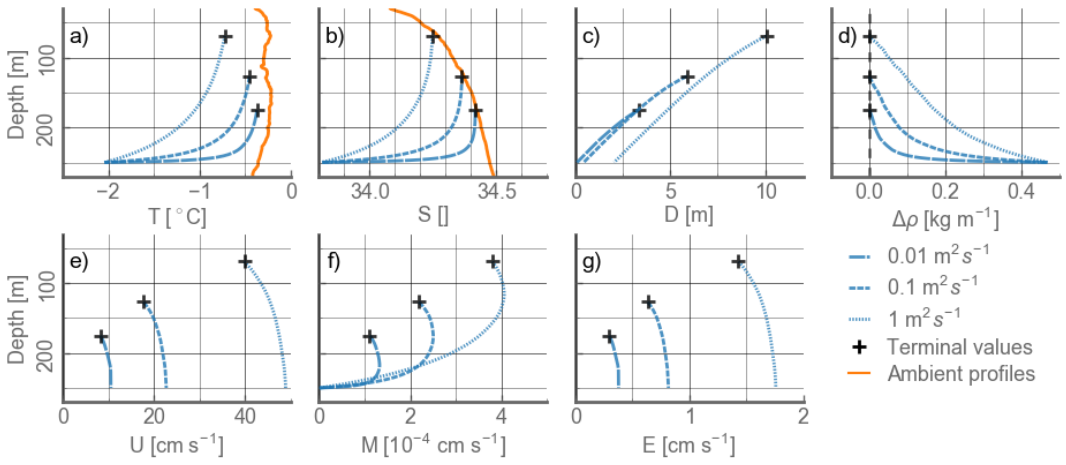

Figure 4.9: Profiles of a plume generated by the release of a saturated meltwater mixture at a grounding line depth 250 m. Mean temperature and salinity from CTD measurements in the BG area during Cruise 2 (shown in orange lines) are used as ambient water boundary conditions. Blue lines show the along-plume properties for a flux (per outflow width) spanning two orders of magnitude. Plume properties at the terminal, equilibrated level are shown in black crosses. The quantities are potential temperature (*a*), salinity (*b*), plume width (*c*), density difference between plume and ambient water (*d*), vertical velocity (*e*), glacier melt rate (*f*) and rate of entrainment of ambient water (*g*).

due to the low velocity and temperatures, the terminal plume width is relatively small ($\sim$ 1 m to $\sim$10 m).

Plume waters at z_{EQ} consist of a mixture of the initially injected water, entrained ambient waters and a small (<0.04 %) amount of melt generated along the plume. Greater values of Q_0 generate wider and colder plumes at shallower terminal depths. Since density is mainly a function of salinity within the temperature range in question, plume salinity at the terminal level is only slightly fresher than the ambient waters. Due to the freshening of the ambient waters towards the surface, equlibrium depth z_{EQ} was found below the surface throughout the range of experiments.

The terminal depth, z_{EQ}, and temperature, θ_{EQ}, and the final composition of the plume waters at z_{EQ} all vary as a function of the outflow flux, Q_0 (Figure 4.10). z_{EQ} increases sharply for small values of Q_0, but as the terminal depth approaches the halocline it becomes more difficult for the plume to overcome the stratification, causing a decrease in $\frac{dz_{EQ}}{dQ_0}$. When Q_0 is increased, the upwelling velocity also increases, but at a sublinear rate. As a result, the increases in along-plume melt and entrainment with Q_0 are also sublinear, and the fraction of the plume waters which consists of the buoyant water initially released at depth, Q_0/Q_{EQ}, increases with Q_0. As a result, θ_{EQ} decreases with depth due to the low temperature of the initial meltwater mixture.

4.3.2.2 *Comparison with observations*

The values of salinity and temperature observed at the temperature minimum of the mid-water plume during the April 2016 glider transect (S = 34.26, $\theta = -0.619$°C) are also shown as dashed

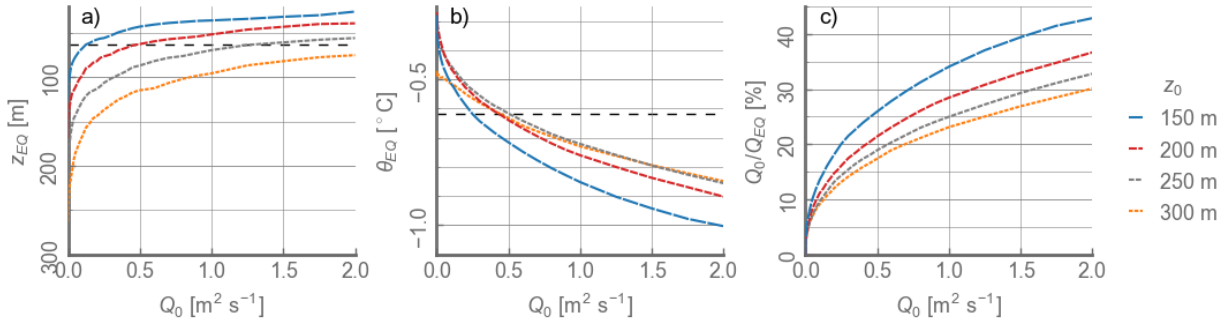

Figure 4.10: Terminal plume properties for a range of meltwater fluxes, Q_0, and grounding line depths, z_0. *a)* Terminal plume depth, z_{EQ}, *b)* potential temperature, θ_{EQ}, *c)* fraction Q_0/Q_{EQ} of the initial source volume flux to the terminal volume flux at depth. Black dashed lines show the depth and potential temperature of the coldest mid-water measurement from the 22 April 2016 glider transect (labelled "62 m") in Figure 4.11).

lines Figure 4.10. Visually, we see that the best match to the plume model is found toward the lower end of the range used for Q_0, and for outflow depths between 200 and 250 m. The best match throughout the parameter range was found for $Q_0 = 0.5$ m^2 s^{-1} and $z_0 = 220$ m. The latter is similar but deeper than the depth obtained by extrapolating the local Gade line towards the intersection with the ambient profile (180-200 m).

Using $Q_0 = 0.5$ m^2 s^{-1} and $z_0 = 220$ m, we obtain a terminal volume flux Q_{EQ}= 2.48 m^2 s^{-1} and meltwater mixture content Q_0/Q_{EQ} = 20.1%. The remaining water is a combination of entrained ambient water from depth (79.8%) and a small amount of meltwater generated by the plume (0.02%).

For large initial volume flux ($Q_0 > 0.01$ m^2 s^{-1}), the distribution of θ_ρ, S_ρ at fixed injection depth lie along a line with slope slightly smaller than that of the local Gade lines (Figure 4.11). For smaller Q_0, the entrained water fraction becomes greater, and the distribution tends towards the ambient water properties deeper in the water column. Terminal model plume water temperature and salinity are found in a similar region to the plume waters observed during the glider transect (also shown). The observed distribution is found within the range of model results generated by an outflow at between 150 m and 250 m. It is worth noting that mixing between a laterally spreading plume and ambient waters would occur along isopycnals. When comparing observed properties with those from the buoyant plume model, the corresponding z_0 should therefore be considered an upper bound on the grounding line depth.

In the small Q_0 range, we find a clear discrepancy between the buoyant plume model and the observations, the latter aligning more closely with the local Gade line even at small deviations from the ambient line. In the high Q_0 range, the tendency of the observations is more similar to that of the model with fixed grounding line depth and varying Q_0, although the latter has a slightly smaller slope than the former, which aligns more closely with the Gade line.

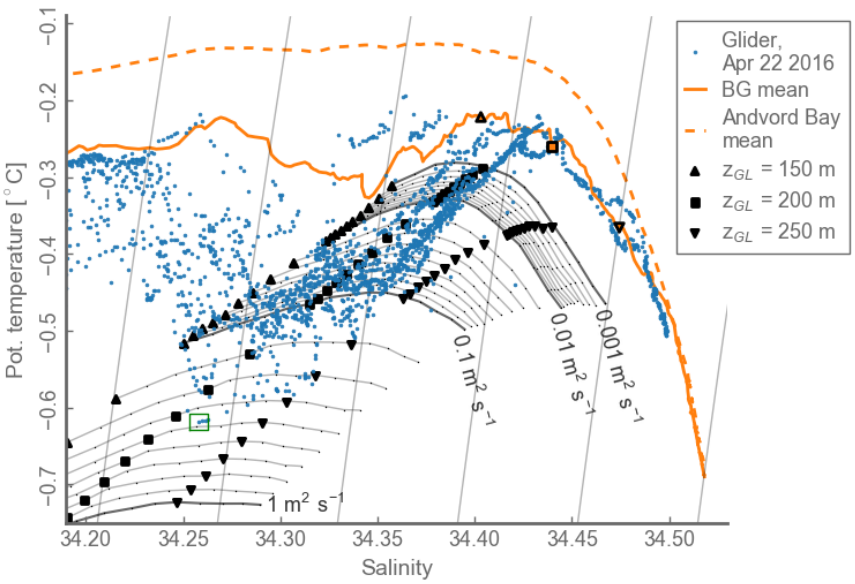

Figure 4.11: θ, S distribution of measurements during the glider transect (blue dots) and terminal plume water properties (black symbols). Terminal plume properties are obtained by evaluating the buoyant plume model with the average temperature and salinity from CTD measurements in the BG area during Cruise 2 (solid orange lines) as ambient profiles, and with a range of outflow depths and outflow fluxes. Gray contours show terminal properties for constant outflow flux Q_0 at various outflow depths z_{GL}. Average distributions from the entire cruise are shown in dashed orange lines.

4.4 DISCUSSION AND CONCLUSIONS

4.4.1 ORIGIN OF UPPER MID-WATER INTRUSIONS

During three cruises spanning the summer season, we observed upper mid-water intrusions of anomalously cold water temperature and elevated optical turbidity in the inner reaches of Andvord Bay. In light of the analysis above, we interpret these intrusions of glacially modified water masses. Glacially modified water was typically found between 40 and 200 m depth, decaying in strength and frequency of occurrence away from the glacier terminus, supporting the idea of a subsurface glacial source. These observations are in line with previous observations of vertical intrusions near Bagshawe Glacier (Domack and Williams, 1990) and other glaciers elsewhere on the northern wAP (Ashley and Smith, 2000; Rodrigo et al., 2016). Glacially modified waters were found at a similar location near the western end of the Bagshawe Glacier terminus in transects during three separate cruises, suggesting a consistently outflowing plume.

The observed properties and spatial distribution of glacially modified water are consistent with a process by which relatively fresh water is released at depth at the glacier terminus. The injection of buoyant water generates an upwelling plume, where water travels upwards along the glacier face while entraining ambient water and meltwater from the glacier face. The plume settles near a mid-water depth level where the plume density equals that of the ambient ocean. At this level,

the plume becomes a source of a neutrally buoyant water mass of anomalous temperature and salinity which flows horizontally away from the glacier. The composition of this water mass is a combination of the source waters released at depth, glacier melt generated along the plume path and deeper ambient waters entrained by the upwelling plume.

Buoyant glacial plumes are commonly observed in glacial fjords, often as a result of subglacial discharge of freshwater originating from surface melt of the glacier (e.g., Syvitski, 1989; Mankoff et al., 2016). In such cases, the subglacial source waters have a salinity near zero, and are therefore highly buoyant when released at depth. In the absence of melt, the plume waters consist of a mixture of ambient water and freshwater, which in the case of Andvord Bay would give a water mass composition which in many cases is inconsistent with the temperature and salinity distribution observed in plumes near Bagshawe Glacier. Furthermore, glacial ablation from surface melt is believed to be small on the Antarctic Peninsula compared to, e.g., Greenland (Vaughan, 2006; van Wessem et al., 2016), and there is no evidence supporting surface runoff reaching the glacier bed along the Peninsula. Lastly, near-glacier ocean observations exhibit characteristic distribution along "Gade lines", a commonly used indicator of meltwater generated by ocean-driven melt rather than a surface source (e.g., Bartholomaus et al., 2013).

Another possible source of subsurface buoyant water masses is direct melting of the glacier face through heat transfer from the ocean to the ice. Increased ocean-driven melt due to warming ocean temperatures has been closely associated with the retreat of tidewater glaciers and ice-sheet mass loss in both hemispheres (Straneo and Heimbach, 2013; Cook et al., 2016). Ocean-driven melt is often amplified by buoyant plumes, which act to increase along-glacier ocean currents. In cases where ambient ocean temperature increases with depth, buoyant plumes also distribute deeper warm waters to a shallower regions of the glacier face, driving additional melt. Warm deep waters are a common feature in many Arctic fjords, as well as much of coastal west Antarctica and the wAP. However, in the case of the northern wAP, including Andvord Bay, subsurface water temperatures are typically cold ($< 0^{\circ}$C), and decreasing with depth. The overall thermal driving of melt along the glacier is therefore low, and melt-driven upwelling does not have the potential for a positive thermal feedback driving additional melt. Nevertheless, some amount of ocean-driven melting occurs at any ocean temperature above the pressure-dependent freezing point (Jenkins, 1999), and therefore also along the face of Bagshawe Glacier. However, we find that the meltwater fluxes along the face of the glacier are insufficient to generate buoyant plumes travelling over large distances along the glacier face. Furthermore, the most likely source of the optical anomalies observed in the mid-water intrusions is erosion at the glacier bed, suggesting a localized source near the grounding line rather than melt distributed along the entire terminus area.

Discounting freshwater discharge and along-face melt, our analysis instead suggest a point source of turbid, ocean-driven meltwater at depth. This is consistent with the mechanism proposed by Domack and Ishman (1993), where meltwater is released from subglacial cavities near the grounding line.

4.4.2 SOURCES OF SUBSURFACE MELTWATER

Domack and Ishman (1993) proposed tidal heaving of the glacial terminus as a mechanism for pumping ambient water in and out of ice cavities near the grounding line, driving melt and resuspension of sediment. The resulting water masses would be a mixture of ambient and meltwater with a high suspended sediment content, which would exit the cavities and generate a buoyant plume during the outgoing tidal phase. However, observations from Andvord Bay (Chapter 2) suggest that tidal range is relatively small ($\sim$1 m), and we have found no evidence of tidal flexure of the glacier in time lapse photo records from the glacier (not shown). Furthermore, Bagshawe Glacier is likely grounded near its terminus, and the mechanical properties of glacial ice is unlikely to allow tidal flexure of the glacier over such a small distance. The mechanism by which ocean-driven meltwater could be released near the grounding line therefore remains undetermined. In the following paragraphs we propose a speculative, but theoretically conceivable alternative mechanism, but stress that further knowledge of the glacial geometry, or at the very least a much more detailed theoretical glaciological analysis, would be needed to assess the viability of the hypothesis.

Bagshawe Glacier is a fast-flowing glacier terminating in an area of rapidly deepening bathymetry (Chapter 2). It is therefore conceivable that there is a region beyond the grounding line where the glacier is supported mechanically through the tensile strength of the ice. This would result in an "overhang" region between the grounding line and the terminus where the glacier base is not in contact with the bed. In the overhang region, gravitational forces could cause the glacier to slope slightly downwards towards the fjord, generating an area where positively buoyant water would be trapped from exiting towards the surface. Waters in this area would also be subject to input of sediment supplied at the grounding line, and might also be more energetic than the ambient ocean due to mechanical forcing by movement of the glacier. In such a case, meltwater would tend to pool up under the glacier, creating a repository of buoyant meltwater which may occasionally spill over or escape. As such, the meltwater supply could potentially be more episodic than what is the case for subglacial freswater discharge, and become intensified during calving or large movements of the glacier.

A meltwater source could also be generated without the requirement of a downward glacial slope. Ocean-driven melt below a large overhang region would flow out towards the ocean, accumulating more meltwater along the horizontal path and providing a localized source. This case would be somewhat analogous to the case below floating ice shelves (MacAyeal, 1985), but it is unclear whether an overhang of Bagshawe Glacier would be sufficiently long to provide a meltwater flux large enough to generate the observed mid-water plumes.

4.4.3 LESSONS FROM BUOYANT PLUME THEORY

The buoyant plume model (Jenkins, 2011) depends on the choices of depth, composition and magnitude of the initial volume flux. It contains four variables, which can be formulated in terms of terminal volume flux, plume width, temperature and salinity. We only have conclusive observational estimates of two of these six quantities, namely temperature and depth (or, equivalently, salinity). As such, the problem is underdetermined, and we are limited to evaluating the buoyant plume equations with a range of parameters and comparing the terminal plume properties with those of the most distinctly anomalous glacially modified waters observed during a near-glacier glider transect. We find the best correspondence to the observations at the core of the observed intrusion for a volume flux of $\sim$0.5 m^2 s^{-1} at outflow depth of $\sim$ 220 m. This is within the range of water depths observed near the terminus of Bagshawe Glacier. Varying the flux at this depth results in plume properties aligning reasonably well with the spread of the observations, suggesting that a varying discharge flux at fixed depth could generate the observed signal.

A key result of the buoyant plume analysis is that the predicted entrainment of ambient waters is relatively weak. Due to the relatively small freshwater content of the meltwater mixture released at depth, buoyancy forcing is weak compared to the case of subglacial freshwater discharge. As a result, the the entrainment rate along the plume, which is parameterized as proportional to the upwelling velocity, is comparatively small. The water injected at depth therefore constitutes a relatively large fraction of the plume waters at terminal level($\sim$20%). The large fraction of the retained meltwater mixture could explain the alignment of the observed temperature and salinity distribution with Gade lines intersecting with ambient water masses deeper in the water column.

Due to the limited velocities and the cold ambient waters, along-plume melt is small, and the plume process is unlikely to play a significant role in the mass balance of Bagshawe Glacier. This may be different in fjords further south along the wAP, where warm modified Upper Circumpolar Deep Water (mUCDW) is believed to penetrate into the fjords (Cook et al., 2016). The warming of deep waters in this area has been convincingly linked with ongoing large-scale mass loss from the Antarctic Peninsula Ice Sheet. Plume processes in the fjords in the central parts of the wAP could act to distribute heat from the warmer deep waters along a greater part of the glacier face, and thus act to increase the effects of deep ocean warming on glacial retreat. While this effect of buoyant plumes has been well-documented in Greenland fjords, further measurements near tidewater glaciers on the central wAP are necessary to further examine this possibility.

We have used the model formulation for a line plume geometry, thereby assuming an outflow along a length along the terminus. Since we have no knowledge of the source of the injected water or of the geometry at the grounding line, we do not know to what degree this is a valid approximation.

The buoyant plume model assumes a system in steady state. Since the nature of the release at depth is unknown, we cannot confidently justify this assumption. Both the tidal mechanism

proposed by (Domack and Ishman, 1993), and the alternative mechanism of trapping of buoyant water in overhang regions, would likely result in a variable volume flux. This introduces further uncertainty to the validity of the buoyant plume model in this environment, which could only be addressed analytically by using a more complex model with explicit time dependence.

Given the large uncertainties and the number of unknown parameters, the quantitative results of this analysis are broad estimates. However, the model does provide some valuable qualitative insights into the behavior of meltwater plumes in the environment. In particular, we note that the relatively weak buoyancy force acting on the initial meltwater mixture results in a slowly upwelling plume compared to environments with similar magnitude of freshwater discharge. Since entrainment and melt are both relatively weak, the outflowing plume retains the distinct water mass signature of ocean-driven melt, observable by a distinct alignment along Gade lines in $\theta - S$ space. The model thereby provides support for the release of meltwater at the bottom of the glacier terminus as a plausible mechanism for generating the observed mid-water intrusions.

4.4.4 PHYSICAL AND GEOCHEMICAL FLUXES

The melt generated by buoyant plumes is small, and therefore unlikely to have a significant impact on Bagshawe Glacier. However, plume generation impacts the ocean waters near the glaciers by acting as a source of neutrally buoyant, cold water at the terminal plume depth, and is likely responsible for the general mid-water cooling found in the inner fjord. This broad temperature minimum could result from buoyant plumes at the terminus through some combination of vertical spreading through diapycnal mixing and the influence of plumes with different terminal depths.

Strong buoyant plumes can drive circulation in fjords (Carroll et al., 2015), but without a better estimate of the volume flux at terminal level, we cannot determine whether this is the case in Andvord Bay. Ocean current records from moored ADCPs in inner Andvord Bay (Chapter 2) show no clear sign of a mid-depth outflow. Due to the high latitude and weak stratification, outflowing glacially modified waters may be deflected by rotation. Velocity observations closer to the western coast may therefore be necessary to locate the velocity signal associated with an outflowing plume.

Perhaps the most significant impact of buoyant glacial plumes is their potential role in vertical transport of various geochemical quantities. The increase in optical attenuation and backscatter within the mid-water intrusions suggest that plume waters are turbid compared to the ambient waters, and we have made the case that this anomaly is a result of upwelling of water from near the grounding line. As such, buoyant plumes act as a vertical "conveyor belt" for suspended eroded material from the grounding line to the upper mid-waters. The halocline prevents plumes from propagating into the surface layer, and most plumes are found below the phytoplankton layer. Downstream mixing mechanisms could potentially bring plume waters closer to the surface.

The high turbidity in the deep basin near Bagshawe Glacier suggests that the bulk of the sediment eroded by the glacier ends up in this deep basin. This is consistent with Domack and Ishman (1993), who proposed that gravity flows of sediment-laden water were the main mechanism of transport of sediment into the basin. Within the basins, we find elevated optical attenuation several hundred meters above the bottom. Given the low background flow in inner Andvord Bay (Chapter 2), resuspension of sediment by background flow is an unlikely mechanism for distributing sediment from the sea floor. Instead, we attribute the broad layer of elevated turbidity to a combination of turbulent detrainment of gravity flows, scouring and resuspension during calving events, and outflow of weak buoyant plumes. Beyond the deep basins, upwelling plumes are a likely transport mechanism of fine suspended sediment upwards in the water column, as evidenced by the mid-water turbidity signal. The subsequent down-fjord sediment transport depends on the downstream pathways of the plumes, which are currently not constrained by observations.

Due to the the upwelling of entrained ambient waters from below the euphotic zone, plume waters may act to transport nutrients upward in the water column. Meltwater of glacial origin has been linked to increased biological productivity along the wAP, likely as a result of their elevated nutrient content (Dierssen et al., 2002; Meredith et al., 2012). In addition to macronutrients, water masses originating near an active grounding line are likely to be a source of trace metals like iron, which are otherwise rare in the ocean around Antarctica (Wadley et al., 2014). The wAP coast have been proposed as a potentially important source of iron to offshore waters and sections of the Southern Ocean (Annett et al., 2017; Bown et al., 2017; Sherrell et al., 2018). Buoyant plumes could be a key mechanism for transporting iron from the deep waters of wAP fjords into shallower layers, from which it can more easily escape to the coastal ocean. Ongoing studies of the trace metal content of the distribution of nutrients and trace metals in Andvord Bay will reveal further details about the geochemical properties of glacial plumes.

Chapter 5
Conclusions

5.1 Summary

This dissertation has examined various aspects of the physical oceanography of Andvord Bay, a glacial fjord on the northern wAP. A large number of observations collected during three research cruises and from fixed oceanographic and meteorological sensors were used to characterize the physical environment of the fjord. The observations motivated further exploration of two processes of particular interest: the flushing of fjord waters during katabatic wind events, and the generation of mid-water intrusions by plume processes at the glacier-ocean interface. The following is a summary of the key outcomes of the study:

- Andvord Bay is located just north of the present influence of modified Upper Circumpolar Deep Water (mUCDW). While intrusions of mUCDW from the southern part of the Gerlache Strait were observed outside the fjord, this relatively warm water mass was not found within the fjord itself. As a result, the interior waters of the Andvord Bay were dominated by cold water masses originating in the Bransfield Strait.

- Upper ocean water masses were more variable, with temperatures varying by $>2.5^{\circ}$C in observations from different parts of the year. This variability is not unique to the fjord, and a similar temperature range is found in the broader coastal ocean. Stratification within the fjord is maintained well within the euphotic zone due to weak mean wind forcing. Upper ocean salinity decreases throughout the ice-free season as a result of glacier and/or sea ice melt. Due to the weak overall stratification in the fjord, the dynamics of the fjord are likely to be strongly influenced by rotation, and there is some evidence of an outflow of meltwater concentrated along the western coast.

- Glacier mass flux into Andvord Bay is dominated by the contribution from Bagshawe Glacier, a fast-flowing glacier located in the southwestern end of the fjord. Mass flux is dominated by the input of solid ice, which greatly exceeds the estimated contribution from freshwater runoff. The export of icebergs may be the main mechanism of export of freshwater and terrigenous material from the fjord.

- Andvord Bay is largely shielded from the prevailing alongshore winds, and is subject to weak tidal and buoyancy forcing. As a result, the fjord is dynamically quiet, with weak interior mixing and typical inner fjord ocean currents on the order of 1 cm s^{-1}. Conversely, the ocean environment outside the fjord is much more energetic, with stronger mean and tidal currents, higher temperature variability and strong diapycnal mixing associated with tidal flows through two narrow channels flanking the mouth of Andvord Bay. Low-frequency fluctuations of the Gerlache Current are likely to influence the interior waters of Andvord Bay, both by varying the water masses present outside the fjord, and possibly by exerting some degree of dynamical control over the weak mean circulation in the fjord.

- In stark contrast to the quiescent background state of Andvord Bay, the fjord occasionally experiences forceful katabatic winds blowing out of the fjord. Ocean observations during one katabatic event showed significant changes in the upper ocean, resulting in a persistent salinity increase. A series of numerical experiments suggest that strong down-fjord wind forcing episodes generate an energetic upper ocean response, strongly modified by rotation, and provides an efficient mechanism for flushing out the majority of the upper fjord waters. The model experiments further suggest that the effects are concentrated in the upper ocean, and that katabatic wind events are unlikely to drive substantial exchange of deep water in the fjord.

- A common feature of the inner reaches of Andvord Bay is the presence of mid-water intrusions of anomalously cold and turbid water masses. Such intrusions are typically found between 40 and 200 m depth, and decay in strength and frequency away from the terminus of Bagshawe Glacier. The signal is consistent with plume generation at the glacier terminus resulting from the input of buoyant water at depth, which generates a turbulent upwelling plume that settles at mid-water depth and flows out into the fjord. The temperature and salinity characteristics of an intrusion observed close to the glacier is consistent with a source of meltwater localized at 150 m to 250 m depth, and the associated turbidity anomaly suggests an origin at the glacier grounding line. In contrast to plumes generated by freshwater discharge, such meltwater plumes cannot efficiently penetrate the halocline, and therefore do not reach the surface. Due to the cold deep waters in Andvord Bay, the melt generated by the plumes is small, and the plume process is unlikely to significantly impact the mass balance of Bagshawe Glacier. Buoyant plumes may provide a key pathway for suspended sediment and geochemical quantities upwards from the grounding line and into the fjord.

5.2 DIRECTIONS FOR THE FUTURE

I hope that this dissertation can contribute to the understanding of fjord systems on the wAP, which is a region in rapid transition as a result of atmospheric and oceanic change. While ongoing

research is advancing our knowledge of the dynamics and interactions in the area, the current state of understanding of the wAP ocean as a whole, and of coastal oceanographic processes in particular, is in its infancy compared to comparable regions elsewhere. The study of the coastal wAP offers an opportunity to examine ongoing effects of oceanic and atmospheric changes, and to gain insight into the connections between ocean, ice, atmosphere, biology and geochemistry. Fjords play a key role in many of these complex interactions, and are therefore of particular interest. The work outlined in this dissertation has highlighted some key gaps in our current knowledge, which could be addressed in future studies. Some of these potential lines of research are outlined below:

- Oceanic heat transport of mUCDW is likely the main driver of glacier retreat along the wAP (Cook et al., 2016), and as a result a great research effort has gone into exploring the pathways of these warm water masses onto the continental shelf (e.g., Dinniman et al., 2011; Martinson and McKee, 2012; Moffat and Meredith, 2018). Less is known about the distribution of mUCDW along the coastal regions of the wAP, due in part to a lack of knowledge of the regional circulation. This study has shown how a bathymetric sill within the Gerlache Strait may prevent mUCDW-dominated deep waters from propagating onto the northern wAP. This highlights the need for improved knowledge of the regional circulation, obtained through observations or regional ocean models, in order to understand the mechanism shielding currently stable glaciers like those in Andvord Bay from the influence of ocean warming. Furthermore, coastal current variability is likely to impact circulation within wAP fjords, and an improved knowledge of the variability of the regional circulation may improve our knowledge of water exchange in fjords like Andvord Bay.

- The localization of glacially modified water masses within a short distance of the glacier shows the need for near-glacier measurements in accurately characterizing outflowing plumes. This in line with studies from Greenland fjords, which have shown that ocean properties change quickly away from the glacier terminus (Jackson et al., 2017). Due to the difficulty of conducting shipboard oceanographic measurements near glacier termini, the use of remotely operated or autonomous vehicles such as the ocean glider used in this study are a promising avenue for expanding our knowledge of near-glacier processes. Another potential source of measurements from this area is the instrumentation of marine mammals, a technique that has been employed successfully in oceanographic studies of the coastal wAP (Padman et al., 2010; Santini et al., 2018). This approach would require an assessment of the travel patterns of these animals in the inner parts of fjords.

- While near-glacier observations are difficult to obtain, further measurements further downstream from wAP glacier termini can also be highly useful. In particular, cross-fjord transects of temperature and salinity along with ocean velocity downstream of glacier termini could be used to estimate fluxes outward from the glacier, and to constrain models of processes occurring at the terminus. As shown in this dissertation, plumes can be highly

localized both vertically and horizontally, and observational approaches should focus on maintaining high spatial resolution.

- We currently have little empirical information about the subsurface geometry of wAP glacier termini. In the study of subsurface plumes in this dissertation, the grounding line depth was considered a free parameter within a wide range based on the adjacent ocean bathymetry. Further knowledge of the terminus geometry would help constrain the depth of the grounding line, and could also potentially be used as diagnostic tool of subglacial, which can generate cavities or other local ice geometry anomalies (Fried et al., 2015b; Slater et al., 2017). Successful subsurface surveys of glacier termini have previously been conducted using shipboard multibeam sonar (Rignot et al., 2015; Fried et al., 2015b) and remotely operated vehicles (Powell et al., 1996; Ashley and Smith, 2000).

- Due to the large-scale gradients in the offshore waters, there may be key differences in near-glacier processes along the wAP, which could result in wholly different circulation regimes in different fjords along the Peninsula. There is a pressing need for observational investigation of a greater range of fjords to understand the physical processes and their sensitivity to ongoing large-scale change. In particular, extending the study of wAP fjords to the regions further south would expand our understanding of the dependence of these systems on the ambient ocean temperature, and give important insights into what role ice-ocean interactions in fjords play in the fate of the Antarctic Peninsula Ice Sheet.

- Warming of the ocean and the atmosphere both have the potential to change Andvord Bay from its present state, although their respective effects may be different is some key respects. In a future scenario where ocean warming dominates, fjords like Andvord Bay may begin to experience the kind of ocean-driven glacier retreat seen further south along the wAP, where air temperatures are colder but mUCDW dominates the offshore water. In an alternative scenario dominated by atmospheric warming, northern wAP fjords could instead begin to resemble their counterparts in the South Shetland Island (SSI), where the atmospheric climate is milder but the offshore subsurface ocean is relatively cold (e.g., Wilson et al., 1999; Stastna, 2010). Surface glacier melt is a major contributor to the surface mass balance of SSI glaciers, and likely also the driver of glacier mass loss in this more temperature region (Simões et al., 1999/ed; Lee et al., 2008). As a result, SSI fjords and bays experience substantial freshwater input, with consequent impacts on surface salinity and ocean turbidity (Klöser et al., 1994; Yoon et al., 1998; Schloss et al., 2012).

  The details of the ongoing changes in the atmospheric and marine climate of the wAP are complex, as evidenced by the recent stagnation or reversal of the atmospheric warming trend in the region (Carrasco, 2013; Oliva et al., 2017; Gonzalez and Fortuny, 2018). Drivers of atmospheric variability on the Antarctic Peninsula include local changes in wind and sea-ice cover in the Weddell Sea (Turner et al., 2016), large-scale changes in the Southern Annular Mode (Marshall et al., 2006) and teleconnections to remote areas such as the North

Atlantic (Li et al., 2014) and the Western Tropical Pacific (Clem and Fogt, 2013). Likewise, the mechanisms responsible for ocean warming along the wAP depend on both large-scale dynamical shifts in the Antarctic Circumpolar Current (e.g., Gille et al., 2016; Palóczy et al., 2018) and details of cross-shelf heat transport occurring on the wAP shelf (e.g., Moffat and Meredith, 2018). As a result of the complexity of the system, the evolution of the climate of the northern wAP is difficult to predict. Future research on the connections between the wAP and global atmosphere and ocean dynamics may therefore help improve our projections of how northern wAP fjords like Andvord Bay may change in the coming decade, and whether such changes are likely to be driven by the ocean or by the atmosphere.

Appendix A

Supplementary material for Chapter 2

This appendix contains a description of the methodology used to generate qualitative time series of sea ice cover from time lapse photographs. It also contains 6 figures which show a more detailed view of FjordEco datasets, or illustrations of analysis referred to in Chapter 2.

Qualitative sea ice estimates

Sea ice cover was estimated visually from each camera site. For each camera, one image per day was selected (near local noon) for the entire period of measurements. For each photograph, the sea ice cover fraction was classified as either *0, 1/3, 2/3 or 1* based on what was estimated to be the best approximate representation of the sea ice cover observed in the image. Instances where the sight was limited due to heavy weather or snow buildup in front of the camera were not included.

To the degree possible, assessment was made based on the amount of ice of oceanic origin. Large bergs and growlers, bergy bits and other ice of glacial origin were excluded, and the estimates were based on the amount of flat, plate-like ice. Making this separation based on photographs is typically non-trivial, and there are likely significant errors associated with the visual estimates.

Estimates were made based on what is immediately visible in the image. The estimate was intended to represent the entire visible ocean area, however there is likely a bias towards the region near the location of the camera due to the low angle.

Images within each dataset were classified in random order in order to minimize bias. Each dataset was processed twice in order to assess the stability of the method. The number of processed photographs (excluding those during poor visibility), and the fraction of these where the two estimates agree is shown below:

- **Inner fjord**: Same: *171/202 (85%)*, within 1/3: *202/202 (100%)*.
- **Middle fjord**: Same: *266/310 (86%)*, within 1/3: *309/310 (100%)*.

(a) Inner fjord, April 18th, 2016 (the *Palmer* on the right).

(b) Outer fjord, April 18th, 2016.

(c) Outer fjord, October 22, 2016.

Figure A.1: Example photographs from AWS A time lapse cameras. Assigned sea ice cover values: 0 *(a, b)*, 1 *(c)*.

The method clearly has its limitations. It is not intended as a quantitative measure of sea ice cover, but does appear to be relatively self-consistent and gives some idea of the time variability of ice cover in the fjord in a broad sense.

SUPPLEMENTARY FIGURES

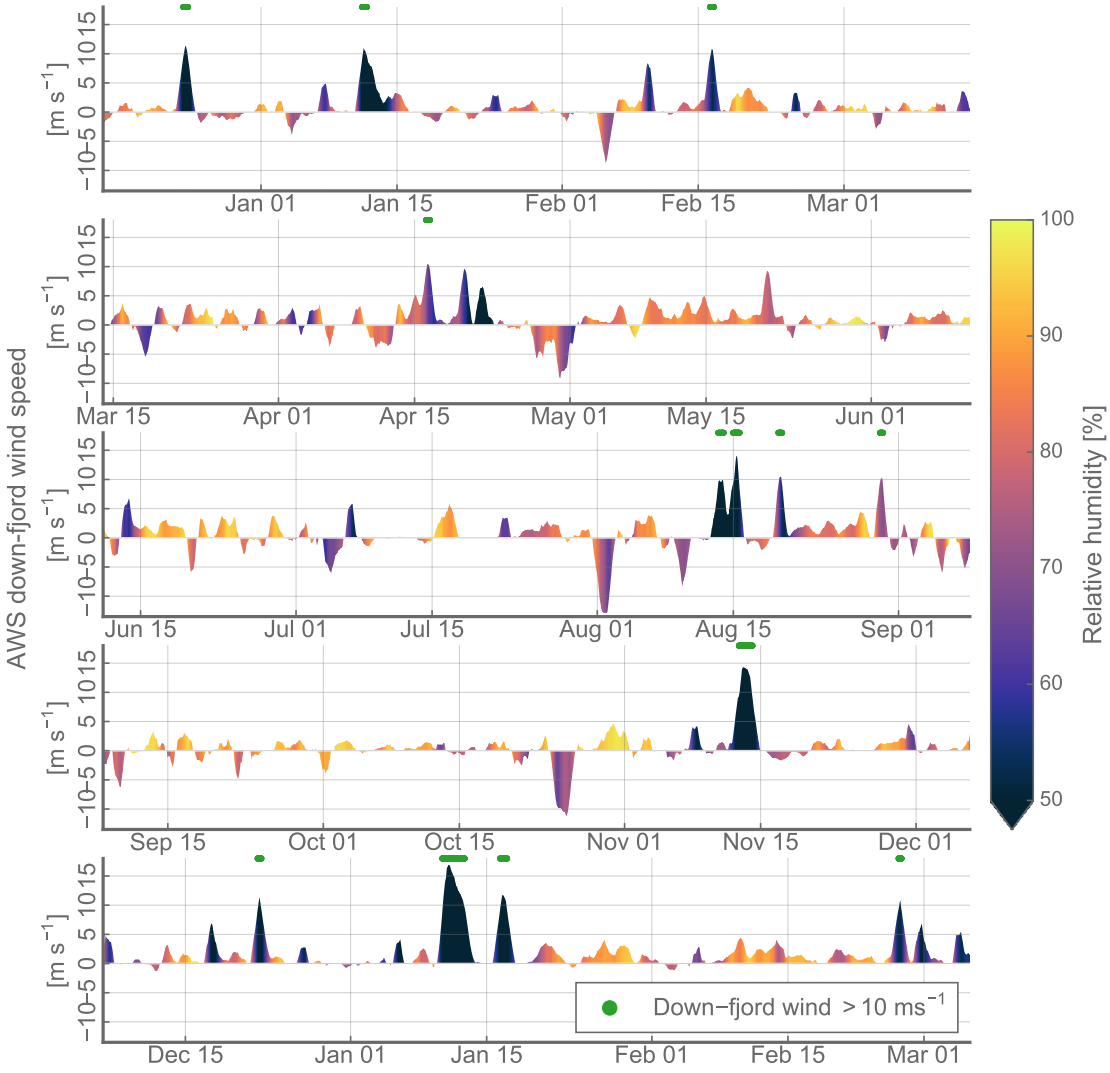

Figure A.2: Time series of down-fjord winds (defined as positive 60° CW of North) and relative humidity from the AWS B record. Measurement time: December 15 2015 to March 5 2017. Smoothed with a 24-hour boxcar window.

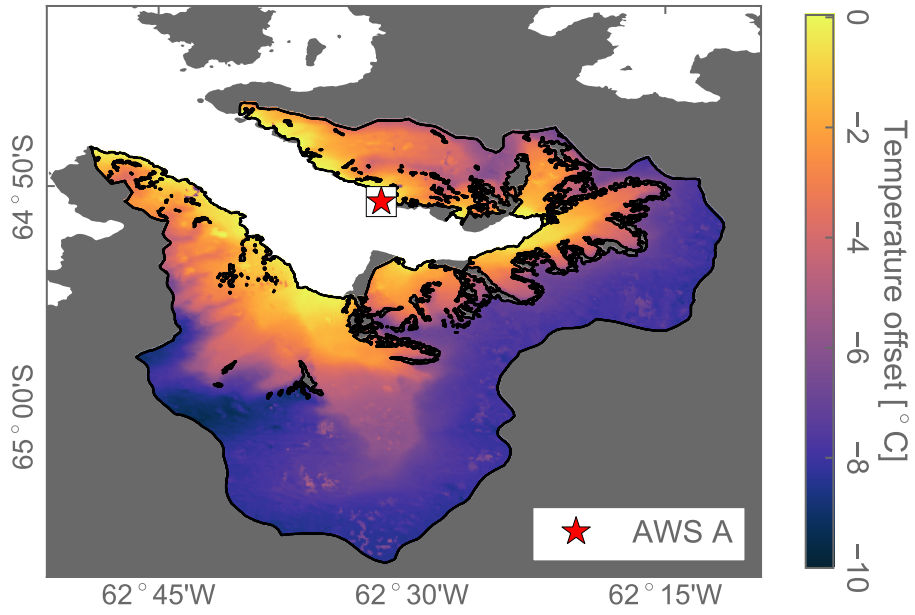

Figure A.3: Temperature offset used to compute PDD over the Andvord Bay catchment areas. Catchment areas of glaciers terminating in Andvord Bay, from Cook et al. (2014). Colors show temperature anomaly relative to *AWS A* using a fixed lapse rate of -0.0044°C m^{-1} and topography obtained from the Global Multi-Resolution Topography Data Synthesis (Ryan et al., 2009).

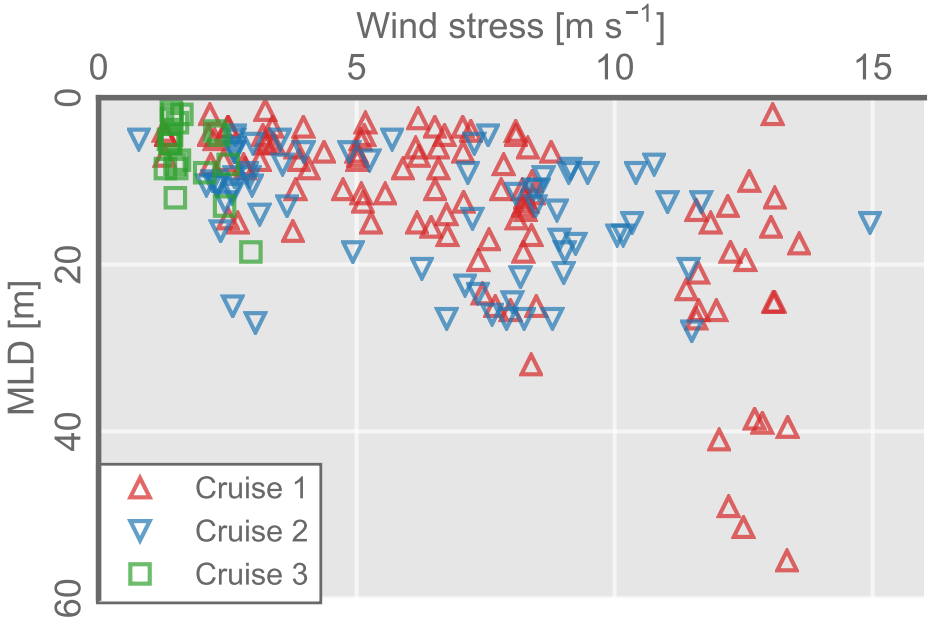

Figure A.4: Mixed layer depths computed from all FjordEco CTDs in Andvord Bay as a function of average winds measured by the ship system over 24 hours leading up to the measurement (excluding wind measurements outside the fjord). Mixed layer depth was taken as the shallowest depth at which potential density increased beyond 0.02 kg m^{-3} of the minimum.

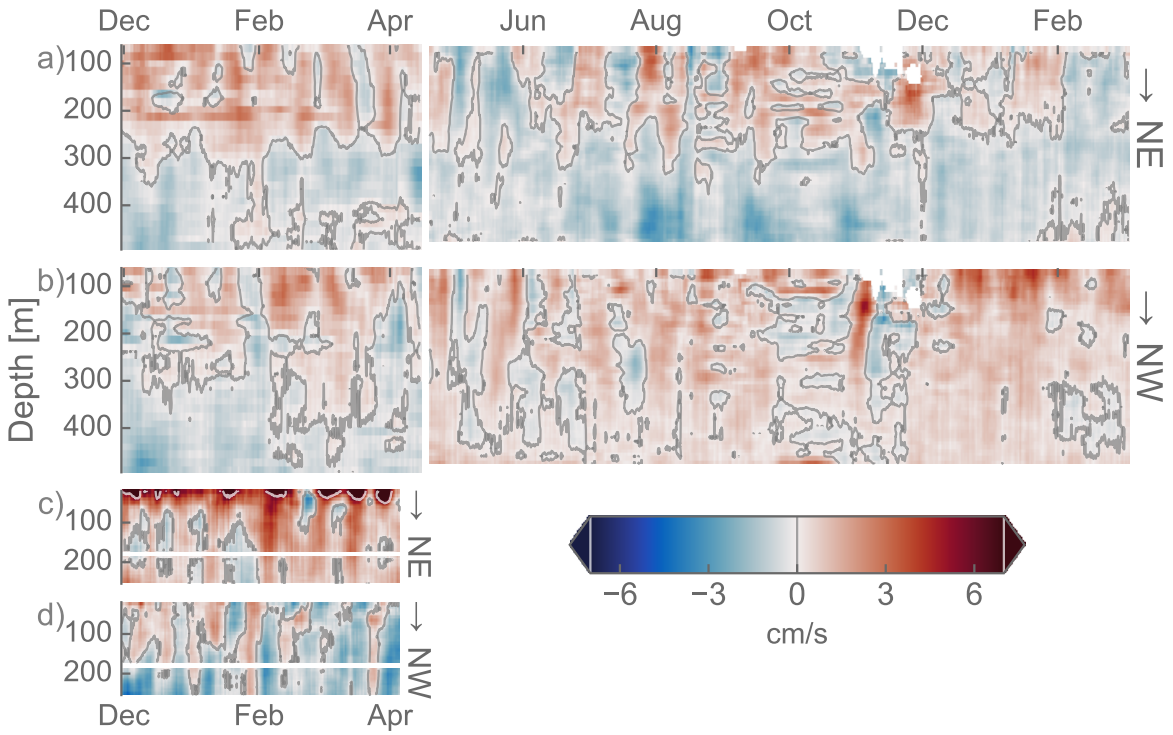

Figure A.5: Current components from Mooring A *(a, b)* and Mooring B *(c, d)* between November 2015 and April 2017. Panels *a, c* show the current component towards the NE corresponding approximately to the along-strait direction. Panels *b, d* show the current component towards the NW corresponding approximately to the along-fjord direction. Smoothed with a week-long boxcar window in time. Capped at ± 6 cm s^{-1} for emphasis.

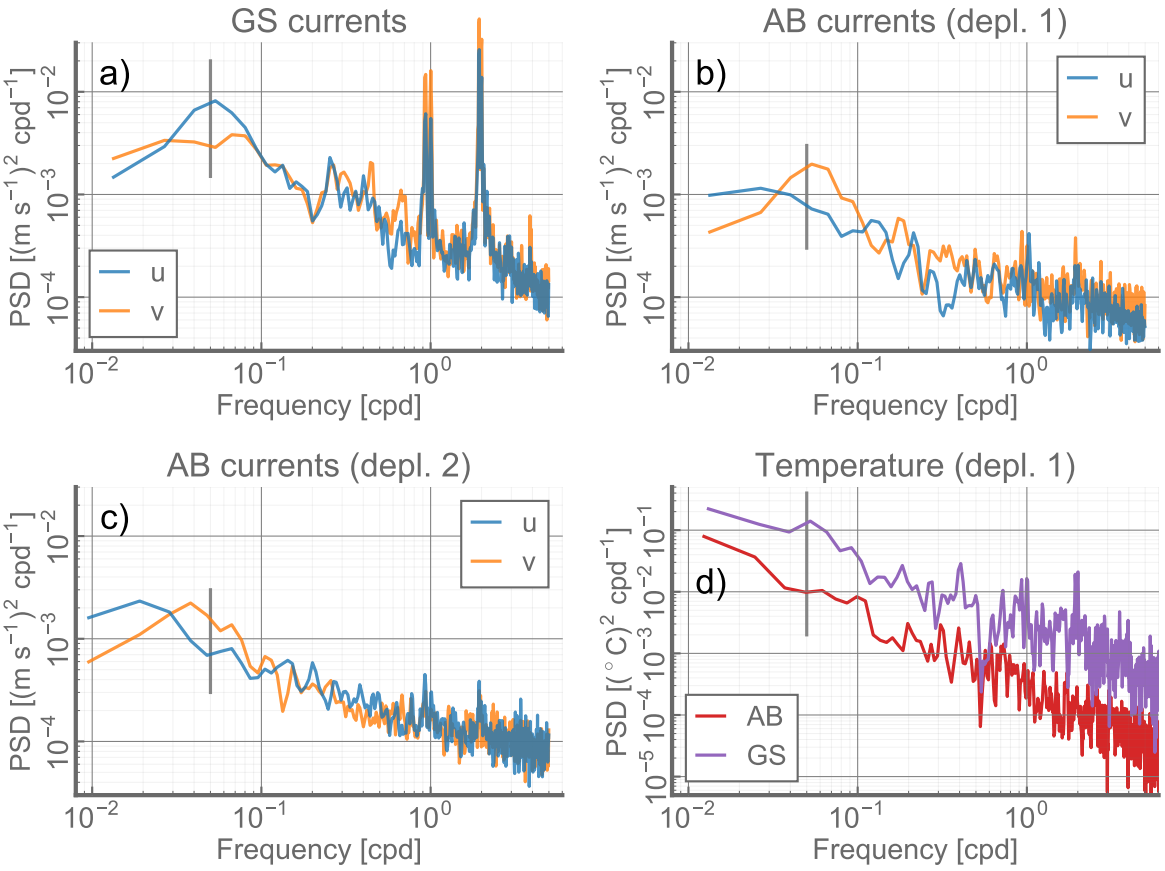

Figure A.6: Power spectra from FjordEco moored records. *a)* Depth average spectra of velocity components (u: eastward, v: northward) between 100 and 200 m from ADCP records at Mooring B in the Gerlache Strait. *b, c)* Depth average spectra of velocity components from the same depth range from *Mooring A* in Andvord Bay during deployments 1 (*b*) and 2 (*c*). *d)* Temperature spectra from moored sensors at *Mooring B* (209 m depth) and 4 *Mooring A* (199 m depth) during the first deployment. Spectra obtained by computing Fast Fourier Transforms in n windows overlapping in time by 66%, where $n = 3$ for deployment 1 and $n = 7$ for deployment 2. Velocity spectra are averaged over the depth range. Smaller gray vertical lines show the frequency (20 days)$^{-1}$. *Date ranges*: Deployment 1: 30 November 2015 to 4 April 2016. Deployment 2: 20 April 2016 to 4 March 2017.

Appendix B

Supplementary material for Chapter 3

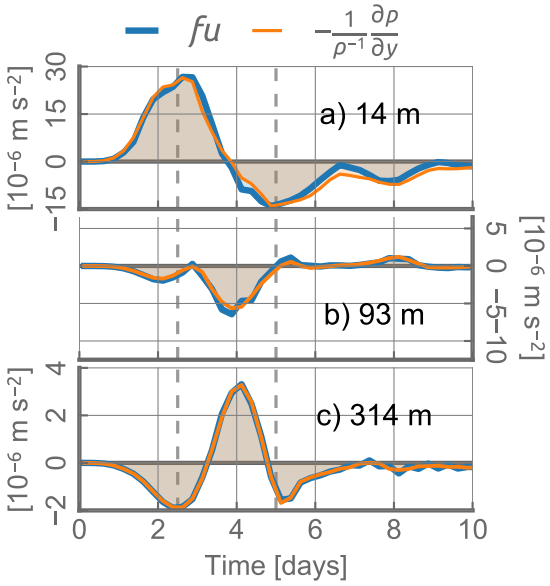

Figure B.1: Dominant terms of the cross-fjord momentum balance in Main Scenario experiment at select depths: Coriolis (blue) and pressure gradient (orange) terms. Averaged from $y = 9$ km to $y = 11$ km and from $x = 20$ km to $x = 30$ km.

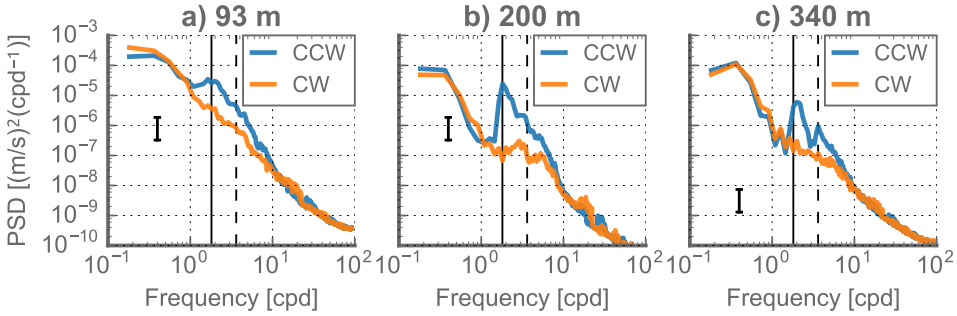

Figure B.2: Zonally averaged rotary frequency spectra of complex velocity time series $u(t) + iv(t)$ in the middle of model the fjord ($y = 12.5$ km, $x \in [25\text{ km}, 35\text{ km}]$) at three different depths in the the Main Scenario experiment. Blue lines show the counter-clockwise rotating component, orange lines show the clockwise. At each point, fast Fourier transforms are calculated over $N = 4$ segments of 5.5 day each, overlapping by 50%. Error bars show the confidence interval assuming $2N = 8$ degrees of freedom, a conservative estimate. The solid and dashed gray lines show f (the local inertial frequency) and $2f$, respectively.

Bibliography

Alford, M. H., J. A. MacKinnon, H. L. Simmons, and J. D. Nash, 2016: Near-Inertial Internal Gravity Waves in the Ocean. *Annual Review of Marine Science*, **8 (1)**, 95–123, doi:10.1146/annurev-marine-010814-015746.

Allen, G. L., and J. H. Simpson, 1998: Reflection of the Internal Tide in Upper Loch Linnhe, a Scottish Fjord. *Estuarine, Coastal and Shelf Science*, **46 (5)**, 683–701, doi:10.1006/ecss.1997.0308.

Anderson, J. J., and A. H. Devol, 1987: Extent and intensity of the anoxic zone in basins and fjords. *Deep Sea Research Part A. Oceanographic Research Papers*, **34 (5)**, 927–944, doi:10.1016/0198-0149(87)90046-X.

Annett, A. L., J. N. Fitzsimmons, M. J. M. Séguret, M. Lagerström, M. P. Meredith, O. Schofield, and R. M. Sherrell, 2017: Controls on dissolved and particulate iron distributions in surface waters of the Western Antarctic Peninsula shelf. *Marine Chemistry*, **196**, 81–97, doi:10.1016/j.marchem.2017.06.004.

Arendt, K. E., J. Dutz, S. H. Jónasdóttir, S. Jung-Madsen, J. Mortensen, E. F. Møller, and T. G. Nielsen, 2011: Effects of suspended sediments on copepods feeding in a glacial influenced sub-Arctic fjord. *Journal of Plankton Research*, **33 (10)**, 1526–1537, doi:10.1093/plankt/fbr054.

Argentini, S., A. P. Viola, G. Mastrantonio, A. Maurizi, T. Georgiadis, and M. Nardino, 2003: Characteristics of the boundary layerat Ny-Ålesund in the Arctic during the ARTIST field experiment. *Annals of Geophysics*, **46 (2)**, doi:10.4401/ag-3414.

Arneborg, L., C. Janzen, B. Liljebladh, T. P. Rippeth, J. H. Simpson, and A. Stigebrandt, 2004: Spatial Variability of Diapycnal Mixing and Turbulent Dissipation Rates in a Stagnant Fjord Basin. *Journal of Physical Oceanography*, **34 (7)**, 1679–1691, doi:10.1175/1520-0485(2004)034<1679:SVODMA>2.0.CO;2.

Arneborg, L., and B. Liljebladh, 2001: The Internal Seiches in Gullmar Fjord. Part I: Dynamics. *Journal of Physical Oceanography*, **31 (9)**, 2549–2566, doi:10.1175/1520-0485(2001)031<2549:TISIGF>2.0.CO;2.

Ashley, G. M., and N. D. Smith, 2000: Marine sedimentation at a calving glacier margin. *GSA Bulletin*, **112 (5)**, 657–667, doi:10.1130/0016-7606(2000)112<657:MSAACG>2.0.CO;2.

Austin, J., 2013: Observations of near-inertial energy in Lake Superior. *Limnology and Oceanography*, **58 (2)**, 715–728, doi:10.4319/lo.2013.58.2.0715.

Azetsu-Scott, K., and J. P. M. Syvitski, 1999: Influence of melting icebergs on distribution, characteristics and transport of marine particles in an East Greenland fjord. *Journal of Geophysical Research: Oceans*, **104 (C3)**, 5321–5328, doi:10.1029/1998JC900083.

Azetsu-Scott, K., and F. C. Tan, 1997: Oxygen isotope studies from Iceland to an East Greenland Fjord: Behaviour of glacial meltwater plume. *Marine Chemistry*, **56 (3)**, 239–251, doi:10.1016/S0304-4203(96)00078-3.

Ball, F. K., 1957: The Katabatic Winds of Adélie Land and King George V Land. *Tellus*, **9 (2)**, 201–208, doi:10.1111/j.2153-3490.1957.tb01874.x.

Barnes, D. K. A., V. Fuentes, A. Clarke, I. R. Schloss, and M. I. Wallace, 2006: Spatial and temporal variation in shallow seawater temperatures around Antarctica. *Deep Sea Research Part II: Topical Studies in Oceanography*, **53 (8)**, 853–865, doi:10.1016/j.dsr2.2006.03.008.

Bartholomaus, T. C., C. F. Larsen, and S. O'Neel, 2013: Does calving matter? Evidence for significant submarine melt. *Earth and Planetary Science Letters*, **380**, 21–30, doi:10.1016/j.epsl.2013.08.014.

Beaird, N., F. Straneo, and W. Jenkins, 2015: Spreading of Greenland meltwaters in the ocean revealed by noble gases. *Geophysical Research Letters*, **42 (18)**, 7705–7713, doi:10.1002/2015GL065003.

Beardsley, R. C., R. Limeburner, and W. B. Owens, 2004: Drifter measurements of surface currents near Marguerite Bay on the western Antarctic Peninsula shelf during austral summer and fall, 2001 and 2002. *Deep Sea Research Part II: Topical Studies in Oceanography*, **51 (17–19)**, 1947–1964, doi:10.1016/j.dsr2.2004.07.031.

Bindschadler, R., and Coauthors, 2008: The Landsat Image Mosaic of Antarctica. *Remote Sensing of Environment*, **112 (12)**, 4214–4226, doi:10.1016/j.rse.2008.07.006.

Bown, J., P. Laan, S. Ossebaar, K. Bakker, P. Rozema, and H. J. W. de Baar, 2017: Bioactive trace metal time series during Austral summer in Ryder Bay, Western Antarctic Peninsula. *Deep Sea Research Part II: Topical Studies in Oceanography*, **139**, 103–119, doi:10.1016/j.dsr2.2016.07.004.

Braithwaite, R. J., and O. B. Olesen, 1989: Calculation of Glacier Ablation from Air Temperature, West Greenland. *Glacier Fluctuations and Climatic Change*, Glaciology and Quaternary Geology, Springer, Dordrecht, 219–233, doi:10.1007/978-94-015-7823-3_15.

Carbotte, S., W. B. F. Ryan, S. O'Hara, R. Arko, A. Goodwillie, A. Melkonian, R. Weissel, and V. Ferrini, 2007: Antarctic Multibeam Bathymetry and Geophysical Data Synthesis: An on-line digital data Resource for marine geoscience research in the Southern Ocean. USGS Numbered Series 2007-1047-SRP-002, U.S. Geological Survey, Reston, VA.

Carrasco, J. F., 2013: Decadal Changes in the Near-Surface Air Temperature in the Western Side of the Antarctic Peninsula. *Atmospheric and Climate Sciences*, **03**, 275, doi:10.4236/acs.2013.33029.

Carroll, D., D. A. Sutherland, E. L. Shroyer, J. D. Nash, G. A. Catania, and L. A. Stearns, 2015: Modeling Turbulent Subglacial Meltwater Plumes: Implications for Fjord-Scale Buoyancy-Driven Circulation. *Journal of Physical Oceanography*, **45 (8)**, 2169–2185, doi:10.1175/JPO-D-15-0033.1.

Carroll, D., D. A. Sutherland, E. L. Shroyer, J. D. Nash, G. A. Catania, and L. A. Stearns, 2017: Subglacial discharge-driven renewal of tidewater glacier fjords. *Journal of Geophysical Research: Oceans*, **122 (8)**, 6611–6629, doi:10.1002/2017JC012962.

Carter, L., I. N. McCave, and M. J. M. Williams, 2008: Chapter 4 Circulation and Water Masses of the Southern Ocean: A Review. *Developments in Earth and Environmental Sciences*, F. F. a. M. Siegert, Ed., Antarctic Climate Evolution, Vol. 8, Elsevier, 85–114, doi:10.1016/S1571-9197(08)00004-9.

Carter, S. P., and H. A. Fricker, 2012/ed: The supply of subglacial meltwater to the grounding line of the Siple Coast, West Antarctica. *Annals of Glaciology*, **53 (60)**, 267–280, doi:10.3189/2012AoG60A119.

Chant, R. J., 2001: Evolution of Near-Inertial Waves during an Upwelling Event on the New Jersey Inner Shelf. *Journal of Physical Oceanography*, **31 (3)**, 746–764, doi:10.1175/1520-0485(2001)031<0746:EONIWD>2.0.CO;2.

Chen, S.-N., and L. P. Sanford, 2009: Axial Wind Effects on Stratification and Longitudinal Salt Transport in an Idealized, Partially Mixed Estuary. *Journal of Physical Oceanography*, **39 (8)**, 1905–1920, doi:10.1175/2009JPO4016.1.

Chu, V. W., 2014: Greenland ice sheet hydrology: A review. *Progress in Physical Geography*, **38 (1)**, 19–54, doi:10.1177/0309133313507075.

Clarke, A., M. P. Meredith, M. I. Wallace, M. A. Brandon, and D. N. Thomas, 2008: Seasonal and interannual variability in temperature, chlorophyll and macronutrients in northern Marguerite Bay, Antarctica. *Deep Sea Research Part II: Topical Studies in Oceanography*, **55 (18)**, 1988–2006, doi:10.1016/j.dsr2.2008.04.035.

Clarke, A., E. J. Murphy, M. P. Meredith, J. C. King, L. S. Peck, D. K. A. Barnes, and R. C. Smith, 2007: Climate change and the marine ecosystem of the western Antarctic Peninsula. *Philosophical Transactions of the Royal Society of London B: Biological Sciences*, **362 (1477)**, 149–166, doi:10.1098/rstb.2006.1958.

Clem, K. R., and R. L. Fogt, 2013: Varying roles of ENSO and SAM on the Antarctic Peninsula climate in austral spring. *Journal of Geophysical Research: Atmospheres*, **118 (20)**, 11,481–11,492, doi:10.1002/jgrd.50860.

Cook, A. J., P. R. Holland, M. P. Meredith, Murray, T., Luckman, A., and Vaughan, D.G, 2016: Ocean forcing of glacier retreat in the western Antarctic Peninsula. *Science*, **353 (6296)**, 283–286, doi:http://dx.doi.org/10.1126/science.aae0017.

Cook, A. J., D. G. Vaughan, A. J. Luckman, and T. Murray, 2014: A new Antarctic Peninsula glacier basin inventory and observed area changes since the 1940s. *Antarctic Science*, **26 (6)**, 614–624, doi:10.1017/S0954102014000200.

Costa, D. P., J. M. Klinck, E. E. Hofmann, M. S. Dinniman, and J. M. Burns, 2008: Upper ocean variability in west Antarctic Peninsula continental shelf waters as measured using instrumented seals. *Deep Sea Research Part II: Topical Studies in Oceanography*, **55 (3–4)**, 323–337, doi:10.1016/j.dsr2.2007.11.003.

Cottier, F. R., F. Nilsen, R. Skogseth, V. Tverberg, J. Skarðhamar, and H. Svendsen, 2010: Arctic fjords: A review of the oceanographic environment and dominant physical processes. *Geological Society, London, Special Publications*, **344 (1)**, 35–50, doi:10.1144/SP344.4.

Cottier, F. R., V. Tverberg, M. Inall, H. Svendsen, F. Nilsen, and C. Griffiths, 2005: Water mass modification in an Arctic fjord through cross-shelf exchange: The seasonal hydrography of Kongsfjorden, Svalbard. *Journal of Geophysical Research: Oceans*, **110 (C12)**, C12 005, doi:10.1029/2004JC002757.

Cowan, E. A., and R. D. Powell, 1990: Suspended sediment transport and deposition of cyclically interlaminated sediment in a temperate glacial fjord, Alaska, U.S.A. *Geological Society, London, Special Publications*, **53 (1)**, 75–89, doi:10.1144/GSL.SP.1990.053.01.04.

Cowton, T., D. Slater, A. Sole, D. Goldberg, and P. Nienow, 2015: Modeling the impact of glacial runoff on fjord circulation and submarine melt rate using a new subgrid-scale parameterization for glacial plumes. *Journal of Geophysical Research: Oceans*, **120 (2)**, 796–812, doi:10.1002/2014JC010324.

Cushman-Roisin, B., L. Asplin, and H. Svendsen, 1994: Upwelling in broad fjords. *Continental Shelf Research*, **14 (15)**, 1701–1721, doi:10.1016/0278-4343(94)90044-2.

Dierssen, H. M., R. C. Smith, and M. Vernet, 2002: Glacial meltwater dynamics in coastal waters west of the Antarctic peninsula. *Proceedings of the National Academy of Sciences of the United States of America*, **99 (4)**, 1790–1795, doi:10.1073/pnas.032206999.

Dinniman, M. S., J. M. Klinck, and W. O. Smith Jr., 2011: A model study of Circumpolar Deep Water on the West Antarctic Peninsula and Ross Sea continental shelves. *Deep Sea Research Part II: Topical Studies in Oceanography*, **58 (13–16)**, 1508–1523, doi:10.1016/j.dsr2.2010.11.013.

Domack, E. W., and S. Ishman, 1993: Oceanographic and physiographic controls on modern sedimentation within Antarctic fjords. *Geological Society of America Bulletin*, **105 (9)**, 1175–1189, doi:10.1130/0016-7606(1993)105<1175:OAPCOM>2.3.CO;2.

Domack, E. W., and C. R. Williams, 1990: Fine Structure and Suspended Sediment Transport in Three Antarctic Fjords. *Contributions to Antarctic Research I*, C. R. Bentley, Ed., American Geophysical Union, 71–89.

Ducklow, H. W., and Coauthors, 2007: Marine pelagic ecosystems: The West Antarctic Peninsula. *Philosophical Transactions of the Royal Society of London B: Biological Sciences*, **362 (1477)**, 67–94, doi:10.1098/rstb.2006.1955.

Duprat, L. P. A. M., G. R. Bigg, and D. J. Wilton, 2016: Enhanced Southern Ocean marine productivity due to fertilization by giant icebergs. *Nature Geoscience*, **9 (3)**, 219–221, doi:10.1038/ngeo2633.

Fahnestock, M., T. Scambos, T. Moon, A. Gardner, T. Haran, and M. Klinger, 2016: Rapid large-area mapping of ice flow using Landsat 8. *Remote Sensing of Environment*, **185**, 84–94, doi:10.1016/j.rse.2015.11.023.

Farmer, D. M., 1976: The Influence of Wind on the Surface Layer of a Stratified Inlet: Part II. Analysis. *Journal of Physical Oceanography*, **6 (6)**, 941–952, doi:10.1175/1520-0485(1976)006<0941:TIOWOT>2.0.CO;2.

Farmer, D. M., and T. R. Osborn, 1976: The Influence of Wind on the Surface Layer of a Stratified Inlet: Part I. Observations. *Journal of Physical Oceanography*, **6 (6)**, 931–940, doi:10.1175/1520-0485(1976)006<0931:TIOWOT>2.0.CO;2.

Fer, I., 2006: Scaling turbulent dissipation in an Arctic fjord. *Deep Sea Research Part II: Topical Studies in Oceanography*, **53 (1–2)**, 77–95, doi:10.1016/j.dsr2.2006.01.003.

Fer, I., R. Skogseth, and P. M. Haugan, 2004: Mixing of the Storfjorden overflow (Svalbard Archipelago) inferred from density overturns. *Journal of Geophysical Research: Oceans*, **109 (C1)**, C01 005, doi:10.1029/2003JC001968.

Fer, I., and K. Widell, 2007: Early spring turbulent mixing in an ice-covered Arctic fjord during transition to melting. *Continental Shelf Research*, **27 (15)**, 1980–1999, doi:10.1016/j.csr.2007.04.003.

Fried, M. J., and Coauthors, 2015a: Distributed subglacial discharge drives significant submarine melt at a Greenland tidewater glacier. *Geophysical Research Letters*, **42 (21)**, 9328–9336, doi:10.1002/2015GL065806.

Fried, M. J., and Coauthors, 2015b: Distributed subglacial discharge drives significant submarine melt at a Greenland tidewater glacier. *Geophysical Research Letters*, **42 (21)**, 9328–9336, doi:10.1002/2015GL065806.

Fujino, K., E. L. Lewis, and R. G. Perkin, 1974: The freezing point of seawater at pressures up to 100 bars. *Journal of Geophysical Research*, **79 (12)**, 1792–1797, doi:10.1029/JC079i012p01792.

Gade, H. G., 1979: Melting of Ice in Sea Water: A Primitive Model with Application to the Antarctic Ice Shelf and Icebergs. *Journal of Physical Oceanography*, **9 (1)**, 189–198, doi:10.1175/1520-0485(1979)009<0189:MOIISW>2.0.CO;2.

Garcıá, M. A., C. G. Castro, A. F. Rıós, M. D. Doval, G. Rosón, D. Gomis, and O. López, 2002: Water masses and distribution of physico-chemical properties in the Western Bransfield Strait and Gerlache Strait during Austral summer 1995/96. *Deep Sea Research Part II: Topical Studies in Oceanography*, **49 (4–5)**, 585–602, doi:10.1016/S0967-0645(01)00113-8.

Garibotti, I. A., M. Vernet, M. E. Ferrario, R. C. Smith, R. M. Ross, and L. B. Quetin, 2003: Phytoplankton spatial distribution patterns along the western Antarctic Peninsula (Southern Ocean). *Marine Ecology Progress Series*, **261**, 21–39.

Geyer, W. R., 1997: Influence of Wind on Dynamics and Flushing of Shallow Estuaries. *Estuarine, Coastal and Shelf Science*, **44 (6)**, 713–722, doi:10.1006/ecss.1996.0140.

Geyer, W. R., and D. Ralston, 2011: Geyer, W. R., and D. K. Ralston. "2.03—The dynamics of strongly stratified estuaries. *Treatise on Estuarine and Coastal Science. Amsterdam: Elsevier*, 37–52.

Gilbert, R., 1990: Rafting in glacimarine environments. *Geological Society, London, Special Publications*, **53 (1)**, 105–120, doi:10.1144/GSL.SP.1990.053.01.06.

Gill, A. E., 1982: *Ocean-Atmosphere Dynamics*. 1st ed., No. 30, International Geophysics Series, Elsevier.

Gille, S. T., D. C. McKee, and D. G. Martinson, 2016: Temporal Changes in the Antarctic Circumpolar Current: IMPLICATIONS FOR THE ANTARCTIC CONTINENTAL SHELVES. *Oceanography*, **29 (4)**, 96–105.

Gonzalez, S., and D. Fortuny, 2018: How robust are the temperature trends on the Antarctic Peninsula? *Antarctic Science*, **30 (5)**, 322–328, doi:10.1017/S0954102018000251.

Grange, L. J., and C. R. Smith, 2013: Megafaunal Communities in Rapidly Warming Fjords along the West Antarctic Peninsula: Hotspots of Abundance and Beta Diversity. *PLoS ONE*, **8 (12)**, doi:10.1371/journal.pone.0077917.

Gray, L., I. Joughin, S. Tulaczyk, V. B. Spikes, R. Bindschadler, and K. Jezek, 2005: Evidence for subglacial water transport in the West Antarctic Ice Sheet through three-dimensional satellite radar interferometry. *Geophysical Research Letters*, **32 (3)**, doi:10.1029/2004GL021387.

Gregg, M. C., D. P. Winkel, J. A. MacKinnon, and R.-C. Lien, 1999: Mixing over Shelves and Slopes. *Dynamics of oceanic internal gravity waves II, Proceedings, Hawaiian Winter Workshop*.

Griffies, S. M., and R. W. Hallberg, 2000: Biharmonic Friction with a Smagorinsky-Like Viscosity for Use in Large-Scale Eddy-Permitting Ocean Models. *Monthly Weather Review*, **128 (8)**, 2935–2946, doi:10.1175/1520-0493(2000)128<2935:BFWASL>2.0.CO;2.

Hagen, J. O., J. Kohler, K. Melvold, and J.-G. Winther, 2003: Glaciers in Svalbard: Mass balance, runoff and freshwater flux. *Polar Research*, **22 (2)**, 145–159, doi:10.1111/j.1751-8369.2003.tb00104.x.

Hansen, D. V., and J. Rattray, 1966: Gravitational Circulation in Straits and Estuaries. *Journal of Marine Research*, **23**.

Hawley, N., 2004: Response of the benthic nepheloid layer to near-inertial internal waves in southern Lake Michigan. *Journal of Geophysical Research: Oceans*, **109 (C4)**, C04 007, doi:10.1029/2003JC002128.

Hofmann, E. E., and J. M. Klinck, 1998: Hydrography and circulation of the Antarctic continental shelf: 150 E eastward to the Greenwich Meridian. *The Sea, The Global Coastal Ocean, Regional Studies and Synthesis*, 11, John Wiley & Sons, Inc, 997–1047.

Hofmann, E. E., J. M. Klinck, C. M. Lascara, and D. A. Smith, 1996: Water Mass Distribution and Circulation West of the Antarctic Peninsula And Including Bransfield Strait. *Foundations for Ecological Research West of the Antarctic Peninsula*, R. M. Ross, E. E. Hofmann, and L. B. Quetin, Eds., American Geophysical Union, 61–80.

Hopwood, M. J., D. P. Connelly, K. E. Arendt, T. Juul-Pedersen, M. C. Stinchcombe, L. Meire, M. Esposito, and R. Krishna, 2016: Seasonal Changes in Fe along a Glaciated Greenlandic Fjord. *Frontiers in Earth Science*, **4**, doi:10.3389/feart.2016.00015.

Huntley, M. E., and P. P. Niiler, 1995: Physical control of population dynamics in the Southern Ocean. *ICES Journal of Marine Science*, **52 (3-4)**, 457–468, doi:10.1016/1054-3139(95)80060-3.

Inall, M. E., T. Murray, F. R. Cottier, K. Scharrer, T. J. Boyd, K. J. Heywood, and S. L. Bevan, 2014: Oceanic heat delivery via Kangerdlugssuaq Fjord to the south-east Greenland ice sheet. *Journal of Geophysical Research: Oceans*, **119 (2)**, 631–645, doi:10.1002/2013JC009295.

Inall, M. E., F. Nilsen, F. R. Cottier, and R. Daae, 2015: Shelf/fjord exchange driven by coastal-trapped waves in the Arctic. *Journal of Geophysical Research: Oceans*, **120 (12)**, 8283–8303, doi:10.1002/2015JC011277.

Ingvaldsen, R., M. B. Reitan, H. Svendsen, and L. Asplin, 2001: The upper layer circulation in Kongsfjorden and Krossfjorden-A complex fjord system on the west coast of Spitsbergen (scientific paper). *Memoirs of National Institute of Polar Research. Special issue*, **54**, 393–407.

Jackson, R. H., and F. Straneo, 2016: Heat, Salt, and Freshwater Budgets for a Glacial Fjord in Greenland. *Journal of Physical Oceanography*, **46 (9)**, 2735–2768, doi:10.1175/JPO-D-15-0134.1.

Jackson, R. H., F. Straneo, and D. A. Sutherland, 2014: Externally forced fluctuations in ocean temperature at Greenland glaciers in non-summer months. *Nature Geoscience*, **7 (7)**, 503, doi:10.1038/ngeo2186.

Jackson, R. H., and Coauthors, 2017: Near-glacier surveying of a subglacial discharge plume: Implications for plume parameterizations. *Geophysical Research Letters*, **44 (13)**, 6886–6894, doi:10.1002/2017GL073602.

Jenkins, A., 1991: A one-dimensional model of ice shelf-ocean interaction. *Journal of Geophysical Research: Oceans*, **96 (C11)**, 20 671–20 677, doi:10.1029/91JC01842.

Jenkins, A., 1999: The Impact of Melting Ice on Ocean Waters. *Journal of Physical Oceanography*, **29 (9)**, 2370–2381, doi:10.1175/1520-0485(1999)029<2370:TIOMIO>2.0.CO;2.

Jenkins, A., 2011: Convection-Driven Melting near the Grounding Lines of Ice Shelves and Tidewater Glaciers. *Journal of Physical Oceanography*, **41 (12)**, 2279–2294, doi:10.1175/JPO-D-11-03.1.

Jensen, M. F., I. Fer, and E. Darelius, 2013: Low frequency variability on the continental slope of the southern Weddell Sea. *Journal of Geophysical Research: Oceans*, **118 (9)**, 4256–4272, doi:10.1002/jgrc.20309.

Johnson, H. L., A. Münchow, K. K. Falkner, and H. Melling, 2011: Ocean circulation and properties in Petermann Fjord, Greenland. *Journal of Geophysical Research: Oceans*, **116 (C1)**, C01 003, doi:10.1029/2010JC006519.

Joughin, I., R. B. Alley, and D. M. Holland, 2012: Ice-Sheet Response to Oceanic Forcing. *Science*, **338 (6111)**, 1172–1176, doi:10.1126/science.1226481.

Kimura, S., P. R. Holland, A. Jenkins, and M. Piggott, 2014: The Effect of Meltwater Plumes on the Melting of a Vertical Glacier Face. *Journal of Physical Oceanography*, **44 (12)**, 3099–3117, doi:10.1175/JPO-D-13-0219.1.

Klinck, J. M., E. E. Hofmann, R. C. Beardsley, B. Salihoglu, and S. Howard, 2004: Water-mass properties and circulation on the west Antarctic Peninsula Continental Shelf in Austral Fall and Winter 2001. *Deep Sea Research Part II: Topical Studies in Oceanography*, **51 (17–19)**, 1925–1946, doi:10.1016/j.dsr2.2004.08.001.

Klinck, J. M., J. J. O'Brien, and H. Svendsen, 1981: A Simple Model of Fjord and Coastal Circulation Interaction. *Journal of Physical Oceanography*, **11 (12)**, 1612–1626, doi:10.1175/1520-0485(1981)011<1612:ASMOFA>2.0.CO;2.

Klöser, H., G. Ferreyra, I. Schloss, G. Mercuri, F. Laturnus, and A. Curtosi, 1994: Hydrography of Potter Cove, a Small Fjord-like Inlet on King George Island (South Shetlands). *Estuarine, Coastal and Shelf Science*, **38 (5)**, 523–537, doi:10.1006/ecss.1994.1036.

Large, W. G., and S. Pond, 1981: Open Ocean Momentum Flux Measurements in Moderate to Strong Winds. *Journal of Physical Oceanography*, **11 (3)**, 324–336, doi:10.1175/1520-0485(1981)011<0324:OOMFMI>2.0.CO;2.

Launder, B. E., and D. B. Spalding, 1983: Paper 8 - The Numerical Computation Of Turbulent Flows. *Numerical Prediction of Flow, Heat Transfer, Turbulence and Combustion*, S. V. Patankar, A. Pollard, A. K. Singhal, and S. P. Vanka, Eds., Pergamon, 96–116, doi:10.1016/B978-0-08-030937-8.50016-7.

Lazzara, M. A., G. A. Weidner, L. M. Keller, J. E. Thom, and J. J. Cassano, 2012: Antarctic Automatic Weather Station Program: 30 Years of Polar Observation. *Bulletin of the American Meteorological Society*, **93 (10)**, 1519–1537, doi:10.1175/BAMS-D-11-00015.1.

Leaman, K. D., 1976: Observations on the Vertical Polarization and Energy Flux of Near-Inertial Waves. *Journal of Physical Oceanography*, **6 (6)**, 894–908, doi:10.1175/1520-0485(1976)006<0894:OOTVPA>2.0.CO;2.

Leder, N., 2002: Wind-induced internal wave dynamics near the Adriatic shelf break. *Continental Shelf Research*, **22 (3)**, 445–463, doi:10.1016/S0278-4343(01)00077-2.

Lee, J., Y. K. Jin, J. K. Hong, H. J. Yoo, and H. Shon, 2008: Simulation of a tidewater glacier evolution in Marian Cove, King George Island, Antarctica. *Geosciences Journal*, **12 (1)**, 33–39, doi:10.1007/s12303-008-0005-x.

Li, X., D. M. Holland, E. P. Gerber, and C. Yoo, 2014: Impacts of the north and tropical Atlantic Ocean on the Antarctic Peninsula and sea ice. *Nature*, **505 (7484)**, 538–542, doi:10.1038/nature12945.

Lien, R.-C., and M. C. Gregg, 2001: Observations of turbulence in a tidal beam and across a coastal ridge. *Journal of Geophysical Research: Oceans*, **106 (C3)**, 4575–4591, doi:10.1029/2000JC000351.

Loose, B., and W. J. Jenkins, 2014: The five stable noble gases are sensitive unambiguous tracers of glacial meltwater. *Geophysical Research Letters*, **41 (8)**, 2835–2841, doi:10.1002/2013GL058804.

López, O., M. A. Garcıá, D. Gomis, P. Rojas, J. Sospedra, and A. Sánchez-Arcilla, 1999: Hydrographic and hydrodynamic characteristics of the eastern basin of the Bransfield Strait (Antarctica). *Deep Sea Research Part I: Oceanographic Research Papers*, **46 (10)**, 1755–1778, doi:10.1016/S0967-0637(99)00017-5.

MacAyeal, D. R., 1985: Evolution of Tidally Triggered Meltwater Plumes Below Ice Shelves. *Oceanology of the Antarctic Continental Shelf*, American Geophysical Union (AGU), 133–143, doi:10.1029/AR043p0133.

MacKinnon, J. A., and M. C. Gregg, 2003: Shear and Baroclinic Energy Flux on the Summer New England Shelf. *Journal of Physical Oceanography*, **33 (7)**, 1462–1475, doi:10.1175/1520-0485(2003)033<1462:SABEFO>2.0.CO;2.

Magorrian, S. J., and A. J. Wells, 2016: Turbulent plumes from a glacier terminus melting in a stratified ocean. *Journal of Geophysical Research: Oceans*, **121 (7)**, 4670–4696, doi:10.1002/2015JC011160.

Manins, P. C., and B. L. Sawford, 1979: Katabatic winds: A field case study. *Quarterly Journal of the Royal Meteorological Society*, **105 (446)**, 1011–1025, doi:10.1002/qj.49710544618.

Mankoff, K. D., F. Straneo, C. Cenedese, S. B. Das, C. G. Richards, and H. Singh, 2016: Structure and dynamics of a subglacial discharge plume in a Greenlandic fjord. *Journal of Geophysical Research: Oceans*, **121 (12)**, 8670–8688, doi:10.1002/2016JC011764.

Marshall, G. J., A. Orr, N. P. M. van Lipzig, and J. C. King, 2006: The Impact of a Changing Southern Hemisphere Annular Mode on Antarctic Peninsula Summer Temperatures. *Journal of Climate*, **19 (20)**, 5388–5404, doi:10.1175/JCLI3844.1.

Martinson, D. G., and D. McKee, 2012: Transport of warm Upper Circumpolar Deep Water onto the western Antarctic Peninsula continental shelf - ProQuest. *Ocean Sci.*, **8 (4)**, 433.

Martinson, D. G., S. E. Stammerjohn, R. A. Iannuzzi, R. C. Smith, and M. Vernet, 2008: Western Antarctic Peninsula physical oceanography and spatio–temporal variability. *Deep Sea Research Part II: Topical Studies in Oceanography*, **55 (18–19)**, 1964–1987, doi:10.1016/j.dsr2.2008.04.038.

May, S., C. E. McClennen, and E. W. Domack, 1991: Diatom assemblages within surface waters of Andvord Bay, Antarctica. *Antarctic Journal of the United States*, **26**, 112–114.

McGrath, D., K. Steffen, I. Overeem, S. H. Mernild, B. Hasholt, and M. V. D. Broeke, 2010/ed: Sediment plumes as a proxy for local ice-sheet runoff in Kangerlussuaq Fjord, West Greenland. *Journal of Glaciology*, **56 (199)**, 813–821, doi:10.3189/002214310794457227.

McPhee, M. G., 1992: Turbulent heat flux in the upper ocean under sea ice. *Journal of Geophysical Research: Oceans*, **97 (C4)**, 5365–5379, doi:10.1029/92JC00239.

Meredith, M. P., and J. C. King, 2005: Rapid climate change in the ocean west of the Antarctic Peninsula during the second half of the 20th century. *Geophysical Research Letters*, **32 (19)**, L19 604, doi:10.1029/2005GL024042.

Meredith, M. P., H. J. Venables, A. Clarke, H. W. Ducklow, M. Erickson, M. J. Leng, J. T. M. Lenaerts, and M. R. van den Broeke, 2012: The Freshwater System West of the Antarctic Peninsula: Spatial and Temporal Changes. *Journal of Climate*, **26 (5)**, 1669–1684, doi:10.1175/JCLI-D-12-00246.1.

Moffat, C., 2014: Wind-driven modulation of warm water supply to a proglacial fjord, Jorge Montt Glacier, Patagonia. *Geophysical Research Letters*, **41 (11)**, 3943–3950, doi:10.1002/2014GL060071.

Moffat, C., R. C. Beardsley, B. Owens, and N. van Lipzig, 2008: A first description of the Antarctic Peninsula Coastal Current. *Deep Sea Research Part II: Topical Studies in Oceanography*, **55 (3–4)**, 277–293, doi:10.1016/j.dsr2.2007.10.003.

Moffat, C., and M. Meredith, 2018: Shelf–ocean exchange and hydrography west of the Antarctic Peninsula: A review. *Phil. Trans. R. Soc. A*, **376 (2122)**, 20170 164, doi:10.1098/rsta.2017.0164.

Montes-Hugo, M., S. C. Doney, H. W. Ducklow, W. Fraser, D. Martinson, S. E. Stammerjohn, and O. Schofield, 2009: Recent Changes in Phytoplankton Communities Associated with Rapid Regional Climate Change Along the Western Antarctic Peninsula. *Science*, **323 (5920)**, 1470–1473, doi:10.1126/science.1164533.

Moreau, S., B. Mostajir, S. Bélanger, I. R. Schloss, M. Vancoppenolle, S. Demers, and G. A. Ferreyra, 2015: Climate change enhances primary production in the western Antarctic Peninsula. *Global Change Biology*, **21 (6)**, 2191–2205, doi:10.1111/gcb.12878.

Mortensen, J., K. Lennert, J. Bendtsen, and S. Rysgaard, 2011: Heat sources for glacial melt in a sub-Arctic fjord (Godthåbsfjord) in contact with the Greenland Ice Sheet. *Journal of Geophysical Research: Oceans*, **116 (C1)**, C01 013, doi:10.1029/2010JC006528.

Mortimer, C. H., 2006: Inertial oscillations and related internal beat pulsations and surges in Lakes Michigan and Ontario. *Limnology and Oceanography*, **51 (5)**, 1941–1955, doi:10.4319/lo.2006.51.5.1941.

Morton, B. R., G. I. Taylor, and J. S. Turner, 1956: Turbulent gravitational convection from maintained and instantaneous sources. *Proc. R. Soc. Lond. A*, **234 (1196)**, 1–23, doi:10.1098/rspa.1956.0011.

Motyka, R. J., W. P. Dryer, J. Amundson, M. Truffer, and M. Fahnestock, 2013: Rapid submarine melting driven by subglacial discharge, LeConte Glacier, Alaska. *Geophysical Research Letters*, **40 (19)**, 5153–5158, doi:10.1002/grl.51011.

Motyka, R. J., L. Hunter, K. A. Echelmeyer, and C. Connor, 2003: Submarine melting at the terminus of a temperate tidewater glacier, LeConte Glacier, Alaska, U.S.A. *Annals of Glaciology*, **36 (1)**, 57–65, doi:10.3189/172756403781816374.

Mugford, R. I., and J. A. Dowdeswell, 2011: Modeling glacial meltwater plume dynamics and sedimentation in high-latitude fjords. *Journal of Geophysical Research: Earth Surface*, **116 (F1)**, doi:10.1029/2010JF001735.

Neshyba, S., and E. G. Josberger, 1980: On the Estimation of Antarctic Iceberg Melt Rate. *Journal of Physical Oceanography*, **10 (10)**, 1681–1685, doi:10.1175/1520-0485(1980)010<1681:OTEOAI>2.0.CO;2.

Nielsen, S., K. Steffen, and C. Charalampidis, 2014: Katabatic winds and piteraq storms: Observations from the Greenland ice sheet. *Geological Survey of Denmark and Greenland Bulletin*, **31**, 83–86.

Nilsen, F., F. Cottier, R. Skogseth, and S. Mattsson, 2008: Fjord–shelf exchanges controlled by ice and brine production: The interannual variation of Atlantic Water in Isfjorden, Svalbard. *Continental Shelf Research*, **28 (14)**, 1838–1853, doi:10.1016/j.csr.2008.04.015.

Nowacek, D. P., and Coauthors, 2011: Super-Aggregations of Krill and Humpback Whales in Wilhelmina Bay, Antarctic Peninsula. *PLoS ONE*, **6 (4)**, doi:10.1371/journal.pone.0019173.

Ó Cofaigh, C., and J. A. Dowdeswell, 2001: Laminated sediments in glacimarine environments: Diagnostic criteria for their interpretation. *Quaternary Science Reviews*, **20 (13)**, 1411–1436, doi:10.1016/S0277-3791(00)00177-3.

Oakey, N. S., 1982: Determination of the Rate of Dissipation of Turbulent Energy from Simultaneous Temperature and Velocity Shear Microstructure Measurements. *Journal of Physical Oceanography*, **12 (3)**, 256–271, doi:10.1175/1520-0485(1982)012<0256:DOTROD>2.0.CO;2.

Oliva, M., F. Navarro, F. Hrbáček, A. Hernández, D. Nývlt, P. Pereira, J. Ruiz-Fernández, and R. Trigo, 2017: Recent regional climate cooling on the Antarctic Peninsula and associated impacts on the cryosphere. *Science of The Total Environment*, **580**, 210–223, doi:10.1016/j.scitotenv.2016.12.030.

Oltmanns, M., F. Straneo, G. W. K. Moore, and S. H. Mernild, 2013: Strong Downslope Wind Events in Ammassalik, Southeast Greenland. *Journal of Climate*, **27 (3)**, 977–993, doi:10.1175/JCLI-D-13-00067.1.

Orsi, A. H., T. Whitworth, and W. D. Nowlin, 1995: On the meridional extent and fronts of the Antarctic Circumpolar Current. *Deep Sea Research Part I: Oceanographic Research Papers*, **42 (5)**, 641–673, doi:10.1016/0967-0637(95)00021-W.

Padman, L., D. P. Costa, S. T. Bolmer, M. E. Goebel, L. A. Huckstadt, A. Jenkins, B. I. McDonald, and D. R. Shoosmith, 2010: Seals map bathymetry of the Antarctic continental shelf. *Geophysical Research Letters*, **37 (21)**, doi:10.1029/2010GL044921.

Palóczy, A., S. Gille, and J. Mcclean, 2018: Oceanic heat delivery to the Antarctic continental shelf: Large-scale, low-frequency variability. *Journal of Geophysical Research: Oceans*, doi:10.1029/2018JC014345.

Parish, T. R., 1988: Surface winds over the Antarctic continent: A review. *Reviews of Geophysics*, **26 (1)**, 169–180, doi:10.1029/RG026i001p00169.

Pedlosky, J., 2013: *Waves in the Ocean and Atmosphere: Introduction to Wave Dynamics*. Springer Science & Business Media.

Peltier, W. R., and C. P. Caulfield, 2003: Mixing Efficiency in Stratified Shear Flows. *Annual Review of Fluid Mechanics*, **35 (1)**, 135–167, doi:10.1146/annurev.fluid.35.101101.161144.

Perkin, R. G., and L. Lewis, 1978: Mixing in an Arctic Fjord. *Journal of Physical Oceanography*, **8 (5)**, 873–880, doi:10.1175/1520-0485(1978)008<0873:MIAAF>2.0.CO;2.

Powell, R. D., M. Dawber, J. N. McInnes, and A. R. Pyne, 1996: Observations of the grounding-line area at a floating glacier terminus. *Annals of Glaciology*, **22**, 217–223, doi:10.3189/1996AoG22-1-217-223.

Pritchard, H. D., and D. G. Vaughan, 2007: Widespread acceleration of tidewater glaciers on the Antarctic Peninsula. *Journal of Geophysical Research: Earth Surface*, **112 (F3)**, F03S29, doi:10.1029/2006JF000597.

Raiswell, R., L. G. Benning, M. Tranter, and S. Tulaczyk, 2008: Bioavailable iron in the Southern Ocean: The significance of the iceberg conveyor belt. *Geochemical Transactions*, **9**, 7, doi:10.1186/1467-4866-9-7.

Rau, F., and Coauthors, 2004: Variations of glacier frontal positions on the northern Antarctic Peninsula. *Annals of Glaciology*, **39 (1)**, 525–530, doi:10.3189/172756404781814212.

Renfrew, I. A., 2004: The dynamics of idealized katabatic flow over a moderate slope and ice shelf. *Quarterly Journal of the Royal Meteorological Society*, **130 (598)**, 1023–1045, doi:10.1256/qj.03.24.

Rignot, E., I. Fenty, D. Menemenlis, and Y. Xu, 2012: Spreading of warm ocean waters around Greenland as a possible cause for glacier acceleration. *Annals of Glaciology*, **53 (60)**, 257–266, doi:10.3189/2012AoG60A136.

Rignot, E., I. Fenty, Y. Xu, C. Cai, and C. Kemp, 2015: Undercutting of marine-terminating glaciers in West Greenland. *Geophysical Research Letters*, **42 (14)**, 5909–5917, doi:10.1002/2015GL064236.

Rignot, E., M. Koppes, and I. Velicogna, 2010: Rapid submarine melting of the calving faces of West Greenland glaciers. *Nature Geoscience*, **3 (3)**, ngeo765, doi:10.1038/ngeo765.

Rodrigo, C., S. Giglio, and A. Varas, 2016: Glacier sediment plumes in small bays on the Danco Coast, Antarctic Peninsula. *Antarctic Science*, **28 (5)**, 395–404, doi:10.1017/S0954102016000237.

Ross, L., I. Pérez-Santos, A. Valle-Levinson, and W. Schneider, 2014: Semidiurnal internal tides in a Patagonian fjord. *Progress in Oceanography*, **129, Part A**, 19–34, doi:10.1016/j.pocean.2014.03.006.

Ryan, W. B. F., and Coauthors, 2009: Global Multi-Resolution Topography synthesis. *Geochemistry, Geophysics, Geosystems*, **10 (3)**, Q03 014, doi:10.1029/2008GC002332.

Saloranta, T. M., and H. Svendsen, 2001: Across the Arctic front west of Spitsbergen: High-resolution CTD sections from 1998–2000. *Polar Research*, **20 (2)**, 177–184, doi:10.3402/polar.v20i2.6515.

Sangrà, P., and Coauthors, 2011: The Bransfield current system. *Deep Sea Research Part I: Oceanographic Research Papers*, **58 (4)**, 390–402, doi:10.1016/j.dsr.2011.01.011.

Santini, M. F., R. B. Souza, I. Wainer, and M. M. Muelbert, 2018: Temporal analysis of water masses and sea ice formation rate west of the Antarctic Peninsula in 2008 estimated from southern elephant seals' SRDL–CTD data. *Deep Sea Research Part II: Topical Studies in Oceanography*, doi:10.1016/j.dsr2.2018.02.013.

Schloss, I. R., D. Abele, S. Moreau, S. Demers, A. V. Bers, O. González, and G. A. Ferreyra, 2012: Response of phytoplankton dynamics to 19-year (1991–2009) climate trends in Potter Cove (Antarctica). *Journal of Marine Systems*, **92 (1)**, 53–66, doi:10.1016/j.jmarsys.2011.10.006.

Sciascia, R., F. Straneo, C. Cenedese, and P. Heimbach, 2013: Seasonal variability of submarine melt rate and circulation in an East Greenland fjord. *Journal of Geophysical Research: Oceans*, **118 (5)**, 2492–2506, doi:10.1002/jgrc.20142.

Shchepetkin, A. F., and J. C. McWilliams, 2005: The regional oceanic modeling system (ROMS): A split-explicit, free-surface, topography-following-coordinate oceanic model. *Ocean Modelling*, **9 (4)**, 347–404, doi:10.1016/j.ocemod.2004.08.002.

Sherrell, R. M., A. L. Annett, J. N. Fitzsimmons, V. J. Roccanova, and M. P. Meredith, 2018: A 'shallow bathtub ring'of local sedimentary iron input maintains the Palmer Deep biological hotspot on the West Antarctic Peninsula shelf. *Phil. Trans. R. Soc. A*, **376**, 20170 171.

Simões, J. C., U. F. Bremer, F. E. Aquino, and F. A. Ferron, 1999/ed: Morphology and variations of glacial drainage basins in the King George Island ice field, Antarctica. *Annals of Glaciology*, **29**, 220–224, doi:10.3189/172756499781821085.

Skarðhamar, J., and H. Svendsen, 2010: Short-term hydrographic variability in a stratified Arctic fjord. *Geological Society, London, Special Publications*, **344 (1)**, 51–60, doi:10.1144/SP344.5.

Slater, D. A., P. W. Nienow, T. R. Cowton, D. N. Goldberg, and A. J. Sole, 2015: Effect of near-terminus subglacial hydrology on tidewater glacier submarine melt rates. *Geophysical Research Letters*, **42 (8)**, 2861–2868, doi:10.1002/2014GL062494.

Slater, D. A., P. W. Nienow, D. N. Goldberg, T. R. Cowton, and A. J. Sole, 2017: A model for tidewater glacier undercutting by submarine melting. *Geophysical Research Letters*, **44 (5)**, 2360–2368, doi:10.1002/2016GL072374.

Smagorinsky, J., 1963: General circulation experiments with the primitive equations. *Monthly Weather Review*, **91 (3)**, 99–164, doi:10.1175/1520-0493(1963)091<0099:GCEWTP>2.3.CO;2.

Smith, A. M., D. G. Vaughan, C. S. M. Doake, and A. C. Johnson, 1998: Surface lowering of the ice ramp at Rother a Point, Antarctic Peninsula, in response to regional climate change. *Annals of Glaciology*, **27**, 113–118, doi:10.3189/1998AoG27-1-113-118.

Smith, C. R., 2017a: Processed Underway Hydrographic and Weather and Ship-state Data (JGOFS) from the Antarctic Peninsula acquired during R/V Laurence M. Gould expedition LMG1510 (2015). *Interdisciplinary Earth Data Alliance (IEDA)*, doi:10.1594/IEDA/323575.

Smith, C. R., 2017b: Raw Conductivity, Oxygen, Pressure and Temperature Data from the Antarctic Peninsula acquired during R/V Laurence M. Gould expedition LMG1510 (2015). doi:10.1594/IEDA/323576.

Smith, D. A., E. E. Hofmann, J. M. Klinck, and C. M. Lascara, 1999: Hydrography and circulation of the West Antarctic Peninsula Continental Shelf. *Deep Sea Research Part I: Oceanographic Research Papers*, **46 (6)**, 925–949, doi:10.1016/S0967-0637(98)00103-4.

Smith, R. C., Dierssen Heidi M., and Vernet Maria, 2013: Phytoplankton Biomass and Productivity in the Western Antarctic Peninsula Region. *Foundations for Ecological Research West of the Antarctic Peninsula*, doi:10.1029/AR070p0333.

Spall, M. A., R. H. Jackson, and F. Straneo, 2017: Katabatic Wind-Driven Exchange in Fjords. *Journal of Geophysical Research: Oceans*, **122 (10)**, 8246–8262, doi:10.1002/2017JC013026.

Spence, P., R. M. Holmes, A. M. Hogg, S. M. Griffies, K. D. Stewart, and M. H. England, 2017: Localized rapid warming of West Antarctic subsurface waters by remote winds. *Nature Climate Change*, **7 (8)**, 595–603, doi:10.1038/nclimate3335.

Stammerjohn, S. E., D. G. Martinson, R. C. Smith, and R. A. Iannuzzi, 2008: Sea ice in the western Antarctic Peninsula region: Spatio-temporal variability from ecological and climate change perspectives. *Deep Sea Research Part II: Topical Studies in Oceanography*, **55 (18–19)**, 2041–2058, doi:10.1016/j.dsr2.2008.04.026.

Stastna, V., 2010: Spatio-temporal changes in surface air temperature in the region of the northern Antarctic Peninsula and south Shetland islands during 1950–2003. *Polar Science*, **4 (1)**, 18–33, doi:10.1016/j.polar.2010.02.001.

Stigebrandt, A., 1976: Vertical Diffusion Driven by Internal Waves in a Sill Fjord. *Journal of Physical Oceanography*, **6 (4)**, 486–495, doi:10.1175/1520-0485(1976)006<0486:VDDBIW>2.0.CO;2.

Stigebrandt, A., and J. Aure, 1989: Vertical Mixing in Basin Waters of Fjords. *Journal of Physical Oceanography*, **19 (7)**, 917–926, doi:10.1175/1520-0485(1989)019<0917:VMIBWO>2.0.CO;2.

Stigebrandt, A., and J. Aure, 1990: De ytre drivkreftenes betydning for vannutskiftningen i fjordene fra Skagerrak til Finnmark. Working paper, Havforskningsinstituttet.

Straneo, F., and C. Cenedese, 2015: The Dynamics of Greenland's Glacial Fjords and Their Role in Climate. *Annual Review of Marine Science*, **7 (1)**, 89–112, doi:10.1146/annurev-marine-010213-135133.

Straneo, F., R. G. Curry, D. A. Sutherland, G. S. Hamilton, C. Cenedese, K. Våge, and L. A. Stearns, 2011: Impact of fjord dynamics and glacial runoff on the circulation near Helheim Glacier. *Nature Geoscience*, **4 (5)**, 322–327, doi:10.1038/ngeo1109.

Straneo, F., and P. Heimbach, 2013: North Atlantic warming and the retreat of Greenland's outlet glaciers. *Nature*, **504 (7478)**, 36–43, doi:10.1038/nature12854.

Straneo, F., and Coauthors, 2012: Characteristics of ocean waters reaching Greenland's glaciers. *Annals of Glaciology*, **53 (60)**, 202–210, doi:10.3189/2012AoG60A059.

Sundfjord, A., and Coauthors, 2017: Effects of glacier runoff and wind on surface layer dynamics and Atlantic Water exchange in Kongsfjorden, Svalbard; a model study. *Estuarine, Coastal and Shelf Science*, **187**, 260–272, doi:10.1016/j.ecss.2017.01.015.

Sutherland, D. A., G. E. Roth, G. S. Hamilton, S. H. Mernild, L. A. Stearns, and F. Straneo, 2014a: Quantifying flow regimes in a Greenland glacial fjord using iceberg drifters. *Geophysical Research Letters*, **41 (23)**, 2014GL062 256, doi:10.1002/2014GL062256.

Sutherland, D. A., and F. Straneo, 2012: Estimating ocean heat transports and submarine melt rates in Sermilik Fjord, Greenland, using lowered acoustic Doppler current profiler (LADCP) velocity profiles. *Annals of Glaciology*, **53 (60)**, 50–58, doi:10.3189/2012AoG60A050.

Sutherland, D. A., F. Straneo, and R. S. Pickart, 2014b: Characteristics and dynamics of two major Greenland glacial fjords. *Journal of Geophysical Research: Oceans*, **119 (6)**, 3767–3791, doi:10.1002/2013JC009786.

Svendsen, H., 1995: Physical oceanography of coupled fjord-coast systems in northern Norway with special focus on frontal dynamics and tides. *Ecology of Fjords and Coastal Waters*, Elsevier, New York, 149–164.

Svendsen, H., and R. O. R. Y. Thompson, 1978: Wind-Driven Circulation in a Fjord. *Journal of Physical Oceanography*, **8 (4)**, 703–712, doi:10.1175/1520-0485(1978)008<0703:WDCIAF>2.0.CO;2.

Svendsen, H., and Coauthors, 2002: The physical environment of Kongsfjorden–Krossfjorden, an Arctic fjord system in Svalbard. *Polar Research*, **21 (1)**, 133–166, doi:10.1111/j.1751-8369.2002.tb00072.x.

Syvitski, J. P. M., 1989: On the deposition of sediment within glacier-influenced fjords: Oceanographic controls. *Marine Geology*, **85 (2)**, 301–329, doi:10.1016/0025-3227(89)90158-8.

Syvitski, J. P. M., G. E. Farrow, R. J. A. Atkinson, P. G. Moore, and J. T. Andrews, 1989: Baffin Island Fjord Macrobenthos: Bottom Communities and Environmental Significance. *Arctic*, **42 (3)**, 232–247.

Turner, J., and Coauthors, 2005: Antarctic climate change during the last 50 years. *International Journal of Climatology*, **25 (3)**, 279–294, doi:10.1002/joc.1130.

Turner, J., and Coauthors, 2016: Absence of 21st century warming on Antarctic Peninsula consistent with natural variability. *Nature*, **535 (7612)**, 411–415, doi:10.1038/nature18645.

Valipour, R., D. Bouffard, L. Boegman, and Y. R. Rao, 2015: Near-inertial waves in Lake Erie. *Limnology and Oceanography*, **60 (5)**, 1522–1535, doi:10.1002/lno.10114.

Valle-Levinson, A., M. A. Caceres, and O. Pizarro, 2014: Variations of tidally driven three-layer residual circulation in fjords. *Ocean Dynamics*, **64 (3)**, 459–469, doi:10.1007/s10236-014-0694-9.

van den Broeke, M., P. Smeets, J. Ettema, C. van der Veen, R. van de Wal, and J. Oerlemans, 2008: Partitioning of melt energy and meltwater fluxes in the ablation zone of the west Greenland ice sheet. *The Cryosphere*, **2 (2)**, 179–189, doi:10.5194/tc-2-179-2008.

van der Lee, E. M., and L. Umlauf, 2011: Internal wave mixing in the Baltic Sea: Near-inertial waves in the absence of tides. *Journal of Geophysical Research: Oceans*, **116 (C10)**, C10016, doi:10.1029/2011JC007072.

van Wessem, J. M., M. P. Meredith, C. H. Reijmer, M. R. van den Broeke, and A. J. Cook, 2016: Characteristics of the modelled meteoric freshwater budget of the western Antarctic Peninsula. *Deep Sea Research Part II: Topical Studies in Oceanography*, doi:10.1016/j.dsr2.2016.11.001.

van Wessem, J. M., C. H. Reijmer, W. J. van de Berg, M. R. van den Broeke, A. J. Cook, L. H. van Ulft, and E. van Meijgaard, 2015: Temperature and Wind Climate of the Antarctic Peninsula as Simulated by a High-Resolution Regional Atmospheric Climate Model. *Journal of Climate*, **28 (18)**, 7306–7326, doi:10.1175/JCLI-D-15-0060.1.

Vaquer-Sunyer, R., and C. M. Duarte, 2008: Thresholds of hypoxia for marine biodiversity. *Proceedings of the National Academy of Sciences*, **105 (40)**, 15452–15457, doi:10.1073/pnas.0803833105.

Vaughan, D. G., 2006: Recent Trends in Melting Conditions on the Antarctic Peninsula and Their Implications for Ice-sheet Mass Balance and Sea Level. *Arctic, Antarctic, and Alpine Research*, **38 (1)**, 147–152, doi:10.1657/1523-0430(2006)038[0147:RTIMCO]2.0.CO;2.

Vaughan, D. G., and Coauthors, 2003: Recent Rapid Regional Climate Warming on the Antarctic Peninsula. *Climatic Change*, **60 (3)**, 243–274, doi:doi:10.1023/A:1026021217991.

Venables, H. J., and M. P. Meredith, 2014: Feedbacks between ice cover, ocean stratification, and heat content in Ryder Bay, western Antarctic Peninsula. *Journal of Geophysical Research: Oceans*, **119 (8)**, 5323–5336, doi:10.1002/2013JC009669.

Vernet, M., D. Martinson, R. Iannuzzi, S. Stammerjohn, W. Kozlowski, K. Sines, R. Smith, and I. Garibotti, 2008: Primary production within the sea-ice zone west of the Antarctic Peninsula: I—Sea ice, summer mixed layer, and irradiance. *Deep Sea Research Part II: Topical Studies in Oceanography*, **55 (18)**, 2068–2085, doi:10.1016/j.dsr2.2008.05.021.

Vieli, A., and F. M. Nick, 2011: Understanding and Modelling Rapid Dynamic Changes of Tidewater Outlet Glaciers: Issues and Implications. *Surveys in Geophysics*, **32 (4)**, 437–458, doi:10.1007/s10712-011-9132-4.

Wadley, M. R., T. D. Jickells, and K. J. Heywood, 2014: The role of iron sources and transport for Southern Ocean productivity. *Deep Sea Research Part I: Oceanographic Research Papers*, **87**, 82–94, doi:10.1016/j.dsr.2014.02.003.

Wang, D.-P., and C. N. K. Mooers, 1976: Coastal-Trapped Waves in a Continuously Stratified Ocean. *Journal of Physical Oceanography*, **6 (6)**, 853–863, doi:10.1175/1520-0485(1976)006<0853:CTWIAC>2.0.CO;2.

Waterhouse, A. F., and Coauthors, 2014: Global Patterns of Diapycnal Mixing from Measurements of the Turbulent Dissipation Rate. *Journal of Physical Oceanography*, **44 (7)**, 1854–1872, doi:10.1175/JPO-D-13-0104.1.

Whitworth, T., W. D. Nowlin, A. H. Orsi, R. A. Locarnini, and S. G. Smith, 1994: Weddell Sea shelf water in the Bransfield Strait and Weddell-Scotia Confluence. *Deep Sea Research Part I: Oceanographic Research Papers*, **41 (4)**, 629–641, doi:10.1016/0967-0637(94)90046-9.

Wilson, C., G. P. Klinkhammer, and C. S. Chin, 1999: Hydrography within the Central and East Basins of the Bransfield Strait, Antarctica. *Journal of Physical Oceanography*, **29 (3)**, 465–479, doi:10.1175/1520-0485(1999)029<0465:HWTCAE>2.0.CO;2.

Wouters, B., A. Martin-Español, V. Helm, T. Flament, J. M. van Wessem, S. R. M. Ligtenberg, M. R. van den Broeke, and J. L. Bamber, 2015: Dynamic thinning of glaciers on the Southern Antarctic Peninsula. *Science*, **348 (6237)**, 899–903, doi:10.1126/science.aaa5727.

Wunsch, C., and R. Ferrari, 2004: Vertical Mixing, Energy, and the General Circulation of the Oceans. *Annual Review of Fluid Mechanics*, **36 (1)**, 281–314, doi:10.1146/annurev.fluid.36.050802.122121.

Xu, Y., E. Rignot, I. Fenty, D. Menemenlis, and M. M. Flexas, 2013: Subaqueous melting of Store Glacier, west Greenland from three-dimensional, high-resolution numerical modeling and ocean observations. *Geophysical Research Letters*, **40 (17)**, 4648–4653, doi:10.1002/grl.50825.

Yoon, H. I., B. K. Park, E. W. Domack, and Y. Kim, 1998: Distribution and dispersal pattern of suspended particulate matter in Maxwell Bay and its tributary, Marian Cove, in the South Shetland Islands, West Antarctica. *Marine Geology*, **152 (4)**, 261–275, doi:10.1016/S0025-3227(98)00098-X.

Zhou, M., P. P. Niiler, and J.-H. Hu, 2002: Surface currents in the Bransfield and Gerlache Straits, Antarctica. *Deep Sea Research Part I: Oceanographic Research Papers*, **49 (2)**, 267–280, doi:10.1016/S0967-0637(01)00062-0.

Zwally, H. J., Comiso Josefino C., Parkinson Claire L., Cavalieri Donald J., and Gloersen Per, 2002: Variability of Antarctic sea ice 1979–1998. *Journal of Geophysical Research: Oceans*, **107 (C5)**, 9–1, doi:10.1029/2000JC000733.